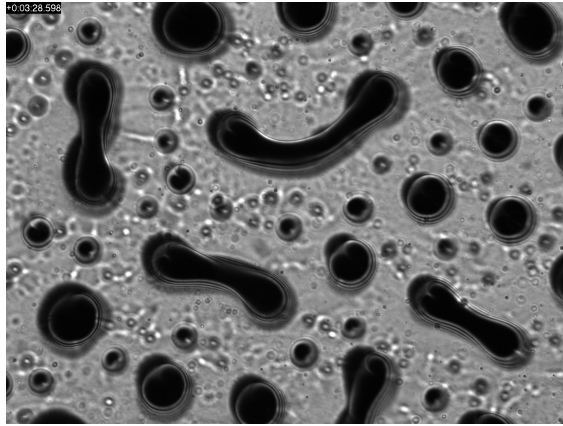


# Magnetic field induced equilibrium textures and non-equilibrium motion of particles



Von der Universität Bayreuth  
zur Erlangung des Grades eines  
Doktor der Naturwissenschaften (Dr. rer. nat.)  
genehmigte Abhandlung

von

**Jonas Bugase**

aus Chiana in Ghana

1. Gutachter: Prof. Dr. Thomas M. Fischer
2. Gutachter: Prof. Dr. Werner Köhler

Tag der Einreichung: 13.06.2018

Tag des Kolloquiums: 16.08.2018



# Abstract

This cumulative thesis is dedicated to the study of magnetic fields driven phenomena in two forms. Magnetic fields are used to (i) induce phase separation and modulated phases in a critical mixture and (ii) drive the motion of particles on two-dimensional periodic magnetic lattices. The study focuses on the fundamental physical mechanism (s) that drives these phenomena and contributes to knowledge and understanding of these systems.

In the first part of this work, the phase behavior of a critical ferrofluid mixture in the presence of an external magnetic field is presented. With an applied perpendicular field to the plane of the mixture, an induced demixing is achieved with mesoscopic-sized droplets of the magnetic-rich phase immersed in the non-magnetic majority phase. A variety of modulated phases is exhibited including droplets deformation and labyrinthine patterns. A wrinkling feature of the phase separated droplets in two length scales is also reported. This feature is only observed when the mixture is placed on a substrate such that an air-liquid interface is present. The phase behavior and equilibrium patterns of the mixture is due to competing dipolar-dipolar interactions, interfacial energy and entropy of mixing. The experimental observations have been described with appropriate theory and the two compare favorably.

The second part deals with the driven motion of magnetic particles on magnetic crystal lattices of different symmetries. Using concepts of topology, a robust and reliable transport of colloidal particles is achieved. Colloidal particles placed on top of the magnetic periodic crystals experience the field of the alternating up and down magnetized domains of the pattern. Applying an external time-dependent field in a specific closed loop modulates the potential of the colloids such that it causes them to move along the lattice of the pattern. This motion is proved to be topologically protected and robust against small perturbation. Performing experiments on all possible two-dimensional magnetic point group symmetries, a deep connection between topology and symmetry of the transport mechanism is established. The predicted theory for the transport modes quantitatively agrees with the results of experiment.

The topological protected transport of the colloidal system is further scaled up to a macroscopic scale with a simple, easy to reproduce set up. This offers a real-time observation of the transport of particles and reorientation of the external magnetic field. Using existing theories of the colloidal system, millimeter-sized magnetic particles are transported on magnetic lattices of the same dimension. The results emphasize robustness of the theory for the topologically protected transport in the colloidal system since the two systems are three orders of magnitude different. This

implies a possible down scaling to the molecular level and potential applications in other condensed matter systems.

# Kurzdarstellung

Diese kumulative Dissertation widmet sich der Untersuchung von zwei verschiedenen, magnetfeldgesteuerten Phänomenen. Magnetfelder werden verwendet, um (i) in einer kritischen Mischung Phasenseparationen und modulierte Phasen zu erzeugen und (ii) Bewegung von Teilchen auf einem zweidimensionalen magnetischen Kristallgitter zu induzieren. Die Untersuchung fokussiert sich auf die fundamentalen physikalischen Mechanismen, denen diese Phänomene zugrunde liegen und leistet so einen Beitrag zu Kenntnis und Verständnis beider Systeme.

Im ersten Teil dieser Arbeit wird das Phasenverhalten einer kritischen Ferrofluidmischung in einem externen magnetischen Feld dargestellt. Durch ein senkrecht zur Flüssigkeitsebene angelegtes Magnetfeld wird eine Entmischung in mesoskopische Tröpfchen einer ferrofluidreichen Phase, die in der überwiegenden, unmagnetischen Phase eingebettet sind, induziert. Es wird eine Vielzahl an modulierten Phasen ausgebildet, darunter Verformungen der Tröpfchen und labyrinthartige Muster. Für die phasenseparierten Tröpfchen wird zudem eine Faltenbildung auf zwei Längenskalen beobachtet. Diese Eigenschaft tritt nur auf, wenn die Mischung so auf die Unterlage aufgebracht wird, dass eine Luft-Flüssigkeits-Grenzfläche existiert. Das Phasenverhalten und die Gleichgewichtsmuster der Mischung entstehen durch konkurrierende Dipol-Dipol Wechselwirkungen, sowie Oberflächenenergie- und Entropiebeiträge der Mischung. Die experimentellen Beobachtungen wurden mit entsprechender Theorie beschrieben und beide stimmen gut überein.

Der zweite Teil beschäftigt sich mit der induzierten Bewegung magnetischer Partikel auf magnetischen Kristallgittern verschiedener Symmetrien. Durch das Ausnutzen topologischer Eigenschaften kann ein robuster und verlässlicher Transport der kolloidalen Teilchen erreicht werden. Kolloide, die sich auf einem solchen magnetischen Muster befinden, spüren das Feld der abwechselnd nach oben und unten magnetisierten Domänen des periodischen Musters. Ein zeitabhängiges, externes Feld, welches einer spezifischen, geschlossenen Kurve folgt, verändert das Potential für die Kolloide so, dass diese sich entlang des Gitters des magnetischen Musters bewegen. Es wurde gezeigt, dass die Bewegung topologisch geschützt und robust gegen kleine Störungen ist. Durch Experimente auf magnetischen Mustern mit allen in zwei Dimensionen möglichen Punktgruppensymmetrien wird eine tiefe Verbindung zwischen der Topologie des Systems und der Symmetrie des Transportmechanismus hergestellt. Die vorhergesagte Theorie für die Transportmoden stimmt quantitativ mit den experimentellen Ergebnissen überein.

Der topologisch geschützte Transport des kolloidalen Systems wird weiterhin mit einem einfachen und leicht reproduzierbaren Aufbau auf makroskopische Ebene hochskaliert. Dies ermöglicht Beobachtungen des Teilchentransportes und der Neu-

ausrichtung des Magnetfeldes in Echtzeit. Unter Verwendung der bestehenden Theorien werden magnetische Teilchen in der Größe von einem Millimeter über ein magnetisches Gitter der selben Größenordnung transportiert. Die Ergebnisse unterstützen die Robustheit der Theorie für topologisch geschützten Transport im kolloidalen System, da die beiden Systeme sich um drei Größenordnungen unterscheiden. Dies sollte die Verkleinerung auf molekulare Ebene und potentielle Anwendungen in anderen Systemen kondensierter Materie ermöglichen.

# Acknowledgments

My sincere gratitude is to Almighty God for His guidance and protection during the period of this work and for a dream come true. Many thanks goes to my supervisor Prof. Dr. Thomas M. Fischer for his unquantifiable motivation, interactive discussions, encouragement, and support especially during challenging time both academic and stipend-wise. I forever remain grateful to him and his entire family.

My special thanks goes to my beloved wife Ida Tamsowe, kids (Maximilian, Marina and Muriel), and my entire family for their enormous support. To my laboratory and office colleagues; Florian, Johannes, Thomas, Anna, and Adrian, it has been a wonderful encounter and your contribution is deeply acknowledged.

I also appreciate the inspiring, supportive and enjoyable time with my family in Bayreuth and I say to you Uncle Fred, Dr. Kiwori (Massa), Man Rogers, Uncle Aziz, Barakka, Big Man (Imani), Benedict, Nikita, Dr. Sabbi , a big Thank you.



# Contents

|  |            |
|--|------------|
| <b>Abstract</b>  | <b>i</b>   |
| <b>Kurzdarstellung</b>   | <b>iii</b> |
| <b>Acknowledgments</b>   | <b>v</b>   |
| <b>1 Introduction</b>  | <b>1</b>   |
| <b>2 Magnetic field induced phases phenomena</b>   | <b>7</b>   |
| 1 Critical demixing of a ferrofluid mixture . . . . .  | 7          |
| 1.1 Phase Separation and Thermodynamics . . . . .  | 9          |
| 2 Wrinkling in ferrofluid mixture . . . . .  | 11         |
| 3 Conclusion and outlook . . . . .   | 12         |
| <b>3 Topologically protected transport</b>   | <b>15</b>  |
| 1 Microscopic transport of colloidal particles . . . . .   | 18         |
| 2 Macroscopic transport of particles . . . . .   | 23         |
| 3 Conclusion and outlook . . . . .   | 24         |
| <b>A Materials and Methods</b>   | <b>25</b>  |
| A.1 Field induced Self Assembly patterns . . . . .   | 25         |
| A.2 Topological protected microscopic transport . . . . .  | 27         |
| A.3 Macroscopic Floquet crystalline pump . . . . .   | 29         |
| <b>Bibliography</b>  | <b>33</b>  |
| <b>Publications</b>  | <b>37</b>  |
| P1 Magnetic field induced modulated phases in ferrofluid lutidine silicone oil mixture . . . . . | 39         |
| P2 Wrinkled labyrinths in critical demixing ferrofluid . . . . .                                 | 49         |
| P3 Lattice symmetries and topologically protected transport of colloidal particles . . . . .     | 57         |
| P4 Macroscopic Floquet topological crystalline steel and superconductor pump . . . . .           | 91         |



# Chapter 1

## Introduction

The field of soft matter involves the study of a large collection of materials mainly composed of polymers, colloids, liquid crystal, surfactants and other mesoscopic constituents which are extensively used in everyday life and modern technology [1]. These classes of materials according to Pierre-Gilles de Gennes (Nobel Prize in Physics 1991) tend to respond largely to a small mechanical, thermal, electric or magnetic perturbation or fluctuation causing changes to the structure, properties, phase of the material including self-assembly. Prominent in many such systems is a partial ordering with associated viscoelastic properties, topological and geometric complexity and long relaxations linked to broken symmetries and/or supramolecular assembling [2]. The mesoscopic scale of their physical structure allow for observing single particles, their behavior in time and under external perturbation as well as their particle-particle interactions. In addition, we can tune their particle interaction, for example, in colloidal suspension and model them in a way that does not necessarily have to account for every atomic scale details. Compared to several other hard-condensed matter systems such as crystalline solids, insulators, metals and superconductors, they are good candidates for studying physical behavior at the micro- and nano-scales.

Several external fields such as acoustic, optical, gravity, electric and magnetic fields can be used to perturb and actuate soft matter systems. Among these, magnetic fields offers the highest manipulation forces and torques in terms of the length scale of soft matter particles i.e. cells, bacteria, colloids and nanoparticles over which they are applicable with a safe and biologically friendly ability [3]. Magnetic field studies have also been proven to be a very important tool for exploring the electronic structure of condensed matter system [4]. Magnetic torques therefore enable orientation, assembly and manipulation of a broad category of materials *e.g.* biomaterials, polymer solutions, fluids and are a promising tool in new soft matter technologies [3]. To this end and cardinal to this thesis, I apply magnetic fields to two fundamental systems where: **(a)** Particle interactions induce self-assembly patterns/phenomena - Thermodynamic equilibrium structures are studied and characterized, **(b)** Fabricated magnetic patterns induce motion of particles - Topologically protected transport of the particles is established.

Many physical systems such as domains in magnetic solids, 2D ferromagnetic layers, dipolar Langmuir films, magnetic garnet films, ferrofluid and other dispersion

of magnetic particles under small electric or magnetic perturbation exhibit phase modulations in their structural properties [5, 6]. Ferrofluids for example are a suspension of single domain magnetic particles stabilized in a liquid carrier. Typically, it is composed of magnetite ( $\text{Fe}_2\text{O}_3$ ) nanosized ( $\sim 10$  nm) particles coated with a surfactant ( $\sim 2$  nm) to prevent agglomeration and suspended in a liquid carrier such as hydrocarbons, ester, water, and kerosene. A thin layer of ferrofluid exhibits modulated phases in the presence of an external magnetic field. The magnetic particles within the fluid turn to reorient themselves in a head-to-tail arrangement forming chains in the direction parallel to the applied field within the liquid carrier. In the first part of this thesis and in system **(a)**, I induce phase modulation of a critical ferrofluid mixture using external magnetic fields, which has not been reported previously. The focus here is to provide an understanding of the fundamental physics of the phase separation and modulated phases as observed.

The critical mixture here is composed of ferrofluid, lutidine<sup>1</sup> and silicone oil. Particularly, the critical demixing behavior of Lutidine-water [7, 8] stimulated the discovery of this critical ferrofluid mixture whose phase behavior I present in this work. A mixture of Lutidine-water at percentage composition of 28% and 72% respectively has a low critical solution temperature (LCST) of  $34.1^\circ\text{C}$  [7]. This mixture shows a single phase below this temperature and separates into two distinct phases of Lutidine-rich and water-rich phase above it. Similarly, when a mixture of ferrofluid, Lutidine and silicone oil is placed on a glass slide and exposed to an external magnetic field perpendicular to the plane of the mixture, it phase separates into ferrofluid-rich and ferrofluid-poor phases. Interesting here is the fact that, this is not a simple mixture compared to that mentioned above and exhibits other modulated phases, which include phase separation with formation of mesoscopic droplets, droplets deformation, labyrinthine patterning and wrinkling of droplets.

In understanding the phase behavior and phenomena of this critical mixture due to external magnetic fields, one seeks to answer two fundamental questions of; (i) what are the conditions of phase change and (ii) the characteristics of the equilibrium textures/structures? Here, my results in publication<sup>2</sup> Pub[P1] and Pub[P2] answers appropriately to these questions. I show that this liquid mixture presents equilibrium structures under different system conditions i.e. composition of constituents, field strength, and temperature. Above a critical value of the external magnetic field  $H_c$ , the mixture phase separates with droplets of magnetic-rich phase immersed in the non-magnetic phase. Different volume concentrations of the constituents exhibit various modulated phases. Fascinating among the observed phase behaviors is the two length scale wrinkling of the equilibrated droplets when the mixture is exposed with an *air-liquid* interface on top and a liquid-substrate interface below. Wrinkling occurs in a two layer coupled system subject to shear stress e.g. in polymer thin layers and the skin epidermal layer [9, 10]. However, not much is reported of fluid mixtures or ferrofluid mixtures. Therefore, the wrinkling in this critical ferrofluid mixture is of great interest.

In all the above mentioned, the crucial question remains as what is the physical mechanism(s) driving these phase modulation? With experiments and coupled the-

---

<sup>1</sup>reference to 2, 6-dimethylpyridine

<sup>2</sup>referred to as **Pub** throughout this document

ory, I show that the critical behavior of this ferrofluid mixture is due to competition between entropy of mixing, interaction energy and interfacial tension of the modulated phases, which show a dependence on temperature, concentration, external field strength among others. The dipolar interactions between particles of the mixture form the basis for the self-assembly patterns and demixing is entropic driven. Because of these competing interaction coupled with other control parameters of the system, the extended phase of the domains (magnetic droplets) undergoing several transitions. For example, the equilibrium droplets at higher fields above the critical field  $H_c$ , will experience both long-range repulsion and short-range attraction interactions within the droplet to maintain its circular shape. The winning long-range interaction however deforms the droplet into a dog-bone shape and lead to other labyrinthine phase modulation. Wrinkling of the deformed droplets was observed to occur only when there is an *air-liquid* interface. Here the wetting behavior of the interface moves the surface region from the critical point and result in the observed wrinkles.

The modulated phase patterns of the ferrofluid mixture in this study compares to patterns of some thin layers of dipolar systems with different morphologies such as bubbles and stripes. Garnet films and Langmuir films are examples of such interesting systems with these morphologies arising from competing surface energy and long range dipole-dipole interaction [11]. Magnetic garnet films have stripes patterns of up and down magnetization at a specific temperature and zero external magnetic field but transition to bubbles at a suitable applied field and temperature. Since their discovery, they have found useful application in both research and technology. These uniaxial thin films are used in magneto-optic devices, visualization of field distribution, microwave communication [12, 13] and a useful tool for studying soft matter systems.

Recently, motion of paramagnetic colloidal particles placed above the bubble lattice of a ferrite garnet films (FGF's) using external magnetic fields has been experimentally achieved [14, 15]. The particle potential due to the magnetic field gradient of the uniaxial garnet film can be altered by an external homogeneous field in a way that result in the particle having to move along the bubble lattice. The controlled motion of particles in this fashion allow for their application in targeted drug delivery systems, transport of chemicals in microfluidic systems among others. In the second part of this thesis and fundamental system **(b)**, we lithographically fabricate uniaxial patterns similar to that of ferrite garnet films but with different symmetries where we induce *topologically protected* transport of particles.

Motion is a vital ingredient of our every world and occurs for various reasons of feeding, migration, protection etc. This is evident at multiple scales in mechanical systems, collective motion in biological systems ranging from flocking birds to swarming bacteria and in active matter [16–18]. While in active matter motion is realized due to interaction of agents or particles and converting the energy for purpose of motion, the system here is a driven one and motion is induced by an external field. The focus of this part of the thesis is to study and characterize the reliable control of motion and transport of particles using magnetic structures together with applied external magnetic torques. By doing this, I contribute to the knowledge and understanding of such a driven system and allows for their tunability

for application. Most recently, Löhr and colleagues predicted and experimentally proved the topologically protected transport of colloidal particles above a bubble and square magnetic lattices [19, 20]. This novel system offers reliable motion of particles, which are robust against both internal and external perturbations.

Motivated by the breakthrough of Löhr and colleagues where ferrite garnet films were used, we fabricated magnetic patterns of all the possible two dimensional point group symmetries i.e. proper  $C_N$  or improper  $S_N$  rotational symmetry. They each possess up and down magnetization of their domains just as the garnet films. Again with an external time-dependent field, we can modulate the potential of the particles above the magnetic patterns by moving the external field in a closed *loop* and induce motion along the lattice. The question that has already been answered and forms part of this work is what makes such a transport or motion topologically protected? In the quantum regime and true for this case, it is clear that a system is topologically protected by a *topological invariant*. These *invariants* are global properties of the system hence their inert nature to small fluctuation. In this system, the *winding number* of the external modulation loop, which is similar to the Chern number of the topological insulator protects the transport of the colloidal particles. The exact shape of the modulation loop or small variation in the shape of the loop does not affect the net transport direction of the particle so long as the winding number remains the same. I present in this thesis and in Pub [P3] an additional contribution to this topologically protected transport. We show here the crucial role of symmetry of the magnetic lattice to the protected transport and our findings points to the fact that topology and symmetry are intertwined in a non-trivial way. From experiments and theory, we establish that at a universal height of the particles above the magnetic structures, only the symmetry of the pattern is important. Together with the modulation loops of the external magnetic field, the direction and characteristics of the motion is determined. Therefore, for all the symmetry point groups, we characterize the motion into adiabatic and ratchet motion with various modulation loops of the external magnetic field.

Experiments at the micrometer scale presents a handy real-time evidence of the topologically protected transport of particles compared to the colloidal system. The predicted theory and experimental observation of the colloidal system was replicated at the macroscale. In Pub [P4], I show that the transport of millimeter-sized particles with different susceptibilities can be achieved using a simple and easy to construct set-up guided by the theory of the colloidal system. Millimeter-sized magnetic structures of different symmetries with alternating up and down magnetized domains was constructed similar to that in the colloidal system. Pumping of two types of magnetic particles, a steel ball and a superconductor along the crystallographic lattice is done using existing theory from the previous system. This validates and emphasize the robustness of the topological transport since the two systems are three orders of magnitude different.

I have organized this cumulative thesis into three chapters. Following this chapter is a summary of the publications. Chapter two is devoted to the equilibrium patterns of the critical ferrofluid mixture and chapter three to the non-equilibrium motion of particles above magnetic structures which is proven to be topologically protected and linked to symmetry. Next, I present three Appendices which gives

the details of the experiments performed describing the various set-ups, materials and methods used in arriving at the research outcomes. After my bibliography, the publications are attached stating my contributions in each case.



## Chapter 2

# Magnetic field induced phases phenomena

In this chapter, a brief account of the underlying physics and concepts that gave rise to the results of the equilibrium textures and phenomena is given. Alongside this, I present the possible connection between the research findings of the study. The first section is dedicated to the physics and mechanisms of the magnetic field induced phase separation and modulated phases of the critical ferrofluid mixture while the second is to the wrinkling behavior of the equilibrated patterns of the mixture. I conclude with an outlook on these outcomes.

## 1 Critical demixing of a ferrofluid mixture

Critical phenomena and critical properties are essential thermophysical properties of chemical compounds and their mixtures. Investigating experimentally these properties of fluids and fluid mixtures is very important for both research and engineering applications [21]. A critical state of a system being a pure substance or mixtures exhibit no phase boundaries under specified properties of temperature, composition and pressure. There are known critical points of liquid-gas, liquid-liquid, and gas-gas equilibrium (coexistence) usually represented on phase diagrams. A phase diagram for a liquid-liquid mixture, for example, is a plot that shows stable, unstable and metastable regions of the mixture as a function of composition, temperature or interaction parameter (describes the interaction energy between the constituents of the mixture). These correspond to regions where the liquids are completely miscible, a small fluctuation in temperature or composition will result in phase separation (spinodal curve) and where the two phases of the mixture coexist (binodal curve) respectively. In addition, a critical point of the mixture is determined also known as the critical solution temperature. This is the Upper or Lower Critical Solution Temperature (UCST or LCST) where UCST is the temperature below which phase separation is induced in the mixture and LCST the temperature above which same is induced as shown in figure 2.1 a).

A mixture of lutidine-water and many polymer solutions show LCST behavior. Motivated by the LCST behavior of Lutidine-water shown in figure 2.1 b), I present here a critical mixture of ferrofluid, lutidine and silicone oil which phase separates in

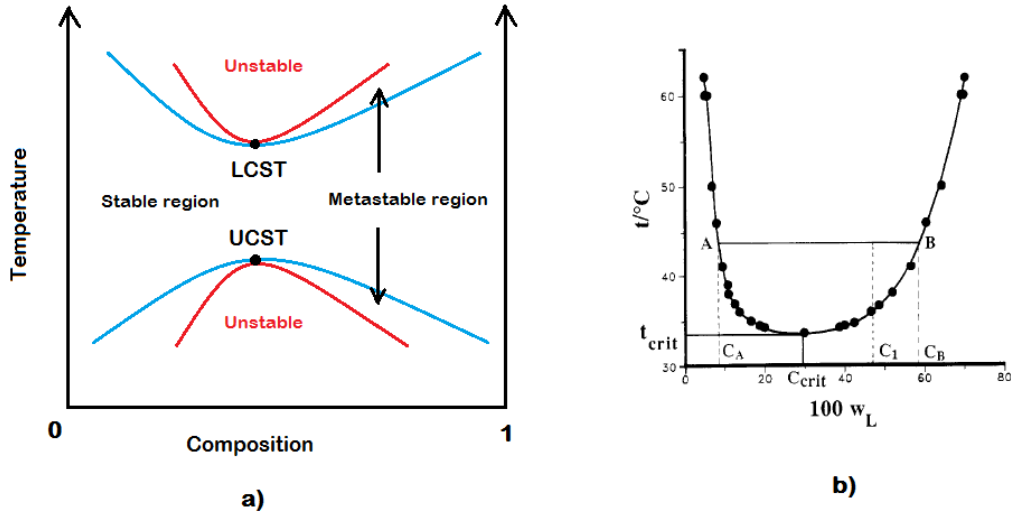


Figure 2.1: Critical point phase diagrams. a) Schematic of lower critical solution temperature and upper critical solution temperature for polymer solutions. The spinodal curve (red) show regions of unstable composition and binodal curve (blue) show coexistence regions of the two phases. The metastable region is between the spinodal and binodal curves with the critical points at the contact of both curves. b) Lower critical solution temperature behavior of Lutidine-water mixture showing the critical temperature above which the mixture will phase separate into two components with the corresponding compositions. adopted from [7].

the presence of an external magnetic field. When I surmount a critical value of the external field  $H_c$ , the mixture phase separates into ferrofluid-rich and ferrofluid-poor regions. The mixture exhibits equilibrium patterns, which depends on temperature, composition and external field strength. The hallmark of this work is the ability to induce phase separation and other modulated phases with an external magnetic field for a critical ternary mixture. A mixture of the three components is prepared and placed on a glass cover allowing a liquid-air interface above as shown in figure 2.2 a). A weak applied perpendicular field ( $\approx 10 \text{ kAm}^{-1}$ ) to the plane of the mixture will induce phase separation. The phase separation comprise droplets of the magnetic-rich phase immersed in the non-magnetic phase (see figure 2.2 b)). Details of the experiments is presented in Appendix A.1. The droplets extend from the glass substrate to the air-fluid interface and coalescence to an equilibrium size.

Due to the complexity of this system, temperature was fixed at room temperature and composition varied. Above certain critical fields ( $H_c$ ), coexisting phases were exhibited. Also, an inverse modulated phase and labyrinthine phase patterns were observed to occur at various compositions and critical fields. These phases I have presented in a ternary phase diagram in Pub[P1]. A ternary phase diagram in this case is a plot of the compositions of the three constituents showing regions of the different modulated phases as observed. Here the modulated phase of the mixture revert to its homogeneity when the external field is quenched contrary to the case

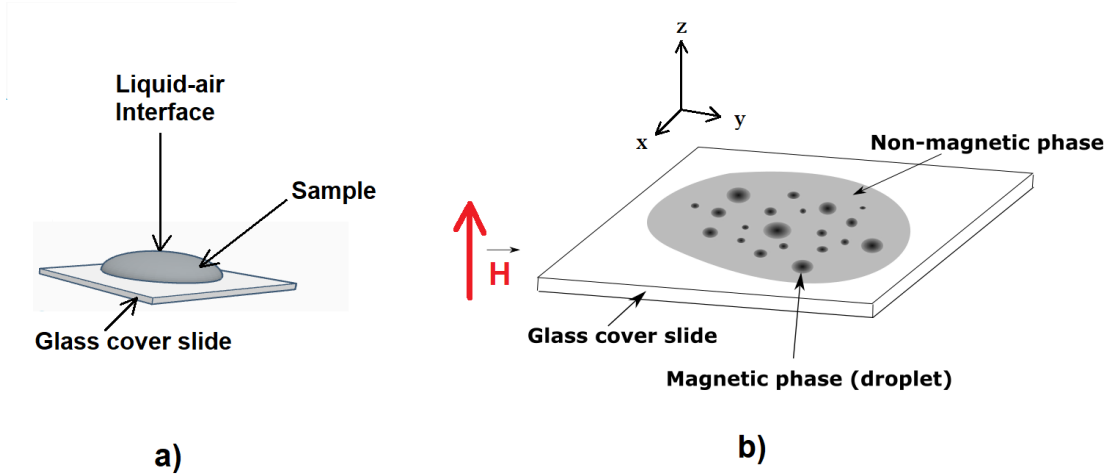


Figure 2.2: Sample and phase separation schematics. a) Side view of sample and substrate with an air-liquid interface. b) Top view of the mixture with laterally circular droplets of the magnetic phase immersed in the majority non-magnetic phase, adopted from Pub[P1].

of immiscible fluids where the phase disappear through coarsening and coalescence. Clearly, I have achieved in combining the magnetic properties of the ferrofluid and the temperature-related properties of lutidine in a way that critical parameters of magnetic field and composition induce demixing and phase modulation. Hence, a new phase behavior of a magnetic field sensitive mixture is reported.

## 1.1 Phase Separation and Thermodynamics

A thermodynamic phase transition represent a change of a state of a system due to the discontinuous change in the system's physical properties engineered by variation in external conditions. For example, liquid water transition to gaseous water where its density changes ( $\rho_l \neq \rho_g$ ) due to a change in its temperature. These transitions sometimes include the emergence of new material properties e.g. ferromagnetism, superconductivity which occur below or above certain critical parameters of temperature, pressure, electric field, magnetic fields etc. [22]. Most often, it begins microscopically with nucleation of a new phase with or without latent heat or discontinuity of state variables. Very important and a determinant is the *intermolecular forces* in such a system which is characterized by the interaction energy. This will for instance result in mixing or unmixing of components of a mixture or multi-component fluid. The aim of this study to provide an understanding of the physical mechanism for the observed mesoscopic phase separation and modulated phases of the critical mixture leads to the thermodynamic consideration of the system.

A thermodynamic state of a system can be described by a potential (i.e. free energy  $F$  or free enthalpy  $G$ ) in which case a stable phase implies a minimum of the potential as given by Gibbs-Duhem stability criterion <sup>1</sup>. Hence a stable phase or equilibrium also correspond to the maximum of entropy  $S$  where phase separation is introduced by an unstable phase with infinitesimal changes in system

parameters such as temperature. The enthalpy of mixing for a solution or mixture is a function of the interaction parameter. It describes the interaction between the components of the solution. In a regular mixture, mixing is favored when there is an attractive interaction between the different components of the mixture forming a single phase and demixing otherwise. In the case of this critical ferrofluid mixture, phase separation cannot be described in this simple way. Here, the entropy of mixing drives phase separation with contributions from the dipolar-dipolar interactions.

The demixing or phase separation mechanism of ferrofluids and their mixtures have been studied theoretically in [23], by simulation in [24, 25] using various techniques and models for inter-particle interaction such as classical Density Functional Theory (DFT). In this framework, ferrofluids have proven to form both linear chains and dense drop-like aggregates in the presence of an external field which is accounted for by dipolar-dipolar interaction of the magnetic particles. In our mixture, the intermolecular forces are not purely dipolar in nature and can not be modeled in this construction. The van der Waals (vdW) mean-field theory <sup>2</sup> for fluids is the simplest system of particles exhibiting first order transitions. However, the thermodynamic properties of such a fluid semi-quantitatively compare with measured real fluids [26]. Even in the simpler case of one-component fluids, this theory result in divergence when compared to numerical simulations [27].

In general, using fundamental quantities in describing physical properties of structure, stability, thermodynamics of colloidal fluids is cumbersome because of the different inter-particle interaction arising from solvent or carrier properties [28]. We therefore developed a thermodynamic phenomenological model that describes the observed phase modulation in experiments. At the microscopic level, we modeled our mixture as a Stock Mayer fluid composed of magnetic and non-magnetic particles. The particle interaction is therefore in two folds of dipole moment interaction and through the Lennard Jones (LJ) pair potential. The repulsive interaction between the magnetic and non-magnetic particles of the LJ potential dominates in this case but is not enough to introduce demixing. Our external magnetic field and inherent dipolar interaction come into play. The head-on-tail chain formation of the magnetic particles due to the external field is modeled by a polymerization reaction where each particle is considered a monomer and polymerize into a *magnetic polymer* stretching from the bottom of the sample to the air-liquid interface. A solution of magnetic polymers and non-magnetic solvent results from this consideration and a Flory-Huggins polymerization allows for the mesoscopic size growth of the polymers. Here, our Flory-Huggins regular mixture has a positive interaction parameter, which is the case of most polymer solution. The entropy of mixing is reduced inducing phase separation since lateral dipolar interaction are repulsive and can not account for the polymers aggregating into mesoscopic size. More detailed description of this phenomenological model is in Pub [P1].

With this, I capture both the microscopic and mesoscopic observed behavior of the phase modulation. It is due to the competition between the dipolar-dipolar interaction and the interfacial tension of the magnetic polymers and non-magnetic

---

<sup>1</sup>Gibbs-Duhem stability criterion  $\Delta U + p\Delta V - T\Delta S \geq 0$  where U, p, V, T, S are thermodynamic variables of internal energy, pressure, volume, temperature and entropy respectively [22]

<sup>2</sup>formulated by Johannes Diderik van der Waals, Nobel prize in Physics 1910

phase of the system leading to a reduction in entropy thereby exhibiting modulated phases of the mixture.

## 2 Wrinkling in ferrofluid mixture

One characteristic behavior of the equilibrated magnetic-rich droplets in the phase separation of the mixture described above in section 1 and presented in Pub [P1] is the ability to deform a laterally circular droplet (see figure 2.2 b)) to a dog-bone shape. This deformation takes place by stepwise increasing the magnetic field above the critical field ( $H_c$ ) at an adiabatic rate of  $\approx 33 \text{ Ams}^{-1}$ . Stimulated by this behavior, I further studied the modulated phase at fields above  $H_c$  and different conditions of substrate. A transition from dog-bone shape of the droplet to labyrinth pattern was observed increasing the field above a certain critical value ( $H_{lab}$ ) where the labyrinth droplet continues to grow at both ends stretching itself and undulating within the non-magnetic phase. On further increment of the field above  $H_{lab}$ , and exceeding another critical value ( $H_{wr}$ ), *wrinkling* of the labyrinth droplet occurs besides its lateral growth. A behavior that proves new in a critical mixture.

Labyrinth pattern formation in magnetic fluids, ferrofluid labyrinthine instability and their evolution from droplets has been known and reported in [5] and [29]. Also the experiments of [30] studied the evolution of two lobed (dumbbell) to multi-lobed labyrinths structures in magnetic fluids. These observation were made either in a *Hele-Shaw Cell* or between two solid plates. Contrary to this, the transition from circular droplet through dog-bone shape to labyrinth pattern observed in this study was performed on a single plate or substrate (figure 2.2 a)). Additionally, we used relatively low fields, one order of magnitude compared to [30] in realizing this shape changeover in our experiments therefore presenting a new feature. The wrinkling behavior of the labyrinth droplets of the ferrofluid mixture prompted attention. Hence, the characteristics and properties of this wrinkling we have studied and presented in Pub [P2].

A wrinkle is a fold or ridge of an initially smooth surface. Wrinkling phenomenon occurs in our everyday lives. This may appear in nanometer to millimeter length scales in materials such as thin polymer film and human skin respectively. Material science in the past viewed wrinkling as a mechanism of failure but has since been found useful in controllable and tunable application e.g. materials properties measurements, adhesion, wetting, photonics and electronics [31]. Wrinkling is a response of a material to shear stress or strain, which take place in different length scales. This mechanical instability has been studied in solids, thin polymer films and human skin but not so much in fluids and their mixtures.

In Pub [P2], I investigated the wrinkling of a critical demixing ferrofluid mixture at fields above the critical demixing field ( $H_c$ ) described in the previous section. The wrinkling behavior is preceded by a circular droplet - dog-bone - labyrinth deformation. This peculiar behavior is attributed to the competing long-range dipolar interaction and the interfacial tension/energy of the system with an *air-liquid* interface. I report two length scales of the wrinkles. These are observed in

the bulk of the mixture and at the air-liquid interface with a characteristic radius of curvature  $100\mu m$  and  $20\mu m$  respectively. The air-liquid interface caused the surface wrinkles that were totally absent in covering the sample in figure 2.2 a) with either glass or plaster (silanized and non-silanized) cover slides. This is therefore an outstanding feature of our mixture and wrinkle phenomena.

We theoretically described and characterized appropriately these wrinkles. Being guided by existing theories, we defined a wrinkle number and characterized the two length scale wrinkling of the droplets as small scale wrinkle number  $wr_<$  and large scale wrinkle  $wr_>$  number for the full length of a droplet. The small scale wrinkle number describes that of the surface wrinkles while that of the large scale is to the bulk. My experimental observation quantitatively agree with the predicted theory in this reported wrinkling behavior of the ferrofluid mixture. More details of the mathematical consideration are found in Pub [P2].

In my quest to further understand the behavior of the equilibrated droplets and wrinkles, I superposed a low frequency oscillating field (coupled  $x$  and  $y$  plane) on the already static perpendicular field to the sample plane in figure 2.2 b). The droplets were observed to oscillate (rotate) at approximately the frequency of the oscillating field. This was however not the case above field strength of  $1.9 \text{ kA/m}$  and frequency  $10 \text{ Hz}$  were the droplet disintegrate into the non-magnetic phase as expected. Based on this idea, I could extend or elongate the wrinkled phase with superposed lateral ( $x$  or  $y$  plane) fields. At this geometry, the wrinkles are lost and the elongated structure relaxes to the wrinkled state when the lateral field (elongating field) is quenched. I measured such relaxation times and compared with theory.

### 3 Conclusion and outlook

A critical ferrofluid mixture exhibits modulated phases above a critical value of an external magnetic field and at a specific composition and temperature. It phase separates with droplets of magnetic-rich phase immersed in the non-magnetic majority phase. The observed mesoscopic droplets arise due to magnetic particles chain formation in the direction of the perpendicular field to the plane of the sample and subsequently coalescence and grow to a stable size. The dipolar-dipolar interaction of the magnetic particles and the interfacial tension effects of the non-magnetic phase leads to a reduction in entropy of mixing and phase separation. A wrinkling behavior of the ferrofluid rich droplets of the mixture was identified and characterized by two length scales. The predicted theory compares with experiments and opens a new opportunity to an understanding of wrinkles in fluids and their mixture.

A further understanding of effects of time-varying fields on the magnetic droplets, labyrinth and wrinkled modulated phases will help comprehensively describe the behavior of this critical ferrofluid mixture. In addition, a careful study of emergent properties and characteristics of the system after phase separation is a step in consolidating my knowledge and understanding of this system. Since temperature was fixed in this experiment, the temperature dependent behavior of the modulated

phases will be desirable. This will enhance their possible application in biotechnology, bioengineering and industry for extraction/separation of cells, proteins and materials in general.



## Chapter 3

# Topologically protected transport

The discoveries of the 2016 Physics Nobel Laureates<sup>1</sup> opened a new frontier in condensed matter physics where matter can exist in exotic states [32]. Their theories, predictions and discovery of topological phase transitions and topological phases of matter has paved the way for topological insulators, topological superconductors, topological metals, among others, which are continuously being explored. My work in this thesis to understand the motion and manipulation of particles (colloids) using external magnetic fields and magnetic structures presented a coupling with topology. This new feature of topological concepts incorporated in an external field controlled motion of magnetic particles is the main output of this chapter. Here, we use concepts of topological protection to achieve microscopic transport (colloids) and macroscopic transport of particles using externally modulated fields. It is proved more robust and reliable than previously known mechanism of transport using external driving forces.

Topology is the study of properties of geometric figures which remain intact after a distortion and is commonly referred to as "*rubber sheet geometry*" [33]. We can use topological methods to identify gross features such as holes or know a geometric figure is made up disjoint pieces [34]. Topological protection is deeply rooted in physics of quantum mechanics, which can be explained with topological invariants that are closely related to the quantum Hall effect. For that matter, I will first give a brief account of these relevant concepts that come into play in describing this transport phenomenon. Following this, I present highlights of the experimental and theoretical findings of Pub [P3] and Pub [P4] and conclude the chapter with future exploration of the phenomena.

## Quantum Hall Effect, Topological invariants and Protection

The Hall effect was discovered by H. E. Hall in 1879 [35] who observed that a thin flat conductor subjected to an electric current ( $\mathbf{I}$ ) and a perpendicular magnetic field ( $\mathbf{B}$ ) will result in a measurable Hall Voltage ( $V_H$ ) and a transverse resistance

---

<sup>1</sup>Nobel prize in Physics 2016: David J. Thouless, F. Duncan M. Haldane and J. Michael Kosterlitz

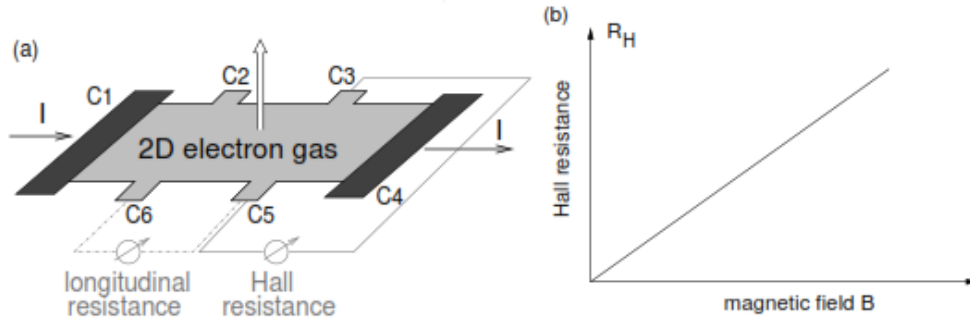


Figure 3.1: (a) A typical Quantum Hall effect system, current  $I$  flow between terminal C1 and C4. The measurement of the Hall and longitudinal resistance are indicated accordingly. (b) Plot of the Classical Hall resistance (*Hall Coefficient* ( $R_H$ )) against magnetic field. Picture adopted from [36]

( $R_H$ ).

$$R_H = \frac{B}{qn} \quad (3.1)$$

This Hall resistance  $R_H$  varies linearly with the applied normal field. The measured quantity contains the fundamental microscopic information of the material being the charge of the charge carrier ( $q$ ) and carrier density ( $n$ ). It differs from the transverse (Hall) resistivity ( $\rho_{xy}$ ) by a geometry factor. The action of Newton's laws and Lorentz force on this system invalidates momentum conservation by deflecting the charge carriers in the transverse direction hence the surprising Hall conductivity. This effect has since been useful in characterizing transport properties of materials.

In the quantum realm i.e. low temperature and high magnetic field, the (quantum) Hall effect is observed in two-dimensional electron gas (2DEG) systems which can be formed at the interface between a semiconductor and oxide layer of a transistor. A discovery of the *Shubnikov-de Haas effect* in 1930 gave the first indication of quantum effects in transport measurement of 2DEG systems where the longitudinal resistance oscillates above certain critical magnetic fields [37]. Fifty years later, the Quantum Hall effect was first experimentally observed by von Klitzing, Dorda and Pepper using a 2DEG of Silicon-MOSFET (metal-oxide-semiconductor field-effect transistor) at helium temperatures and a strong magnetic field ( $\sim 15$  T) [38]. A typical set up for such an experiment is shown in figure 3.1 a). Their work proved that the quantization of electrons' circular orbits with cyclotron frequency  $\omega_c$  results in quantized Landau levels with energy  $\epsilon_m = \hbar\omega_c(n + \frac{1}{2})$ . This leads to a quantized Hall conductance ( $1/\rho_{xy}$ )

$$\sigma_{xy} = N \frac{e^2}{h} \quad (3.2)$$

when the Fermi energy lies in a gap between two Landau levels <sup>2</sup>. It is expressed

in terms of universal constants and multiples of  $e^2/h$ .  $N$  is the filling factor which takes integer values  $N = 1, 2, \dots$  hence the name Integer Quantum Hall Effect (IQHE). The quantization of the Hall conductance  $\sigma_{xy}$  has been subsequently measured to an extraordinary precision (1 part in  $10^9$ ) an indication of its topological nature [40]. A lot of studies has since been done on the theory of quantum Hall effect where the strong magnetic field leads to mixing of Landau levels by disorder or by electron-electron interaction being considered as a weak perturbation [41]. In considering a non-interacting electron gas, mixing of the Landau levels is due to disorder leading to IQHE. Fractional Quantum Hall Effect (FQHE) <sup>3</sup> is the case where electron-electron correlation is considered and the filling factor  $N$  in equation (3.2) assumes fractional values.

In 1982, Thouless and colleagues theoretical explained the quantization of the Hall conductance after its experimental observation and measurement [39]. What is important here and groundbreaking is that they derived an expression for the Hall conductance that emphasize its connection to topology [39]. In order to appreciate the connection between Hall conductance and topology, two essential concepts are prominent; *topological invariants* and topological band theory. In mathematics and topology, a topological invariant is a property of a topological space, which is preserved under homeomorphisms. That is this property does not change for equivalence classes and one can continuously deform one space into another of the same class. Intense theoretical survey has concluded that the Hall conductance is represented by a topological invariant usually an integer for a 2D periodic system in the presence of a magnetic field [42].

In topological band theory, it is known that the magnetic field breaks translational symmetry of the crystal and the electron states are specified with a vector in reciprocal space, crystal momentum  $\mathbf{k}$  in a periodic Brillouin zone (topologically a torus  $T^2$ ). The Bloch wave function  $|u_m(\mathbf{k})\rangle$  just like in an ordinary crystal lattice constitute the eigenstates of the Bloch Hamiltonian  $\mathcal{H}(\mathbf{k})$  and the eigenvalues  $E_m(\mathbf{k})$  together form the band structure. It is possible to classify topologically gapped band structures for equivalence classes of the Bloch Hamiltonian  $\mathcal{H}(\mathbf{k})$  which can be continuously deformed into one another without band gap closure or quantum phase transition [40]. These classes are differentiated by a topological invariant which has its root in mathematics of fiber bundles. This invariant is the Chern number  $n$  and can be explained physically with the Berry phase which in turn is connected to the Bloch wave function [43]. The value of the Chern number only changes under drastic variation of the Bloch Hamiltonian  $\mathcal{H}(\mathbf{k})$  implying band gap closure. The work of Thouless and colleagues showed that the integer-valued Chern number  $n$  is identical to the filling factor  $N$  of the quantized Hall conductance  $\sigma_{xy}$ . It explains the fact that  $\sigma_{xy}$  is robust against perturbation such as disorder or electron-electron interaction hence a *topological invariant* [32].

The most remarkable achievements of the topological band theory is the prediction of the exotic state of matter Topological insulator (TI) [44]. It is an electronic material with the Fermi level in a bulk band gap and conducting edge or surface

---

<sup>2</sup>It has been shown from Laughlin's arguments that Hall conductance is quantized even when the Fermi energy lie in a gap within Landau levels [39]

<sup>3</sup>Discovered by Tsui, Störmer and Gossard in 1982

states. The edge channels in the 2D IQHE discussed above is closely related to the surface or edge states of the discovered novel topological insulator. The gapless states in this topological insulator are protected by a topological invariant and the fundamental distinction between such a quantum Hall state and an ordinary insulator relies on the topology of the system. A physical property that depends only on a topological invariant is *topologically protected*. A topologically protected property of such a system is insensitive to perturbation due to this topological invariant.

A topological invariant that can easily be understood in terms of two-dimensional surfaces is the *genus*  $g$ . We can also classify 2D surfaces, which have topological equivalence classes distinguished by the genus. It is just the number of holes each 2D surface possess. Example is the sphere being homeomorphic to a hockey puck and drinking glass all being  $g = 0$  whereas that of a donut is to the inner tube and coffee cup characterized by  $g = 1$ . This integer valued *genus* is a topological global property of the system but geometric properties such as curvature are local in nature. However integrating such local properties (integral over a closed orientable manifold) may characterize a global property. Therefore, the Chern number is closely related to the *genus* since it is an integral of the Berry curvature and the genus gives a simple understanding of the topological invariant.

Another topological invariant in terms of the Chern number and Bloch Hamiltonian  $\mathcal{H}(\mathbf{k})$  that can be intuitively understood is the *winding number*  $\nu$ . *winding number* is the number of times the vector field  $\mathbf{d}(\mathbf{k})$  winds around on a closed loop in the  $\mathbf{k}$ -space as  $\mathbf{k}$  goes through the Brillouin zone. Just as the Hall conductance and for that matter the Chern number changes sign for a topological phase transition, same is the case for the topological invariant of *winding number* since we can distinguish between clockwise and counterclockwise paths. This becomes clear in the different winding numbers due to the topology of our system. The above topological invariants are prominent and show relevance in characterizing and describing the topologically protected transport in this work. Particularly, the winding number of the modulation of the external magnetic field which I will show in the next section, is the topological invariants protecting the transport.

## 1 Microscopic transport of colloidal particles

Quantum Hall effect and its chiral edge or surface states have been understood to be protected by topological invariants making them robust against perturbation. Discovery of Topological Insulators (TIs) comes in the light of this scientific advancement and since paved the way for theoretical prediction and experimental discovery of many 2D and 3D solid-state materials exhibiting such exotic quantum phenomena. The underlying principle is the topology of the band structure leading to the topological classification of phases. This classification is currently found not to be limited to quantum systems but include many classical wave-like systems.

In this work, the concept of topological protection is applied to a non-Hamiltonian system. The dissipative transport of colloids above a modulated periodic magnetic potential is achieved. This transport of particles (paramagnetic and diamagnetic) is characterized by the topology of the modulation loops of the external

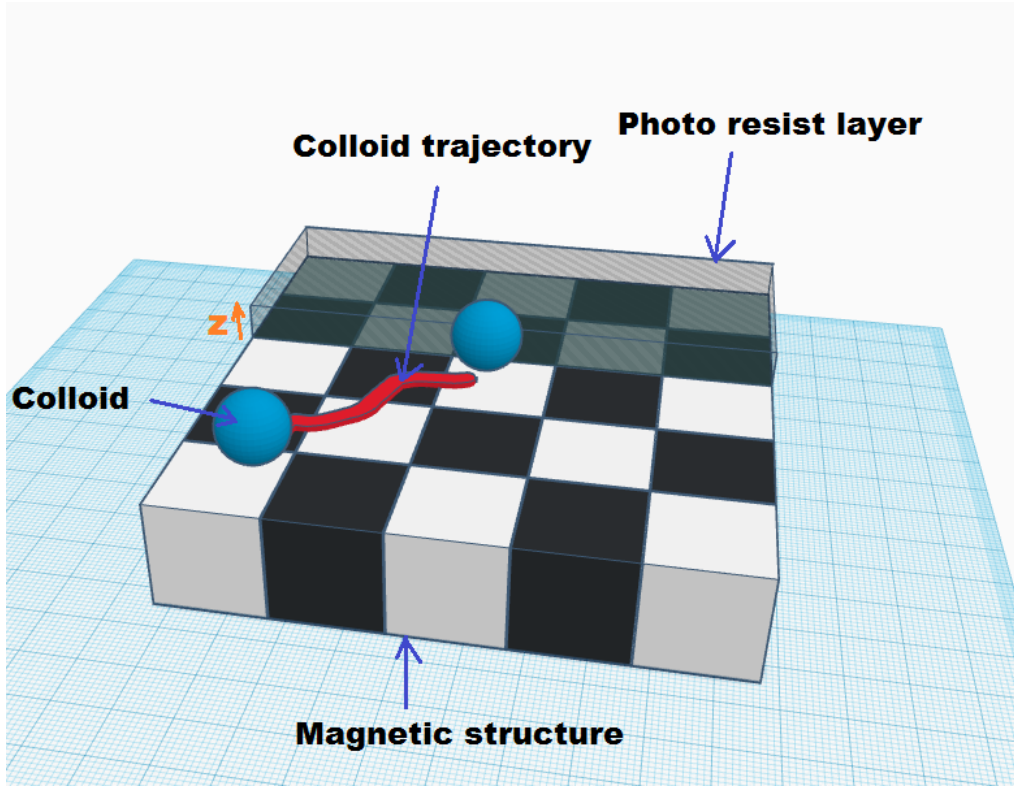


Figure 3.2: 3D schematic of colloids and magnetic structures. The domains of the four fold symmetry magnetic structure are up (white) and down (black) magnetized. The photo resist layer gives the desired universal height  $z$  above which the colloids move.

magnetic field and that of the mathematical manifold on which they are transported. The focus of this study is to emphasize the role of symmetry and topology on the transport modes of the colloids hence we considered all possible two-dimensional magnetic lattices symmetry point groups.

The experiments consist of colloids placed above a two-dimensional magnetic structure which has periodic domains. These domains alternating up and down magnetized generate magnetic field gradients above the structure. When an external time-dependent magnetic field is applied in a specific form, it modulates the field of the structures in a way that causes the colloids to move from one unit cell to another along the lattice as shown in figure 3.2. The space of the 2D magnetic structure on which the colloids are placed and transported we define as Action space  $\mathcal{A}$ , figure 3.3 a). The set of all points in space corresponding to all the directions of the external field is what we call the Control space  $\mathcal{C}$ . It is a sphere of the external field with constant magnitude. The closed loop in control space  $\mathcal{L}_{\mathcal{C}}$  as shown in figure 3.3 b), is an example of a loop we move the external field such that we modulate the colloidal potential to induce motion. These loops are characterized by the winding number  $w(\mathcal{L}_{\mathcal{C}})$  around a hole or special objects in control space.

Magnetic thin films with different symmetries of the lattice having proper  $C_N$  or improper  $S_N$  rotational symmetry were used. Broadly, our experiments were performed on a proper  $C_2$ ,  $C_4$ ,  $C_6$  and improper  $S_6$  ( $C_3$ ) lattices with magnetized

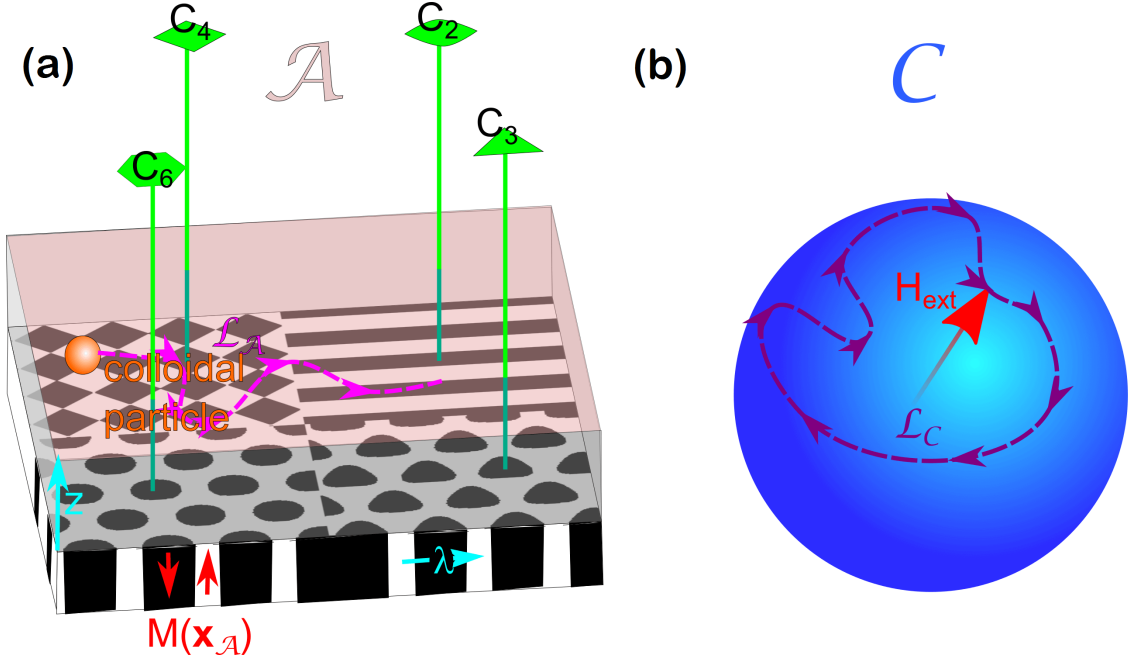


Figure 3.3: a) Action space  $\mathcal{A}$  for the different lattices,  $C_N$  ( $N = 2, 3, 4, 6$ ) rotational symmetries above which the magnetic colloids are transported at a universal height  $z > \lambda$ . The wavelength of the lattice  $\lambda$  is the same for all the symmetries with up and down magnetization  $M(\mathbf{x}_A)$ . b) Control space  $\mathcal{C}$  with an external field modulation loop  $\mathcal{L}_C$  resulting in action space loop  $\mathcal{L}_A$  and transport of a colloidal particle in  $\mathcal{A}$ . Adopted from Pub [P3].

domains (up and down) in the  $z$ -direction of the film plane (figure 3.3 a)). The position of the particles is described by a vector  $\mathbf{x}_A$  in the lattice plane in Action space  $\mathcal{A}$ . Action space  $\mathcal{A}$  is topologically a torus ( $g = 1$ ) using periodic boundary conditions of the unit cell. The colloids are transported at a fixed elevation ( $z > \lambda$ )<sup>4</sup> above the lattice in action space.

Our magnetic thin structures produce a magnetic field which is defined as

$$\mathbf{H}_p = -\nabla\psi \quad (3.3)$$

This pattern field  $\mathbf{H}_p$  can be obtained from a magnetic scalar potential that can be written as a Fourier series and fulfills the Laplace equation. It follows that the colloids on top of these structures with effective susceptibility  $\chi_{\text{eff}}$  and volume  $V$  will acquire magnetic moments and potential energy;

$$\mathbf{m} = \chi_{\text{eff}}V\mathbf{H} \quad , \quad E = -\chi_{\text{eff}}V\mathbf{H}^2 \quad (3.4)$$

where we define the colloidal potential as  $U_m = \mathbf{H}^2$ . Since we modulate the colloidal potential with an external field, the total field  $\mathbf{H}$  is a sum of both the pattern

<sup>4</sup>We focus on attaining a universal elevation at which the detail of the pattern of the magnetic film is irrelevant to the movement of the colloidal particles except its symmetry. It is universal because at high  $z$  values, the only important contribution to the magnetic potential is the lowest reciprocal lattice vector  $\mathbf{Q}$ . This is achieved by magnetic levitation of the colloids in a ferrofluid or coating the film with a polymer film of defined thickness [19]

field and external time-dependent field  $\mathbf{H} = \mathbf{H}_p + \mathbf{H}_{ext}$ . The space of the external magnetic field constitute our control space  $\mathcal{C}$  (figure 3.3 b)) which by definition has a constant magnitude. At the desired universal elevation, the universal colloidal potential can be expressed as (see Pub [P3] for detail mathematical consideration)

$$U^* = e^{Qz} \mathbf{H}_{ext} \cdot \mathbf{H}^p(\mathbf{x}_A). \quad (3.5)$$

Depending on the susceptibility of the colloids, they will move to the maximum (paramagnetic) or minimum (diamagnetic) of the universal potential if we modulate it with the external field causing transport along the lattice of the film.

What is important here is to identify, characterize and classify the modulation of the external field  $\mathcal{L}_C$  that will result in transport along the various directions of the crystallographic lattice in action space  $\mathcal{A}$ . The full dynamics of this system is described by the mathematical stationary manifold  $\mathcal{M}$  which is a two-dimensional manifold in product space  $\mathcal{C} \otimes \mathcal{A}$  [19]. Such a manifold is characterized by a topological invariant the *genus*  $g$  and takes different values for the different symmetry lattice groups. The manifolds of the  $C_2$  and  $C_4$  lattices are 2D surface with genus 2 and 5 respectively whereas that for the  $C_3(S_6)$  and  $C_6$  lattices are genus 7 surfaces.

The winding number  $w$  of the modulation loop in control space (the loop that the external field traces, see figure 3.3 b)) and in action space is the topological invariant that protects the transport of these particles. Hence, modulation loops of the same winding number can be continuously deformed into one another forming the basis for the classification of these loops. Crucial to this classification is to identify modulation loops in control space  $\mathcal{L}_C$  that will translate into action space loops  $\mathcal{L}_A$  with different non-zero winding numbers in action space resulting in transport.

The complexity of action space and corresponding control space of the various symmetry groups makes this task crafty. For example, the two fold symmetry ( $C_2$ ) has an action space topologically a genus 1 surface<sup>5</sup>(a circle) whereas control space is a genus 0 surface (a sphere). Therefore, modulation loops of the two spaces are not homeomorphic to one another. However, considering the quasi one dimensional nature of the lattice and the fact that in-plane field perpendicular to the only important reciprocal lattice vector  $\mathbf{Q}$  is irrelevant, we construct a reduced control space  $\mathcal{C}^r$  which is now a circle. It is the grand circle on control space around the axis of the in-plane field. For this case, we proved that

$$w(\mathcal{L}_A) = w(\mathcal{L}_{C^r}) \quad (3.6)$$

satisfies the condition for transport in action space at a universal elevation.

To this end, the problem is similar for the other symmetry groups ( $C_3$ ,  $C_4$  and  $C_6$ ) where action space is a genus 1 surface (a torus) but again control space a genus 0 surface. We mathematically identified objects on control space around which we modulate our external field making it non-trivial. The theory of these objects are given in detail in Pub [P3]. By doing this we obtained a constrained control space  $\mathcal{C}$  such that modulation loops with winding numbers

---

<sup>5</sup>This is also true for all other symmetries where folding the edges of the Brillouin zone we get a torus ( $g = 1$ ).

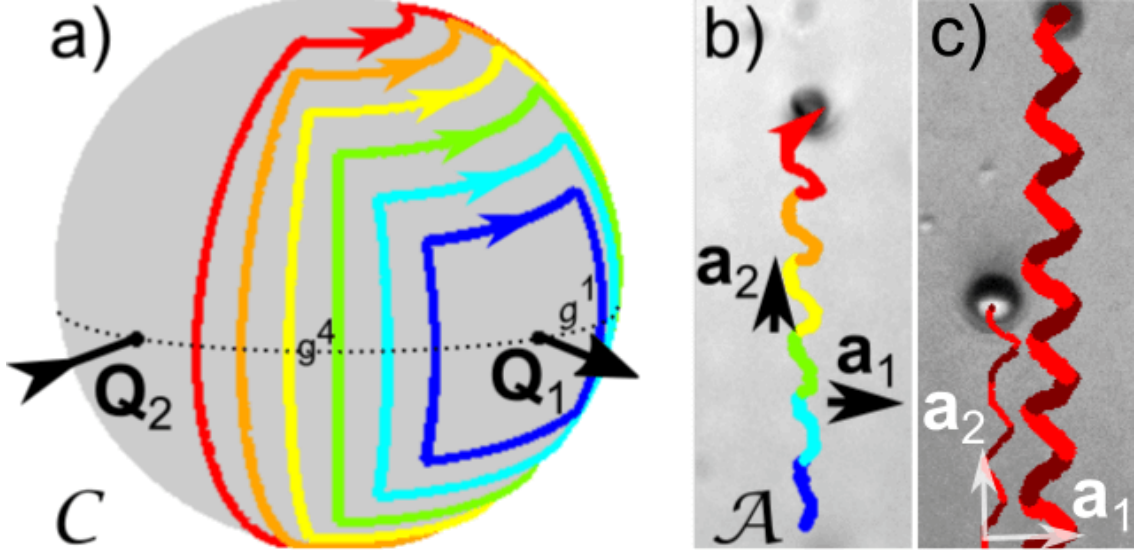


Figure 3.4: Experimental results of the four fold symmetry. a) Control space with modulation loops of the same winding number but different proximity around fence point in the  $\mathbf{Q}_1$  direction. b) Action space showing the corresponding travel path of a paramagnetic particle in the  $\mathbf{a}_2$  direction due to the modulation loops in a). c) Transport trajectories of a diamagnetic particle (left) and paramagnetic (right) due to largest loop (red) in a). The paths show a shift by  $\mathbf{d} = 1/2(\mathbf{a}_1 + \mathbf{a}_2)$ . Due to lithographic effect and the ferrofluid, the reflective microscopic images are not able to capture the background structure of the magnetic patterns but they possess a lattice constant  $a = 7 \mu\text{m}$ . Adapted from Pub [P3].

$$w(\mathcal{L}_{\mathcal{A}}) = w(\mathcal{L}_{\bar{\mathcal{C}}}) \quad (3.7)$$

will result in the particle moving from one unit cell to the other in action space. Below, I give some results of the four fold symmetry experiments that confirms these theories.

In figure 3.4 a), we apply modulation loops that winds around a special object in the  $\mathbf{Q}_1$  direction in control space which we call the fence point. These modulation loops all have the same winding number  $w$  regardless of their closeness to the said fence point. Interesting in each case is the transport of the particle a unit cell upon completion of each loop. This emphasize the fact that the transport is robust against small perturbation since the exact shape of the loop is irrelevant and protected by the winding number. The only visible distinction is the more linear nature of particle path for loops much closer to the fence point (see figure 3.4 b))

We can transport particles with different effective susceptibilities (paramagnetic and diamagnetic) using a modulation loop with the same winding number. To achieve effective diamagnetism of the non-magnetic particles, we immerse both type of particles in a ferrofluid. We obtain transport of both particles in the same direction for the four fold symmetry case but with a shift in their trajectories as predicted by theory (see figure 3.4 c)). Finally, the topologically protected transport of colloidal particles has also been characterized to be either adiabatic or ratchet in

nature. Ratchet motion occurs with jumps of the particle with a speed uncorrelated to that of the modulation loop causing the transport contrary to adiabatic motion. The results of the transport modes of the experiments alongside the predicted theory shows dependence on symmetry hence establishing a link between symmetry and topology in this system. This is fully described for the different symmetries in attached Pub [P3] in Appendix P3 below.

## 2 Macroscopic transport of particles

The results of the topologically protected transport colloidal system briefly discussed in Section 1 inspired the up scaling from micrometer ( $\mu m$ ) to millimeter ( $mm$ ) scale of the experiments guided by the existing theory. I study the topologically protected transport of a crystalline steel and superconductor pump. The experimentation at this scale presents a simple advantage of observing both the external field and particles during the protected transport compared to the colloidal system. The focus here is to emphasize and further consolidate the robustness of the predicted theory and experimentally verified concepts allowing for engineering applications.

Two-dimensional magnetic patterns constructed in proper four fold  $C_4$ , proper six fold  $C_6$  and improper  $S_6$  six fold symmetries made from NbB magnets with lattice constant 2.82 mm, 4.33 mm and 5.20 mm respectively were employed in this study. Universality of the two-dimensional magnetic potential of a 1.0 mm steel and superconductor sphere in this case was achieved by placing spacers of defined thickness between the pattern and particles. This ensures that the symmetry of the pattern is relevant not the details. The external magnetic field was also generated from two parallel permanent NbB magnets and together with the magnetic patterns arranged in a *Goniometer* geometry (see Appendix A.3). Just as in the colloidal system, transport occurs when we modulate the potential with the external field by reorienting it relative to the periodic magnetic crystal around specific objects (points, lines or areas) in control space. An advantage here is, the ability to trace out these areas or objects with the aid of a laser pointer attached to the goniometer.

Based on the winding number of the modulation loops, we classify non-trivial transport and characterized them as adiabatic or ratchet. Exciting is the observed irreversible ratchet motion in the  $S_6$  symmetry lattice which was not achieved in the previous experiments with the colloidal system. The effect of noise arising from the magnetic structures in the colloidal system accounted for this feature, which is drastically reduced in the macroscopic system allowing for observation of these irreversible ratchets. However, a hysteresis was observed in the nature of the gates (special lines in  $\mathcal{C}$ ) in  $C_4$  symmetry and fence segments (special areas in  $\mathcal{C}$ ) in  $S_6$  symmetry contrary to the theory in the colloidal system. This discrepancy is due to the solid friction in this macroscopic system. We can also pump both the steel (paramagnetic) and superconductor (diamagnetic<sup>6</sup>) sphere into the same or different directions depending on the symmetry of the pattern and external modulation. Both theory and experiments agree at this macroscopic scale of the topologically

protected transport.

### 3 Conclusion and outlook

We employ the concept of topological invariants and protection to achieve a robust microscope/macrosopic transport of colloids/particles. The magnetic potential of the microscopic and macrosopic magnetic patterns with different symmetries is modulated with an external magnetic field which we characterize and classify using the winding number of the loops. We theoretically described this classification and the experimental outcomes favorably agrees with the former. We used patterns of different symmetries in experiments and could highlight the deep connection between geometry and topology in this transport mechanism. Based on microscopic findings, we extended the concept to a macrosopic scale where a Floquet topological crystalline pumping of a steel and superconductor ball was achieved.

From the theory and experimental findings of this study, we established that particles with  $\chi_{eff} > 0$  (paramagnetic) and  $\chi_{eff} < 0$  (diamagnetic) will follow the maximum and the minimum of the colloidal universal potential respectively. In a future work, it will be exciting and instructive to understand what will happen to a particle that is neither diamagnetic nor paramagnetic e.g. a particle comprising of two diamagnetic and two paramagnetic particles in this system. This we forehand speculate will be restrained to the saddle points of the potential. Preliminary experiments at the macrosopic scale have already commenced by gluing two steel and two superconductors each of 1.0 mm into an octupole. However, this saddle point behavior was difficult to observe since the size of the octupole was approximately the size of the lattice constant. Also, our theoretical prediction that on inverting or rotating the external field by  $180^\circ$  the orientation of the octupole changes by  $90^\circ$ , and its position around the interstitial area of the magnetic structure should change by  $360^\circ$  in comparison to the quantum mechanical *Anyons* was also not observed. The susceptibility of the steel ball dominated even for tiny sizes of 0.6 mm making the octupole effective paramagnetic.

A further experimental understanding of this saddle point phenomena using the micrometer scale set up of the colloidal system is a promising way to go. It will enhance the comprehensive description of this interesting transport mechanism and contribute to the knowledge and understanding of such a system.

---

<sup>6</sup>Superconductivity is achieved by immersing both particle in liquid nitrogen

# Appendix A

## Materials and Methods

The experimental results for this thesis were obtained using commonly known soft matter instrumentation and techniques with custom designed materials and innovative methods. I highlight in this chapter the essential materials, experimental set up and methods that were employed in this regard. In general, optical microscopy was the major tool used in observing and recording the equilibrium mesoscopic structures of the critical ferrofluid mixture and the microscopic motion of the topologically protected transport phenomena. However, the rather simple case of the macroscopic transport or pumping of the millimeter-sized particles was recorded with a simple digital camera.

The materials and methods for the ferrofluid modulated phase phenomena and wrinkling behavior is given in Appendix A.1, that for the microscopic topological transport in Appendix A.2, and the macroscopic Floquet pump in Appendix A.3 below.

### A.1 Field induced Self Assembly patterns

The set up for observing the critical demixing and modulated phases of the ferrofluid mixture was done with a *Leica DMLP* polarization microscope with a mounted charge-coupled device (CCD) *Leica DFC365FX* camera. Particularly, the demixing phase and droplets deformation were observed in transmittance illumination mode whereas the wrinkling behavior in reflectance mode. A sample of the mixture is prepared, pipetted onto the desired substrate and placed on top of an aluminum block on the stage of the microscope. This block is temperature controlled offering the ability to read and control the sample temperature. The coils generating the magnetic field and the sample are arranged in a geometry shown in a schematic in figure A.1 a) below. With the aid of the CCD camera, the texture of the mixture is viewed and recorded on a computer using a software *StreamPix 5*.

#### External Magnetic fields

The magnetic field for the study was generated from three coils. The  $z$ -direction coil coupled to a DC power supply generated the desired field strength 0 - 10 kA/m. In order to measure and record the field strength, a *Lakeshore 450* Gaussmeter

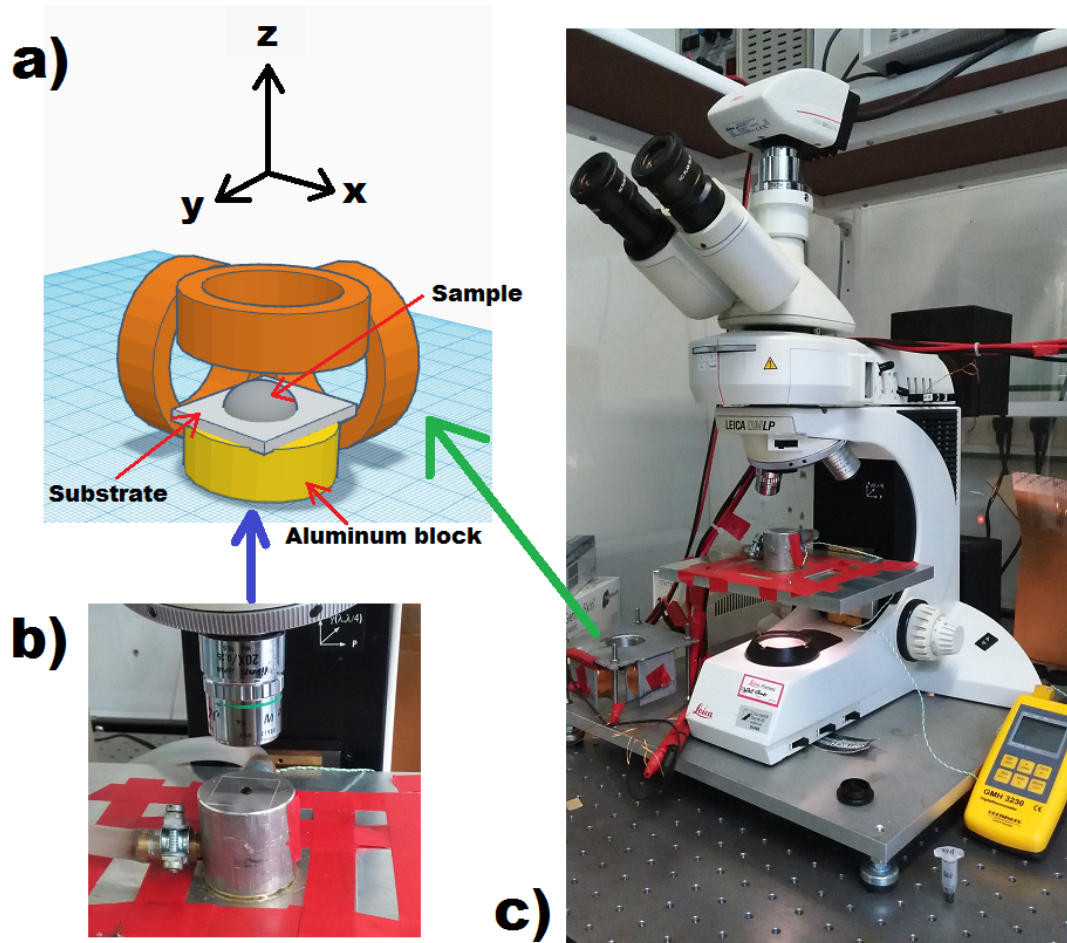


Figure A.1: Set up for Experiments. a) Schematic of Coils configuration and sample. b) Image of sample (black substance on the glass slide) placed on the temperature controlled Aluminum block with an objective lens directly above the sample. c) Image of the polarization microscope in transmittance illumination mode with the CCD camera mounted on top. A thermometer (yellow) is attached to the Aluminum block, which is mounted on the microscope stage for reading the temperature of the sample.

was incorporated into the set up. A Computer program *Tcl* controlled the power supply to the  $z$ -coil such that, the resultant applied field was increased adiabatically inducing the observed textures of the sample. An oscillating field for elongating the wrinkled droplets was produced from a  $40\text{ MHz}$  *Aim-TTi TGA 1242* waveform generator, *Tektronix TDS 2014B* oscilloscope, *Ominitronic E-200* amplifier and the  $x/y$ -coils.

## Sample

The magnetic component of the critical mixture is a ferrofluid. Ferrofluids since their discovery by Steven Pappell at NASA in the 1960s and subsequent commercialization by R. E. Rosensweig and R. Moskowitz gained great scientific attention and contributed to the understanding of fundamental properties of soft materials. They form part of a broad group of magnetic particles systems which include magnetorheological (MR) fluids and so-called magnetic holes classified based on their method of preparation and characteristics [45]. Modulation of ferrofluids and their mixtures occur in the presence of both steady and time-varying magnetic fields. The ingredients of the mixture were ester-based Ferrotec *APG 512A* ferrofluid, Sigma-Aldrich *2,6-dimethylpyridine* 98% and Fluka *Silicone oil DC 200*. A sample is prepared by measuring volume fraction ratios  $\phi_{ferro} : \phi_{lutidine} : \phi_{silicone}$  and mixing them in a test tube. Then, a drop of  $5\mu\text{l}$  of the thoroughly mixed sample is pipetted on to the appropriate substrate. A clean glass slide was used as the substrate for studying the equilibrated structures of the mixture while a silicon wafer was employed for the wrinkling behavior due to the reflectance mode of the illumination. However, other substrates such as silanized plastic and glass slides were introduced at various stages in the study.

## A.2 Topological protected microscopic transport

The experiments for the transport of colloidal particles was done with a similar array as in Appendix A.1 above. Here, a *Leica DM 2500 P* microscope (without polarizers) operated in reflectance illumination mode and a *Leica DFC360FX* camera was used. The colloidal motion was recorded using the same computer software as in Appendix A.1 and the particle trajectories and velocities were extracted using a *MATLAB* program. The sample is placed above the  $z$ -direction coil as shown in the schematic in figure A.2 a), the time-dependent field from the coupled  $x$ ,  $y$  and  $z$  coils induce motion of the colloids above the magnetic pattern in the direction predicted by theory. Other important components of the set up are briefly described below.

### Lithographic Magnetic structures

The magnetic patterns/structures are made of magnetic domains magnetized perpendicular to the surface in alternating up and down directions. The magnetic patterns for the experiments were lithographically made to possess the different symmetries *i.e.* two-, three-, four-, and six fold. They were created in Poznań

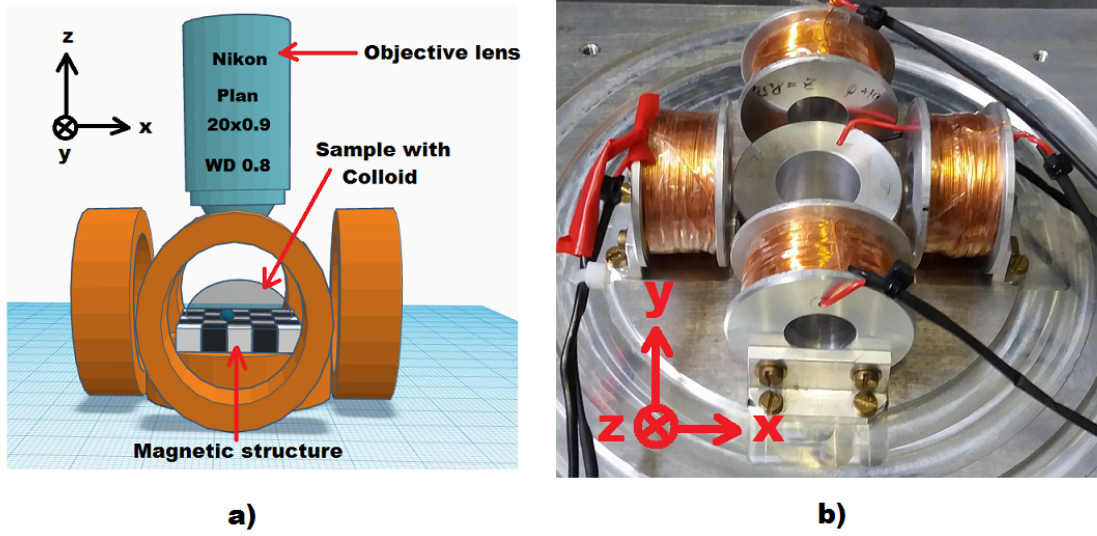


Figure A.2: Experimental set up for transport of colloidal particles. a) 3D Schematic of coils configuration and magnetic structure on which a sample with a colloid is placed and transported b) Image of coils on the stage of the microscope.

and Kassel from [Co/Au] magnetic multilayer structures with perpendicular magnetic anisotropy. Patterning was done by using a desired shadow mask and He-ion bombardment through the mask onto the structure. All patterns were made to have a lattice constant of  $7\mu\text{m}$ . As a result of the small thickness of the magnetic structures relative to their wavelength, all fabricated structures had a pattern field  $H^p = M_s \cdot t \cdot Q$ , which was characterized to be  $3\text{ kA/m}$ . Details of the fabrication process of the lithographic structures is in Pub [P3], Appendix IX. To maintain the colloidal particles at a universal height above the surface of the magnetic patterns during experiments, the surfaces of the patterns were spin coated with polyelectrolyte (Fotoresit Positiv AZ 1512 HS Microchem Newton MA) of thickness  $1.6\mu\text{m}$ .

## External Magnetic fields

The external magnetic fields in the experiments of the microscopic transport of colloids was generated from a set of coils similar to the previous set up. However, here inhomogeneous fields have drastic effects on the trajectory of the particles. As a result, two coils each  $x$ - and  $y$ - directions were used to reduce this effect as shown in figure A.2 a). The coils were connected to a  $40\text{ MHz}$  Aim-TTi TGA 1244 waveform generator, Tektronix TDS 2014B oscilloscope and three Kepco BOP 20-50GL bipolar amplifiers. Modulation loops of the desired form are created with a Matlab program and uploaded to the signal wave generator. In this arrangement, the exact modulation of the potential is obtained above the magnetic patterns through the coils.

## Sample

The sample for the topologically protected transport of colloids were prepared from paramagnetic and diamagnetic particles at various concentrations and stages of the investigations. On one hand,  $2.7\mu\text{m}$  (*Dynabeads M-270*, *ThermoFischer*) paramagnetic particles were immersed in deionized water and placed above the magnetic structures for transport. On the other hand, non-magnetic polystyrene particles (*Fluoro Max Polymer microspheres* - *ThermoFischer*) of  $4\mu\text{m}$  diameter were used as diamagnetic particles. To achieve effective diamagnetism, these particles were immersed in water-based ferrofluid (*Ferrotec EMG 707*). A mixture of the components is prepared in a test tube and  $\sim 5 - 10 \mu\text{l}$  of the sample is pipetted onto the designated structure for observation. For experiments involving the transport of diamagnetic particles, a careful chosen concentration of ferrofluid, deionized water and particles was required. This is important because a high concentration of ferrofluid reduces the visibility of the background structure of the magnetic pattern. Therefore, a balance between the visibility of the patterns and effective diamagnetism of the non-magnetic polystyrene particles is essential.

### A.3 Macroscopic Floquet crystalline pump

Set up for the macroscopic Floquet crystalline pumping of particles was rather simple and easy to manipulate as compared to that for the equilibrium structures of the critical mixture and the microscopic transport of colloidal particles. A steel ball and superconductor being paramagnetic and diamagnetic respectively were transported along the millimeter-sized magnetic lattices. One can view the motion and trajectories of the particles without the use of a camera. However, a simple digital camera offered the possibility to record the dynamics of the transport for analysis using the designed computer Matlab program. The NbB magnets generating the external magnetic field, magnetic structure and sample (particles) are arranged in a *Goniometer* geometry as shown in figure A.3. By reorienting the field direction in the desired modulation loop, the particles move above the magnetic pattern while a *LASER* pointer attached to it traces out the shape of the loop and allow for recording important points in control space on a screen.

### Magnetic Structure

Four fold ( $C_4$ ), proper six fold ( $C_6$ ) and improper six fold ( $S_6$ ) symmetric patterns where built out of millimeter-sized NbB-magnets of various saturated magnetization with lattice constants 2.82 mm, 4.33 mm, and 5.20 mm respectively. The constructed lattices were glued with epoxy onto the holder to avoid its damage by the external field. A transparent PMMA spacer of defined thickness 1 - 1.5mm was placed above the structure to ensure universal elevation. In addition, another transparent plate is used to enclose the paramagnetic (steel ball) particle on to the holder.

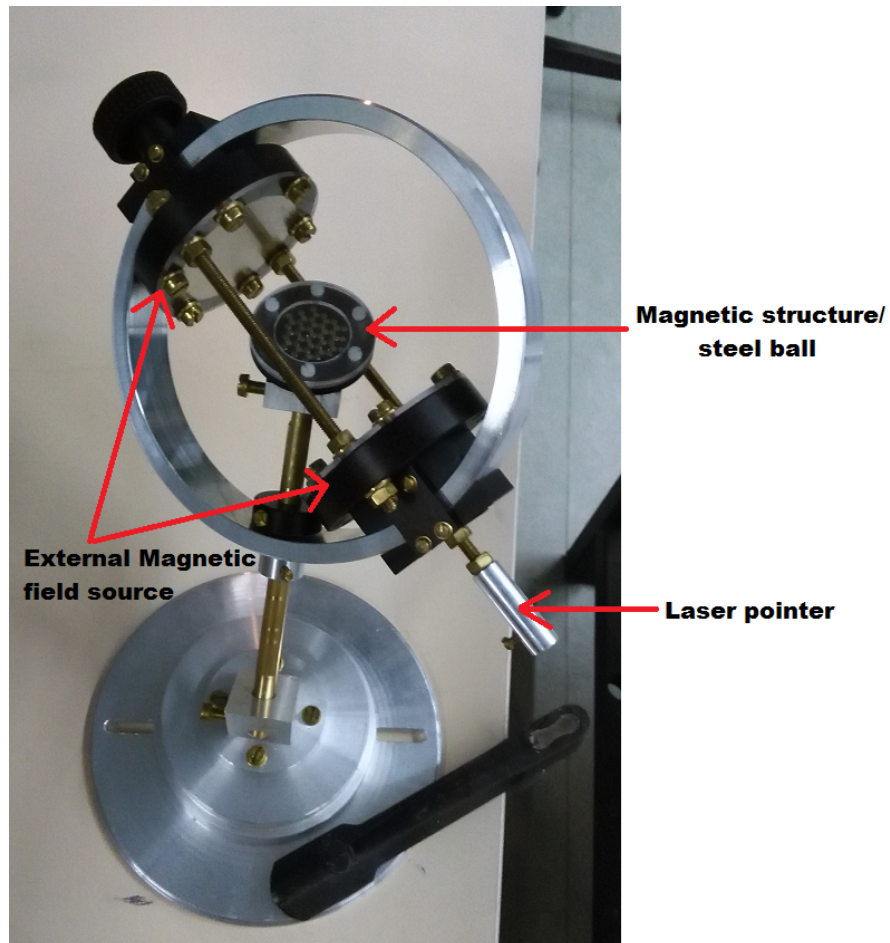


Figure A.3: Experimental set up for steel and superconductor pump. The sample and magnetic structure fixed in between the two large cylindrical NbB magnets generating the desired field. The Laser pointer is attached to one end and traces out the modulation loop on a screen.

## External Magnetic fields

Two large size cylindrical NbB magnets of 60 mm x 10 mm diameter and thickness respectively generated the external field of  $\sim 36$  kA/m. They are arranged parallel to each other at a distance of 120 mm on the Goniometer. Modulation loops of the field are done by physically steering the magnets in the desired loop on control space.

## Sample

A steel sphere of diameter 1 mm was utilized as the paramagnetic particle in this experiment. It is placed above the spacer providing the universal elevation and enclosed by another transparent cover on to the structure. A high  $T_c$  superconductor of equivalent size acts as the diamagnetic particle. The compartment of the magnetic pattern holder is made high enough to fill in *liquid nitrogen*. In this way, immersing the superconductor in the liquid nitrogen will provide effective diamagnetic behavior of the particle.



# Bibliography

- [1] M. Doi, *Soft Matter Physics*. Oxford University press, (2013).
- [2] R. Holyst, “Some features of soft matter systems,” *Soft Matter*, vol. **1**, pp. 329–333, (2005).
- [3] R. M. Erb, J. J. Martin, R. Soheilian, C. Pan and J. R. Barber, “Actuating soft matter with magnetic torque,” *Adv. Funct. Mater.*, vol. **26**, pp. 3859–3880, (2016).
- [4] National Research Council 2013, *High magnetic field science and its application in the United States: current status and future directions*. The National Academies Press, (2013).
- [5] Y. Tsori and U. Steiner, *Polymers, Liquids and Colloids in Electric Fields*, vol. 2 of *Series in Soft Condensed Matter*. World Scientific, (2009).
- [6] J. E. Martin, J. Odinek and T. C. Halsey, “Evolution of structures in a quiescent electrorheological fluid,” *Phy. Rev. Letts.*, vol. **69**, pp. 1524–1527, (1992).
- [7] C. A. Grattoni, R. A. Dawe, C. Y. Saeh and J. D. Gray, “Lower critical solution coexistence curve and physical properties (density, viscosity, surface tension, and interfacial tension) of 2,6-lutidine + water,” *J. Chem. Eng. Data*, vol. **38**, pp. 516–519, (1993).
- [8] S. Z. Mirzaev, R. Behrends, T. Heimburg, J. Haller and U. Kaatze, “Critical behavior of 2,6-dimethylpyridine-water: Measurements of specific heat, dynamic light scattering and shear viscosity,” *J. Chem. Phys.*, vol. **124**, p. 144517, (2006).
- [9] W. T. S. Huck, “Artificial skins: Hierarchical wrinkling,” *Nature materials*, vol. **4**, pp. 271–272, (2005).
- [10] K. Efimenko, M. Rackaitis, E. Manias, A. Vaziri, L. Mahadevan and J. Genzer, “Nested self-similar wrinkling patterns in skins,” *Nature materials*, vol. **4**, pp. 293–297, (2005).
- [11] F. Elias, C. Flament, J. C. Bacri and S. Neveu, “Macro-organized patterns in ferrofluid layer,” *J. Phys. I France*, vol. **7**, pp. 711–728, (1997).

- [12] R. M. Grechishkin, M. Yu. Goosev, S. E. Ilyashenko and N. S. Neustroev, “High-resolution sensitive magneto-optic ferrite-garnet films with planar anisotropy,” *J. of Mag. and Mag. Mat.*, vol. **157/158**, pp. 305–306, (1996).
- [13] F. W. Aldbea and N. B. Ibrahim, “An overview about garnet thin films (terbium yttrium iron garnet and aluminum terbium yttrium iron garnet ) structural and magnetic properties,” *J. of Mat. Sci. and Application*, vol. **1(5)**, pp. 185–194, (2015).
- [14] P. Tierno, T. H. Johansen and T. M. Fischer, “Localized and delocalized motion of colloidal particles on a magnetic bubble lattice,” *PRL*, vol. **99**, p. 038303(4), (2007).
- [15] P. Tierno, F. Sagues, T. H. Johansen and T. M. Fischer, “Colloidal transport on magnetic garnet films,” *Phys. Chem. Chem. Phys.*, vol. **11**, pp. 9615–9625, (2009).
- [16] A. Deutsch, G. Theraulaz and T. Vicsek, “Collective motion in biological systems,” *Interface Focus*, vol. **2**, pp. 689–692, (2012).
- [17] T. Sanchez, D. T. N. Chen, S. J. DeCamp, M. Heymann and Z. Dogic, “Spontaneous motion in hierarchically assembled active matter,” *NATURE*, vol. **491**, pp. 431–434, (2012).
- [18] A. Bricard, J. B. Caussin, N. Desreumaux, O. Dauchot and D. Bartolo, “Emergence of macroscopic directed motion in populations of motile colloids,” *NATURE*, vol. **503**, pp. 95–98, (2013).
- [19] J. Loehr, M. Loenne, A. Ernst, D. de las Heras and T. M. Thomas, “Topological protection of multiparticle dissipative transport,” *Nature Comm.*, vol. **7**, p. 11745, (2016).
- [20] D. de las Heras, J. Loehr, M. Loenne and T. M. Fischer, “Topologically protected colloidal transport above a square magnetic lattice,” *New. J. Phys.*, vol. **18**, p. 105009, (2016).
- [21] M. He, N. Xin, Y. Liu and Y. Zhang, “Determination of critical properties of binary and ternary mixtures of short chain alcohols and alkanes using flow apparatus,” *J. of Supercritical Fluids*, vol. **104**, pp. 19–28, (2015).
- [22] P. Papon, J. Leblond and P. H. E. Meijer, *The Phase of Phase Transitions*. Springer, 2 ed., (2006).
- [23] A. Y. Zubarev and L. Y. Iskakova, “Yield stress in thin layers of ferrofluids,” *Physica A*, vol. **365**, pp. 265–281, (2006).
- [24] K. Lichtner, A. J. Archer and S. H. L. Klapp, “Phase separation dynamics in a two-dimensional magnetic mixture,” *J. Chem. Phys.*, vol. **136**, p. 024502, (2012).

- 
- [25] S. T. Cattes, S. H. L Klapp and M. Schoen, “Condensatioin, demixing and orientational ordering of magnetic colloidal suspensions,” *Phys. Rev. E*, vol. **91**, p. 052127, (2015).
- [26] D. C. Johnston, *Advances in thermodynamics of the van der Waals fluid*. Morgan and Claypool Publishers, (2014).
- [27] A. Parola and L. Reatto, “Depletion interaction between spheres of unequal size and demixing in binary mixtures of colloids,” *Molecular Physics*, vol. **113**, pp. 2571–2582, (2015).
- [28] A. Fernandez-Nieves and A. M. Puertas, *Fluids, Colloids adn Soft Materials*. WILEY, (2016).
- [29] A. J. Dickstein, S. Erramilli, R. E. Goldstein, D. V. Jackson and S. A. Langer, “Labyrinthine pattern formation in magnetic fluids,” *Science*, vol. **216**, pp. 1012–1015, (1993).
- [30] A. G. Papathanasiou and A. G. Boudouvis, “Three-lobe-shaped equilibrium states in magnetic liquid bridges,” *Phys. Rev. E*, vol. **65**, p. 035302, (2002).
- [31] J. Yin and M. C. Boyce, “Unique wrinkles as identity tags,” *Nature*, vol. **520**, pp. 164–165, (2015).
- [32] The Royal Swedish Academy of Science, “Topological phase transition and topological phases of matter,” (2016).
- [33] S. Stahl, *Introduction to topology and geometry*. WILEY, (2005).
- [34] C. Nash and S. Sen, *Topology and geometry for Physicist*. Academic Press, (1983).
- [35] E. H. Hall, “On a new action of the magnet on electri currents,” *American Journal of Mathematics*, vol. **2**, pp. 287–292, (1879).
- [36] M. O. Goerbig, “Qunatum hall effects,” *arXiv:0909.1998v2 [cond-mat.mes-hall]*, (2009).
- [37] Shubnikov L. W. and de Haas W. J., “Die abhängkeit des elektrischen widerstandes von wismutkristallen von der reinheit des metalles,” in *Proc. Roy. Acad. Amsterdam*, vol. **33**, pp. 350–362, (1930).
- [38] K. v. Klitzing, G. Dorda and M. Pepper, “New method for high-accuracy determination of the fine-structure constant based on quantized hall resistance,” *Phys. Rev. Lett.*, vol. **45**, pp. 494–497, (1980).
- [39] D. J. Thouless, M. Kohmoto, M. P. Nightingale and M. den Nijs, “Quantized hall conductance in two dimensional periodic potential,” *Phys. Rev. Lett.*, vol. **49**, pp. 405–408, (1982).

- [40] M. Z. Hasan and C. L. Kane , “Colloquium: Topological insulators,” *Review of Modern Physics.*, vol. **82**, pp. 3045–3067, (2010).
- [41] A. H. MacDonald, “Introduction to the physics of quantum hall regime,” *arXiv:cond-mat/9410047v1*, (1994).
- [42] M. Kohmoto, “Topological invariant and the quantization of the hall conductance,” *Annals of Physics*, vol. **160**, pp. 343–354, (1985).
- [43] 48th IFF Spring School 2017, *Topological Matter - Topological Insulators, Skyrmions and Majoranas*. Jülich Forschungszentrum, (2017).
- [44] A. Bansil, H. Lin and T. Das, “Topological band theory,” *Review of Modern Physics*, vol. **88**, p. 021004(37), (2016).
- [45] N. Casic, *Dynamic Self-assembly of Magnetic Colloidal Particles*. Dissertation, University of Bayreuth, (2013).

# Publications

---



## **P1 Magnetic field induced modulated phases in ferrofluid lutidine silicone oil mixture**

**Jonas Bugase<sup>a</sup>, Johannes Berner<sup>b</sup>, Thomas M. Fischer<sup>\*a</sup>**

<sup>a</sup>Institute of Physics Universität Bayreuth, 95440 Bayreuth, Germany

<sup>b</sup>Physikalisches Institut, Universität Stuttgart, Pfaffenwaldring 57, 70569 Stuttgart, Germany

*Soft Matter*, 2016,**12**, pp(8521-8527)

**DIO:10.1039/C6SM01713D**

Received 26<sup>th</sup> July, 2016, Accepted 14<sup>th</sup> Sept., 2016

---

### **My Contribution**

The experiments were designed and performed by me. I also analyzed the results and wrote the manuscript with T. M. Fischer. J. Berner identified the critical demixing magnetic field sensitive ferrofluid mixture.




 Cite this: *Soft Matter*, 2016,  
12, 8521

## Magnetic field induced modulated phases in a ferrofluid lutidine silicone oil mixture†

 Jonas Bugase,<sup>a</sup> Johannes Berner<sup>b</sup> and Thomas M. Fischer\*<sup>a</sup>

A mixture of an ester based ferrofluid with silicone oil and 2,6-lutidine is exposed to an external magnetic field. We find a region of composition of the ternary mixture, where weak magnetic fields of the order of a few  $\text{kA m}^{-1}$  induce a modulated phase with a pattern characterized by equilibrium size droplets of the minority phase immersed into the extended majority phase. While the pattern resembles in many ways the pattern of immiscible magnetic fluids, the dependence of the characteristic parameters of the pattern on the magnetic field are completely different than in immiscible fluids. We theoretically explain the pattern formation as a magnetic field induced polymerization of magnetic particles into magnetic chains that goes along with a reduction of the entropy of mixing. This entropy reduction causes the Ostwald ripening of chains into mesoscopic droplets the size of which is limited by repulsive dipolar interactions between the chains.

 Received 26th July 2016,  
Accepted 14th September 2016

DOI: 10.1039/c6sm01713d

[www.rsc.org/softmatter](http://www.rsc.org/softmatter)

### 1 Introduction

The properties of magnetic fluids makes them useful for many technological, biological and medical purposes, as well as materials science and engineering research.<sup>1</sup> Magnetic fluids consist of usually superparamagnetic nanoparticles stabilized and immersed into a complex carrier fluid. Exchange interactions in the superparamagnetic particles that have sizes below the magnetic correlation length cause their superparamagnetic behavior. Dipolar interactions relevant for the formation of magnetic domains in larger magnetic particles cannot cause domain formation in the nanoregime. Inter particle dipolar interactions between the individual particles, however, become relevant if one exposes the liquid to an external magnetic field and many of the properties of such ferrofluids are due to these dipolar interactions.

The dipole-dipole interaction is a traceless anisotropic interaction that when averaged over all directions vanishes identically. Moreover the interaction is usually weak and can only affect the behavior of a liquid due to its superextensive nature. This causes interfacial dipolar energies of domain walls to grow faster than the area of the interface surrounding the domain as one increases the size of a domain. For this reason the dipolar interaction dominates for anisotropic arrangements of mesoscopic length and causes a patterning on such mesoscopic scale.

The miscibility of fluids comprising a complex fluid is a second independent feature that can cause complex patterns when such a fluid approaches a critical demixing point.<sup>2,3</sup> Spinodal decomposition is a known process that describes the dynamics of demixing fluids. Here we pose the interesting question how the behavior of a complex fluid changes if we combine the magnetic properties of a ferrofluid with critical miscibility properties of a mixed fluid.

There are various classes of fluids whose structural and thermodynamical properties are strongly influenced by the presence of either magnetic or electric dipolar interaction between constituents. To this end, a complete understanding of the structure, phase behavior, and dynamics of strongly interacting dipolar magnetic fluids is still a considerable challenge to soft matter physics.<sup>4,5</sup> Generally, our knowledge and understanding of phase separation in mixtures is important to tune the interfacial and confinement properties especially when they involve internal degrees of freedom and resulting in their sensitivity to an external field.<sup>6</sup> Essentially, mixtures of magnetic and non-magnetic particles offer promising application in micron and submicron pattern formation since the system can be manipulated by external magnetic fields.<sup>7</sup>

In this work we combine the magneto-mechanic properties of a ferrofluid with the thermo-chemical properties of a critical miscible mixture. Demixed phases near a critical demixing point have orders of magnitude lower interfacial tension than between immiscible liquids. Shape deformations of the critical interface between demixing phases are therefore possible on scales that are orders of magnitude smaller than for immiscible fluids. We use this sensitivity toward magnetic fields for the critical mixture of an ester based ferrofluid, with silicone and 2,6-lutidine.

<sup>a</sup> Institute of Physics Universität Bayreuth, 95440 Bayreuth, Germany.

 E-mail: [Thomas.Fischer@uni-bayreuth.de](mailto:Thomas.Fischer@uni-bayreuth.de)
<sup>b</sup> Physikalisches Institut, Universität Stuttgart, Pfaffenwaldring 57, 70569 Stuttgart, Germany

† Electronic supplementary information (ESI) available. See DOI: 10.1039/c6sm01713d

Above a critical magnitude of the field  $H_c$ , the initially homogeneous mixture shows an equilibrium phase separation with the formation of droplets rich in the magnetic phase that are immersed in a non-magnetic phase. Dipolar interactions limit the phase separation of both phases to the modulation length of a modulated phase.

The composition and experimental observations of our mixture presents a rich and exciting phase separation properties at room temperature in the presence of applied weak fields ( $< 10 \text{ kA m}^{-1}$ ). Our system reacts to three control parameters: the component concentration, the magnetic field strength and the temperature. Here we report the behavior as a function of composition and magnetic field at a fixed temperature and develop a simple model to describe the pattern forming effects.

### 1.1 Experiment

The ester based ferrofluid APG 512 A from Ferrotec was used in this study. This ferrofluid consists of magnetite nanoparticles of mean diameter 7.2 nm with a particle volume concentration of 6.1% immersed into synthetic esters and stabilized by surfactants adsorbed to the particles.<sup>8</sup> 2,6-Dimethylpyridine 98% was purchased from Sigma-Aldrich and Silicone DC 200 ( $\sim 10 \text{ mPa s}$ ) was purchased from Fluka. The three liquids were mixed and a droplet 5  $\mu\text{l}$  of the mixture was placed on top of glass and PMMA slides. The droplet partially wets the slide and exposes a free liquid air interface at the top of the sample. Observations of the texture of the sample were performed in the presence of an external static magnetic field under controlled temperatures between 12  $^{\circ}\text{C}$  and 35  $^{\circ}\text{C}$ . The external field was applied perpendicular to the plane of the sample as shown in Fig. 1. The resulting phase separation above the external critical field  $H_c$  is observed using transmission optical microscopy using a Leica DMLP microscope. Here, the 2D mesoscopic droplets (magnetic rich phase) are cylindrical-like structures that extend from the glass surface to the air-liquid interface of the sample.

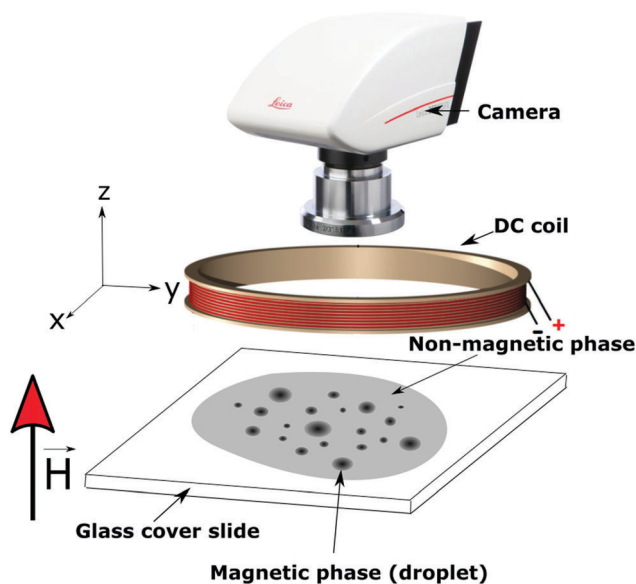


Fig. 1 Schematic representation of the experimental set-up.

## 2 Results

Our ternary mixture develops a modulated phase as a function of the external field and microscopic images of the subcritical homogeneous mixture and the modulated phase of the mixture are recorded below and above the critical field  $H_c$  are shown in Fig. 2. These measurements were done at a temperature  $T \approx 20 \text{ }^{\circ}\text{C}$  and an external field  $H = 7.5 \text{ kA m}^{-1}$ . Fig. 2a shows the texture of the liquid below the critical field  $H < H_c$  at a composition defined by the volume fraction ratio  $\phi_{\text{ferro}} : \phi_{\text{lutidine}} : \phi_{\text{silicone}} = 40 : 10 : 50$ . The texture of the liquid shows fluctuations of the transmission on a submicron scale. Presumably the mixture has a complex submicron structure like a micro-emulsion or similar. On the longer length scale above the micron scale there is however no visible texture of the fluid and we will therefore use the term homogeneous phase for textures of the type presented in Fig. 2a. The homogeneous phase thus differs from the texture of two phase separated immiscible liquids, where one observes the coexistence of two macroscopic droplets of each of the immiscible components. Fig. 2b–d shows patterns of the miscible fluid at a field beyond the critical field  $H > H_c$ . However,  $H_c$  varies for the different composition of b, c, and d. A composition of  $\phi_{\text{ferro}} : \phi_{\text{lutidine}} : \phi_{\text{silicone}} = 40 : 10 : 50$  is presented in Fig. 2b where a collection of black droplets forms in a surrounding liquid having a higher transmission than the homogeneous fluid. The droplets have diameters of the order ten micron and are separated from each other by a distance of similar magnitude. We also observe a pattern having a texture that is the inverted pattern of Fig. 2b. Fig. 2c shows a pattern at a composition of  $\phi_{\text{ferro}} : \phi_{\text{lutidine}} : \phi_{\text{silicone}} = 70 : 0 : 30$  with silicone rich droplets immersed into a ferrofluid rich phase. Finally in Fig. 2d we show a labyrinth pattern of silicone rich and ferrofluid rich lamellae for  $\phi_{\text{ferro}} : \phi_{\text{lutidine}} : \phi_{\text{silicone}} = 50 : 0 : 50$ .

In Fig. 2e we present a ternary phase diagram that shows which patterns are observed at which composition. The texture of the pattern varies with the concentration of its three components: there are compositions for which the mixture remains in the homogeneous phase at all temperatures and magnetic fields. Equal volume concentrations of all three components tend to result in ferrofluid rich droplet patterns. Inverted droplets occur in binary mixtures of a ferrofluid majority mixed with a silicone minority. When both components are mixed in equal proportions the texture crosses over to the inverted droplet phase *via* the labyrinth phase along the ferrofluid-silicone binary line.

In a mixture of immiscible fluids the modulated phase usually disappears *via* the coarsening and coalescence of droplets if one turns off the magnetic field. Here the modulated phase disappears and returns to the homogeneous phase of Fig. 2a *via* the dissolution of ferrofluid droplets in the extended phase. The dissolution of droplets is shown in Fig. 3a–d. Fig. 3a shows the pattern at a composition  $\phi_{\text{ferro}} : \phi_{\text{lutidine}} : \phi_{\text{silicone}} = 40 : 40 : 20$  at a field of  $H = 5 \text{ kA m}^{-1}$  at a time  $t = -3 \text{ s}$ . At ( $t = 0$ ) we switch off the field and Fig. 3b–d show the temporal evolution of the pattern following the switch. The boundary of ferrofluid rich droplets turns into a front that radially expands and thereby dilutes the

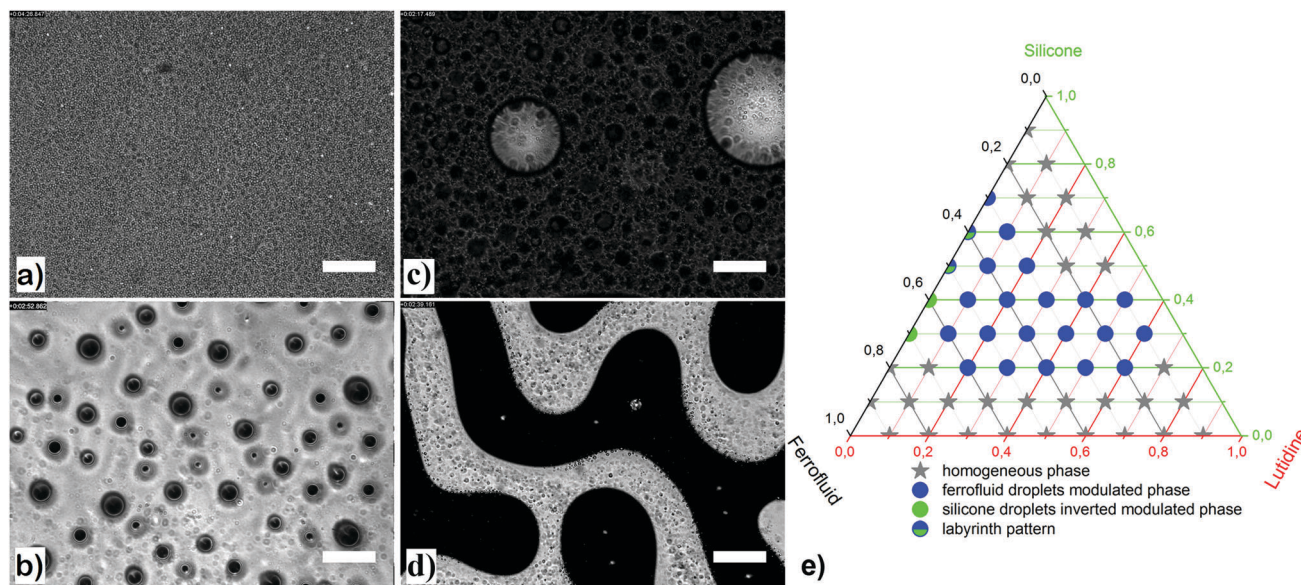


Fig. 2 Behavior of the mixture at  $T = 20\text{ }^{\circ}\text{C}$  in (a) the absence of an applied field, and (c) and (d) in the presence of an applied field  $H = 7.5\text{ kA m}^{-1}$ . (a) Homogeneous mixture of sample at a field of  $H < H_c$ . (b) Phase separation of a mixture of composition  $\phi_{\text{ferro}} : \phi_{\text{lutidine}} : \phi_{\text{silicone}} = 40 : 10 : 50$  at a field of  $H > H_c = 3.8\text{ kA m}^{-1}$ . Black droplets enriched in ferrofluid nucleate in the extended phase that has reduced ferrofluid concentration. (c) Inverted phase of silicone rich droplets immersed into a ferrofluid rich extended phase  $H > H_c = 6.0\text{ kA m}^{-1}$  with composition  $\phi_{\text{ferro}} : \phi_{\text{lutidine}} : \phi_{\text{silicone}} = 70 : 0 : 30$ . (d) Labyrinth pattern at  $H > H_c = 4.0\text{ kA m}^{-1}$  and composition of  $\phi_{\text{ferro}} : \phi_{\text{lutidine}} : \phi_{\text{silicone}} = 50 : 0 : 50$ . (e) A ternary phase diagram of the mixture. The common scale bar of all four images is  $50\text{ }\mu\text{m}$ . A video clip of the transition from (a) and (b) is shown in the ESI<sup>†</sup> Movie.

ferrofluid rich phase. Eventually fronts from different formerly ferrofluid rich regions collide and stop leaving behind a homogeneous phase that is interrupted by the remainders of collided fronts that eventually dissolve on longer time scales. This shows that the magnetic field is not only responsible for the lateral distribution of both phases but also for the demixing into both components. A theory explaining the phenomenon must not only explain the pattern but also the appearance of the two phases.

The critical magnetic field  $H_c$  which varies with composition is given in the contour plot in Fig. 4. The lowest critical field occurs for a composition of  $\phi_{\text{silicone}} = 25\%$  silicone and roughly equal volume fractions ( $\phi_{\text{ferro}} = \phi_{\text{lutidine}} = 37\%$ ) of ferrofluid and lutidine. The transition at low silicone concentrations to the homogeneous phase is of first order with a discontinuous jump of the critical field from lowest to very high values. At the other borders to the homogeneous phase the critical field rises continuously as one approaches the modulated phase border.

When we increase the magnetic field beyond the critical field, the equilibration of the ferrofluid droplet size is very slow and nucleation of droplets does not stop with this field increase. Droplets nucleating at fields above the critical field are smaller than those that have already nucleated at the critical field. The equilibration of the droplet size occurs *via* the coalescence of droplets. We observe a decrease in the number of domains (droplets) and an increase in the average droplet size with increasing magnetic field. This is contrary to what one would expect from an increase of the strength of the lateral dipolar interactions between the droplets<sup>9</sup> and points to a complicated dependence of the interfacial tension between

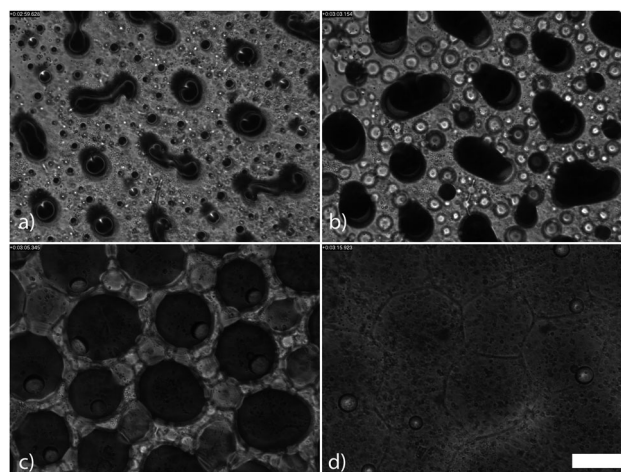


Fig. 3 Dissolution of the modulated phase at a composition of  $\phi_{\text{ferro}} : \phi_{\text{lutidine}} : \phi_{\text{silicone}} = 40 : 40 : 20$  when the magnetic field  $H = 5\text{ kA m}^{-1} > H_c$  is switched off at  $t = 0\text{ s}$ . (a) The pattern at  $t = -3\text{ s}$ , (b) the pattern when the field is just switched off  $t = 0$  (c) the pattern after  $t = 2\text{ s}$ , and (d) the pattern after  $t = 12\text{ s}$ .  $T \approx 20\text{ }^{\circ}\text{C}$  and the scale bar corresponds to  $100\text{ }\mu\text{m}$ . A video clip of the dissolution is shown in the ESI<sup>†</sup> Movie.

droplet and extended phase on the magnetic field dependent composition of the droplets and the extended phase.

In a non-magnetic regular mixture there is no stable droplet size and the coalescence of two mesoscopic droplets or the coalescence of droplets and individual magnetic chains (Ostwald ripening)<sup>10</sup> will only stop when only one droplet of the two coexisting compositions remains. Here we clearly observe an equilibrium size of the droplets. In Fig. 5 we plot this

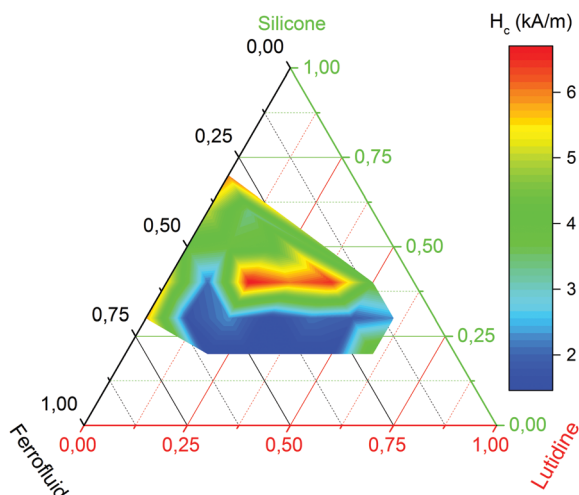


Fig. 4 Contour plot of the critical magnetic field  $H_c$  as a function of the composition of the mixture at a temperature of  $T \approx 20$  °C.

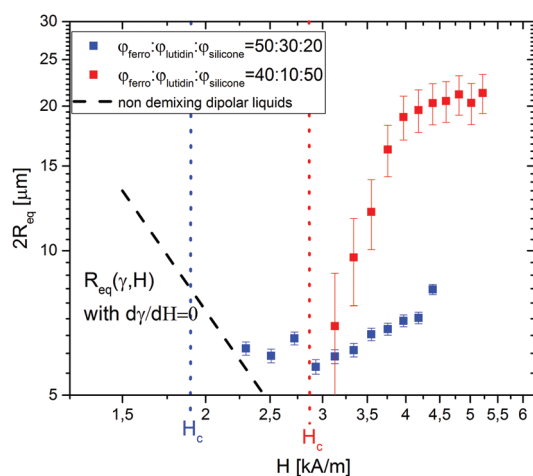


Fig. 5 The lateral equilibrium diameter of the average droplet as a function of the magnetic field for two different compositions of the mixture. The dotted line is the prediction when using a magnetic field independent interfacial tension  $\gamma$  and correlation length  $\xi$ .

equilibrium droplet size as the function of the magnetic field for the compositions  $\phi_{\text{ferro}}:\phi_{\text{lutidine}}:\phi_{\text{silicone}} = 50:30:20$  (blue) and the composition  $\phi_{\text{ferro}}:\phi_{\text{lutidine}}:\phi_{\text{silicone}} = 40:10:50$  (red). There is no clear functional relationship between the size and the magnetic field from our measurements. The dependence of the droplet diameter on the magnetic field differs from the prediction for immiscible fluids. At the first composition (blue) the size first slightly decreases with the magnetic field passes through a minimum and then increases with the field. At the second composition (red) we observe a monotonous increase of the droplet size with the magnetic field.

If we increase the magnetic field at a sufficiently high rate ( $dH/dt = 33 \text{ A ms}^{-1}$ ) and far above  $H_c$ , we can destabilize the droplet phase and deform a laterally circular droplet into a dogbone shape.<sup>11–14</sup> Fig. 6 shows such a droplet shape destabilization for a droplet in a mixture of the second composition (red).

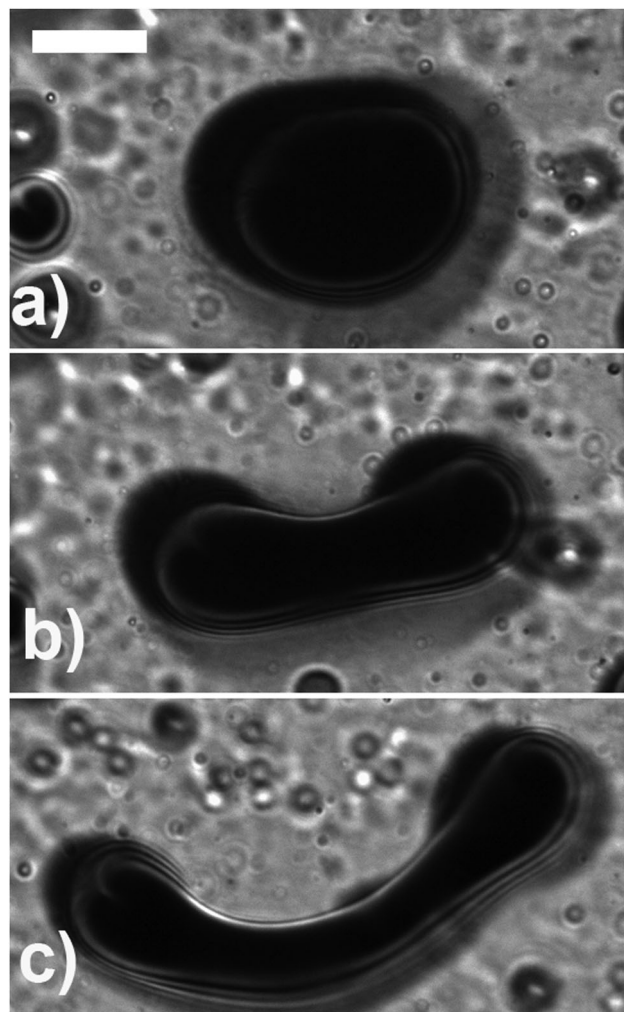


Fig. 6 Shape transition of a laterally circular droplet into a lateral dogbone shape. The composition of the mixture is  $\phi_{\text{ferro}}:\phi_{\text{lutidine}}:\phi_{\text{silicone}} = 40:10:50$  (red in Fig. 5) and  $H_c = 2.9 \text{ kA m}^{-1}$ . The field is increased from (a)  $H = 5.2 \text{ kA m}^{-1}$  to (b)  $H = 5.8 \text{ kA m}^{-1}$  to (c)  $H = 6.9 \text{ kA m}^{-1}$  at a rate of  $dH/dt = 33 \text{ A ms}^{-1}$ . The scale bar is  $50 \mu\text{m}$ . A video clip of the shape transition is provided with the ESI,† Movie.

### 3 Phenomenological model

In our simplified model we reduce the ternary mixture to an effective binary magnetic (ferrofluid) and non-magnetic (silicone and 2,6-lutidine) fluid mixture. Crucial to the description of this system is capturing of both the microscopic and mesoscopic structural behavior of the mixture since the rich phenomena can not be explained entirely by magnetic dipolar interactions. Starting from a Stock Mayer fluid mixture model to describe the microscopic structural formation we end up with a phenomenological model of a dipolarly interacting fluid of magnetic field induced polymer-chains that precipitate in the bad solvent of the non-magnetic fluid and there form a modulated phase<sup>15,16</sup> due to long range repulsive dipolar interactions.

The phase behavior of mixed Stock Mayer fluids have been studied intensely on a microscopic level using density functional theory.<sup>17–19</sup> In such models, a mixture of different types

(labeled by  $\alpha = 1, 2, \dots$ ) of particles interact *via* isotropic Lennard Jones pair potentials:

$$U_{\alpha,\beta}^{\text{LJ}} = 4\epsilon_{\alpha,\beta} \left[ \left( \frac{\sigma_{\alpha} + \sigma_{\beta}}{r_{ij}} \right)^{12} - \left( \frac{\sigma_{\alpha} + \sigma_{\beta}}{r_{ij}} \right)^6 \right] \quad (1)$$

where  $\epsilon_{\alpha,\beta}$  denotes the interaction energy parameter between the particles of type  $\alpha$  and  $\beta$ , and  $\sigma_{\alpha}$  is the hard core radius of the particle of type  $\alpha$ .  $r_{ij} = |\mathbf{r}_i - \mathbf{r}_j|$  denotes the distance between the pair of particles. The mixed fluid turns into a Stock Mayer fluid if the particles are magnetic and apart from their Lennard Jones type interactions also interact *via* magnetic dipole interactions:

$$U_{\alpha,\beta}^{\text{dd}} = \frac{\mu_0}{4\pi} \mathbf{m}_i^{\alpha} \cdot \frac{r_{ij}^2 \mathbf{I} - 3\mathbf{r}_{ij}\mathbf{r}_{ij}}{r_{ij}^5} \cdot \mathbf{m}_j^{\beta} \quad (2)$$

where the time averaged magnetic moments (time averaged over a time larger than the Neel time) of the superparamagnetic particles are similar to induced paramagnetic moments

$$\mathbf{m}^{\alpha} = \chi_{\text{eff}}^{\alpha} \frac{4\pi\sigma_{\alpha}^3}{3} \mathbf{H} \quad (3)$$

and  $\chi_{\text{eff}}^{\alpha}$  is the effective magnetic susceptibility of the particle and  $\mathbf{H}$  an external magnetic field. What we are interested in here is the particular case of a binary mixture of paramagnetic particles with non magnetic particles:

$$\chi_{\text{eff}}^1 \neq 0 \quad (4)$$

$$\chi_{\text{eff}}^2 = 0 \quad (5)$$

in a situation for which the Lennard Jones attraction between different types of particles is weaker than for similar types of particles but not so weak as to enable a demixing of the components in the absence of dipolar interactions:

$$\epsilon_{1,2} < \epsilon_{1,1}, \epsilon_{2,2} \quad (6)$$

It is well known that a binary Lennard Jones system with volume fraction of particles of type 1 of  $\phi$  can be described thermodynamically by a Gibbs free energy of a regular mixture:

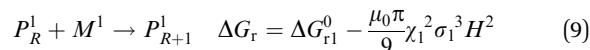
$$G/N = \phi\mu_1^0 + (1 - \phi)\mu_2^0 + h_{\text{mix}}\phi(1 - \phi) + Ts_{\text{mix}} \quad (7)$$

with  $\mu_{\alpha}^0$  the chemical potential of the pure particle fluid of type  $\alpha$ ,  $h_{\text{mix}} = (\epsilon_{1,1} + \epsilon_{2,2})/2 - \epsilon_{1,2}$  the enthalpy of mixture per particle and  $s_{\text{mix}}$  the entropy of mixture per particle. The enthalpy of mixture per particle is positive for the situation described by eqn (6), but below the critical enthalpy of demixing per particle:

$$0 < h_{\text{mix}} < h_{\text{mix}}^c = 2k_{\text{B}}T. \quad (8)$$

It is also well known that an external magnetic field promotes the formation of oriented magnetic particle chains *via* the dipolar interactions. In the simplest model we can catch the effect of the magnetic field *via* a polymerization reaction of the individual

particles (monomers  $M^1$ ) into a magnetic particle polymers  $P_R^1$  of degree of polymerization  $R$ :



The Gibbs free energy of reaction  $\Delta G_r$  consists of a part deriving from the Lennard Jones interaction  $\Delta G_r^0$  and the magnetic dipolar binding energy  $-\frac{\mu_0\pi}{9}\chi_1^2\sigma_1^3H^2$ . This polymerization reaction will set in if the Gibbs free energy of polymerization is negative, which will happen at a critical field

$$H_c = \sqrt{\frac{9\Delta G_{r1}^0}{\mu_0\pi\chi_1^2\sigma_1^3}} \quad (10)$$

There is no limit to the degree of polymerization until a chain has formed that starts and ends at the boundaries of the sample. These boundaries are perpendicular to the magnetic field and separated by the mesoscopic distance  $d$ . The degree of polymerization is thus:

$$R = \begin{cases} 1 & \text{if } H < H_c \\ d/\sigma_1 & \text{if } H > H_c \end{cases} \quad (11)$$

The quasi particles to be considered in the regular mixture Gibbs free energy of eqn (7) are no longer individual particles but are now the polymers and behave analog to a Flory-Huggins regular mixture of a polymer with a solvent. The polymerization reaction renormalizes the entropy of mixture such that

$$s_{\text{mix}} = k_{\text{B}} \left( \frac{\phi}{R} \ln \phi + (1 - \phi) \ln(1 - \phi) \right) \quad (12)$$

the polymer part in the entropy of mixture is reduced by the degree of polymerization. The polymerization reaction thus reduces the entropy of mixture and therefore the critical point shifts from  $\phi_c(H < H_c) = 1/2$  toward  $\phi_c(H > H_c) \approx R^{-1/2}$  such that also the critical enthalpy of demixing per particle

$$h_{\text{mix}}^c(H > H_c) \approx \frac{1}{2}k_{\text{B}}T \quad (13)$$

shifts. If

$$\frac{1}{2}k_{\text{B}}T < h_{\text{mix}} < 2k_{\text{B}}T \quad (14)$$

then the polymers demix from the non-magnetic particles while the magnetic monomers don't. Note that in the lateral direction the dipolar interactions are repulsive and do not promote the aggregation of polymers into mesoscopic polymer droplets. The demixing is an entropic not an energetic effect. The lateral dipolar repulsion, however, renders the interfacial tension between the demixing components super extensive<sup>15,16</sup> and suppresses a complete demixing in favor of a modulated phase of finite size prolate polymer droplets, in close analogy of other dipolar systems such as thin magnetic films or Langmuir monolayers carrying electric dipole moments.

The equilibrium size of the droplets in these systems is described by a balance between dipolar repulsion and interfacial

tension arising due to the local excess Gibbs free energy density in the interfacial region<sup>21–23</sup>

$$R_{\text{eq}} = \xi \exp(2\gamma/(\mu_0 \xi M^2)) \quad (15)$$

Here  $\gamma$  denotes the interfacial tension between the demixing phases and  $M = \phi \chi_1^{\text{eff}} H 3\sigma_1^3/4\pi$  is the magnetization of the ferrofluid rich phase and  $\xi$  is the correlation length that determines the width of the interface.<sup>23</sup> In ordinary magnetic fluids only the magnetic energy depends on the magnetic field and the interfacial tension between the two coexisting phases is independent of the field. For such a situation the equilibrium droplet size decreases with the magnetic field energy.

Here the demixing is induced by the external magnetic field and thus also determines the properties of the demixed components and the structure of the interface between both phases. It is thus not surprising if we obtain a magnetic field dependent interfacial tension  $\gamma(H)$ , where the sign of  $d(\gamma/\xi H^2)/dH$  can be positive or negative.

We note that the assumption of mesoscopic polymers is obviously an oversimplified description. Taking into account more detailed structures<sup>24,25</sup> one obtains a more detailed theoretical description with more complex branched structures that depend on more structural parameters not only the degree of polymerization. The reduction of entropy remains valid in these descriptions as well and it is the main reason, why demixing into modulated phases is observed above a critical field.

## 4 Discussion

Previous work on equilibrium properties of ferrocolloids indicated that increased externally applied magnetic field strength favors phase separation due to increased dipole inter-particle interaction.<sup>26</sup> Further theoretical research states that the equilibrated (condensation) phase transition of ferrofluids is proceeded by formation of linear chain like clusters which collapse into globules when the number of particles in the chain exceeds a critical magnitude  $n_c$ . This phase presents a dense cylindrical-like domains in a relatively dilute surrounding ferrofluid when filled in a thin flat gap with the applied field perpendicular to the gap plane. The formation of these structures is reversible and cause strong variation in rheological and other characteristics of the suspension<sup>27–30</sup> as presented by our composition and magnetic field dependent mixture. Demixing in these theoretical studies occurs for magnetic reasons only. There is no critical demixing without a magnetic field and no critical behavior with the control parameter temperature is predicted.

Considerable work has also been done on phase separation of magnetic mixtures and colloidal suspensions. Mendeleev and Ivanov<sup>31</sup> have predicted and computed ferrofluid structural aggregating in chains under the influence of magnetic fields. The zippering of chains in magnetic nanofluids in the presence of a field and the evolution of electrorheological fluid structures have also been reported.<sup>5,32</sup> The above mentioned investigations are limited to microscopic structures and do not include

computations on mesoscopic length scales where dipolar interactions become again relevant.

In our experiments we do not observe a modulated phase in a pure compound as predicted by the above theories. A mixed composition is needed for a ferrofluid enriched droplet to form in a magnetic field. It is not clear, why a zippering effect<sup>5</sup> should be at work only when nonmagnetic molecules that can prevent the magnetic particles from coming into close contact should promote a droplet formation. Our experiments seem to rather support the entropic effects explained in the phenomenological model section.

There is abundant theoretical and computer simulations work on phase separation dynamics in Stock-Mayer fluids.<sup>17–20</sup> A 2D magnetic mixture as well as demixing of magnetic colloidal suspensions in both the presence and absence of a magnetic field where the magnetic particles are modeled to carry a 3D classical Heisenberg spin using classical density functional theory (DFT) has been performed by Klapp *et al.*<sup>6,17</sup> The experimental observation of phase separation of a polymer-solvent-nanoparticle mixture in a magnetic field has been reported.<sup>7</sup> Similar to our results a phase separation is observed that however does not seem to depend on temperature as is the case for critical demixing fluids. Moreover the fields needed to induce a phase separations were of the order of ( $\sim 40$ – $240$  kA m<sup>-1</sup>) roughly one to two orders of magnitude larger than in our experiments reported here.

## 5 Conclusion

We have experimentally investigated a complex mixture of a ferrofluid with other fluids, where demixing of components can be induced by a magnetic field. We have measured the phase behavior as a function of the composition and as a function of the magnetic field. We find a regime in composition, where above a critical field, we observe a modulated phase of coexisting regions of high and low ferrofluid content. With a phenomenological model we prove the importance of entropy reduction upon magneto-polymerization in a magnetic field, to explain the demixing. The texture of the modulated phase resembles those of other quasi two dimensional systems interacting *via* dipolar interactions, however, the field dependence of the geometric parameters of the modulated phase are in stark contrast to mixtures of immiscible dipolar fluids. We attribute this to the twofold role external magnetic fields play in this critical demixing fluids.

## Acknowledgements

We thank R. Richter for the ferrofluid.

## References

- 1 C. Scherer and A. M. Figueiredo Neto, *Braz. J. Phys.*, 2007, **35**(3a), 718–727.
- 2 M. He, N. Xin, Y. Liu and Y. Zhang, *J. Supercrit. Fluids*, 2015, **104**, 19–28.

- 3 C. A. Grattoni, R. A. Dawe, C. Y. Seah and J. D. Gray, *J. Chem. Eng. Data*, 1993, **38**, 516–519.
- 4 I. Szalai and S. Dietrich, *Mol. Phys.*, 2005, **103**(21–23), 2873–2895.
- 5 J. M. Laskar, J. Philip and B. Raj, *Phys. Rev. E: Stat., Nonlinear, Soft Matter Phys.*, 2009, **80**, 041401.
- 6 S. M. Cattes, S. H. L. Klapp and M. Schoen, *Phys. Rev. E: Stat., Nonlinear, Soft Matter Phys.*, 2015, **91**, 052127.
- 7 R. Rungsawang, J. da Silva, C. Wu, E. Sivaniah, A. Ionescu, C. H. W. Barnes and N. J. Darton, *Phys. Rev. Lett.*, 2010, **PRL 104**, 255703.
- 8 R. Saldivar-Guerrero, R. Richter, I. Rehberg, N. Aksel, L. Heymann and O. S. Rodriguez-Fernandez, *J. Chem. Phys.*, 2006, **125**, 084907.
- 9 Y. A. Buyevich and A. Y. Zubarev, *J. Phys. II*, 1993, **3**(11), 1633–1645.
- 10 A. Pototsky, U. Thiele and A. J. Archer, *Phys. Rev. E: Stat., Nonlinear, Soft Matter Phys.*, 2014, **89**, 032144.
- 11 A. Cebers and M. M. Maiorov, *Magneto hydrodynamics*, 1980, **16**, 21–27.
- 12 R. de Koker and H. M. McConnell, *J. Phys. Chem.*, 1993, **97**, 13419–13424.
- 13 K. Y. C. Lee and H. M. McConnell, *J. Phys. Chem.*, 1993, **97**(37), 9532–9539.
- 14 H. A. Stone and H. M. McConnell, *Proc. R. Soc. A*, 1995, **448**(1932), 97–111.
- 15 M. Seul and D. Andelman, *Science*, 1995, **267**, 476–483.
- 16 A. Cebers, *Magneto hydrodynamics*, 2001, **37**, 195–205.
- 17 K. Lichtner, A. J. Archer and S. H. L. Klapp, *J. Chem. Phys.*, 2002, **136**, 024502.
- 18 B. Groh and S. Dietrich, *Phys. Rev. E: Stat. Phys., Plasmas, Fluids, Relat. Interdiscip. Top.*, 1994, **50**, 3814–3833.
- 19 B. Groh and S. Dietrich, Long-ranged orientational order in dipolar fluids, *Phys. Rev. E: Stat. Phys., Plasmas, Fluids, Relat. Interdiscip. Top.*, 1994, **72**, 2422–2425.
- 20 A. B. Yener and S. H. L. Klapp, 2015, [Cond-Mat.Soft], November, arXiv:1510.00196v2, p. 3.
- 21 H. McConnell, *Annu. Rev. Phys. Chem.*, 1991, **42**, 171–195.
- 22 H. Wang, Y. Zhu, C. Boyd, W. Luo, A. Cebers and R. E. Rosensweig, *Phys. Rev. Lett.*, 1994, **72**, 1929.
- 23 P. Heinig, P. Steffen, S. Wurlitzer and T. M. Fischer\*, *Langmuir*, 2001, **17**, 6633–6637.
- 24 A. Cebers, *Magneto hydrodynamics*, 1982, **18**, 137–142.
- 25 E. Blums, A. Cebers, M. M. Maiorov, *Magnetic Fluids*, Walter de Gruyter, Berlin, New York, 1997.
- 26 Y. A. Buyevich and A. O. Ivanov, *Physica A*, 1992, **190**, 276–294.
- 27 A. Y. Zubarev and L. Y. Iskakova, *Physica A*, 2004, **335**, 325–338.
- 28 A. Y. Zubarev and L. Y. Iskakova, *Physica A*, 2006, **367**, 55–68.
- 29 A. Yu. Zubarev and L. Yu. Iskakova, *Physica A*, 2006, **365**, 265–281.
- 30 L. Yu. Iskakova, A. P. Romanchuk and A. Yu. Zubarev, *Physica A*, 2006, **366**, 18–30.
- 31 V. S. Mendelev and A. O. Ivanov, *Phys. Rev. E: Stat., Nonlinear, Soft Matter Phys.*, 2004, **70**, 051502.
- 32 J. E. Martin and J. Odinek, *Phys. Rev. Lett.*, 1992, **69**, 1524–1527.



## P2 Wrinkled labyrinths in critical demixing ferrofluid

Natalia Wilke<sup>ab</sup>, **Jonas Bugase**<sup>b</sup>, Lisa-Marie Treffenstädt<sup>b</sup>,  
Thomas M. Fischer<sup>\*b</sup>

<sup>b</sup>CIQUIBIC-CONICT, Facultad de Ciencias Químicas, Universidad Nacional de  
Córdoba, Argentina

<sup>b</sup>Institute of Physics Universität Bayreuth, 95440 Bayreuth, Germany

*Soft Matter*, 2016,**13**, pp(7307-7311)

**DIO:**10.1039/C7SM01475A

Received 25<sup>th</sup> July, 2017, Accepted 19<sup>th</sup> Sept., 2017

---

### My Contribution

I performed the experiments using silanized glass and plastic cover slides and supervised the experiments analyzing the elongation and relaxation of the wrinkled labyrinth structure which was done by L. M. Treffenstädt. Together with N. Wilke and T. M. Fischer, we prepared the manuscript for publication.





Cite this: *Soft Matter*, 2017, **13**, 7307

Received 25th July 2017,  
 Accepted 19th September 2017

DOI: 10.1039/c7sm01475a

[rsc.li/soft-matter-journal](http://rsc.li/soft-matter-journal)

## Wrinkled labyrinths in critical demixing ferrofluid†

Natalia Wilke,<sup>ab</sup> Jonas Bugase,<sup>b</sup> Lisa-Marie Treffenstädt<sup>b</sup> and Thomas M. Fischer<sup>id</sup>\*<sup>b</sup>

A thin film of a critical ferrofluid mixture undergoes a sequence of transitions in a magnetic field. First the application of a field induces a critical demixing of the fluid into cylindrical droplets of the minority phase immersed in an extended majority phase. At a second critical field the cylindrical shape is destabilized and transforms into a labyrinth pattern. A third wrinkling transition occurs at even higher field if the liquid has a liquid/air interface. The wrinkling is absent if the droplet has a cover-slide on top. We explain the wrinkling by the wetting behavior of the liquid/air interface that shifts the surface region away from a critical demixing point.

Wrinkles are a result of two coupled materials that grow with different rates. The faster growing material must wrinkle since this is the only way to remain coupled with the other material. When we couple two solids with Hookian mechanical properties and the growth stops, elastic stresses in both materials hold the wrinkle in place.<sup>1</sup> The elastic theory of wrinkling has found useful applications in thin layers of graphene,<sup>2</sup> thin polymer films,<sup>3</sup> as well as in human skin.<sup>4</sup>

Fluids in contrast to solids cannot support shear stress and one therefore needs long range interactions active on the geometric scale of the wrinkles to support their shape. Fluids with long range dipolar interactions can form modulated phases<sup>5</sup> that under proper conditions and in very different materials such as ferrofluids,<sup>6–14</sup> dielectric liquids,<sup>15,16</sup> Langmuir monolayers<sup>17–20</sup> or magnetic garnet films<sup>21,22</sup> can form undulated labyrinth patterns. Like wrinkles in solids they can occur either on a single<sup>1</sup> or on a hierarchy of length scales.<sup>23</sup> Here we show the formation of wrinkles of two length scales in a critical<sup>24,25</sup> ferrofluid mixture<sup>26–31</sup> that decomposes into two phases under the application of an external magnetic field. While the transition to a labyrinth pattern at a larger length scales is well known from immiscible ferrofluid mixtures<sup>6–13</sup> a second wrinkling transition at a higher wrinkling transition field is a new phenomenon occurring only in critical demixing ferrofluids.

We performed experiments with a ternary mixture of liquids (ester based ferrofluid/2,6-lutidine/silicone, see ref. 32 for further details) and placed an approximately 40 micron thick droplet of 4  $\mu\text{L}$  on top of a silicon wafer exposing its free surface toward

the air on top. Fig. 1 shows reflection microscopy images of the texture of the liquid/air surface at different applied magnetic field (see also the video clip in ref. 35). At vanishing field (Fig. 1a) the liquid mixture exhibits a single one phase homogeneous region of low reflectivity that shows no texture. At a critical field  $H_{\text{dem}} \cong 0.7$  mT the liquid demixes into a darker minority phase and a brighter majority phase (Fig. 1b).

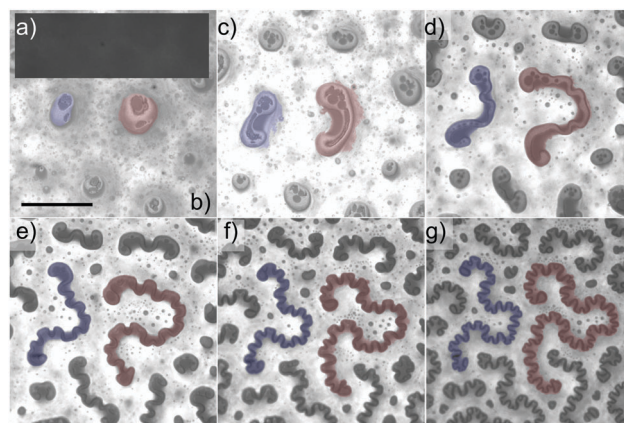


Fig. 1 Reflection microscopy image of the surface of a ferrofluid/2,6-lutidine/silicone (3:1:1) mixture at an external magnetic induction of (a)  $\mu_0 H = 0$  mT, (b)  $\mu_0 H = 2.4$  mT (c)  $\mu_0 H = 3.6$  mT, (d)  $\mu_0 H = 4.8$  mT, (e)  $\mu_0 H = 6.3$  mT, (f)  $\mu_0 H = 7.9$  mT, (g)  $\mu_0 H = 9.3$  mT normal to the film having a silicone oxide support and a free liquid/air surface at the top. (a) Exhibits a homogeneous image with no texture. The demixing of the fluid into ferrofluid rich and ferrofluid poorer phases occurs between (a) and (b). Cylindrical droplets get deformed into a labyrinth of droplets as one increases the field. The onset of the large scale shape transition is between (b) and (c). Between (c) and (d) the labyrinth starts to wrinkle. Wrinkles and large scale bending of the droplets can be distinguished very clearly as the droplets grow (d–g). Scale bar in figure (b) is 100  $\mu\text{m}$ . The two droplets in the center that are marked in blue and red corresponds to the data shown in Fig. 5. A video clip of the sequence of transitions can be viewed in ref. 35.

<sup>a</sup> CIQUIBIC-CONICET, Facultad de Ciencias Químicas, Universidad Nacional de Córdoba, Argentina

<sup>b</sup> Institute of Physics, Universität Bayreuth, 95440 Bayreuth, Germany.  
 E-mail: thomas.fischer@uni-bayreuth.de

† Electronic supplementary information (ESI) available. See DOI: 10.1039/c7sm01475a

The minority phase appears as a collection of drops with circular cross section. In a previous paper<sup>32</sup> we have shown that the three dimensional shape of the droplet is a cylinder that extends from the bottom of the film to the top. These cylinders are immersed in the majority phase. When we surmount a second critical field  $H_{lab} = 2.6$  mT (Fig. 1c) the circular cross section of the minority droplet deforms into a dogbone shape<sup>36</sup> that for larger fields deforms into a labyrinth pattern of droplets (Fig. 1d–g), with each of the droplets following intertwined two dimensional winding paths with a typical radius of curvature of the order of 100  $\mu\text{m}$ . This path significantly grows as a function of the external field as the two ends of the droplet explore regions that are not yet occupied by the minority phase. The increase of the external field is done with an adiabatically slow rate of  $dH/dt = 0.04$  mT  $\text{s}^{-1}$  to prevent branching<sup>14,18–20</sup> of the droplets. This transition from circles to dog-bones and then to labyrinths have been largely described in ferromagnetic fluids<sup>6–14</sup> as well as in other systems.<sup>15–22</sup> At a third field  $H_{wr} \cong 4.5$  mT the path not only grows at the ends but exhibits wrinkles of lower radius of curvature of the order of 20  $\mu\text{m}$ . These wrinkles can be clearly distinguished from the large scale undulation of the droplet in the labyrinth pattern. This wrinkling transition has not been previously reported, and seems particular to critical demixing ferrofluids.

Fig. 2 shows a checkerboard of two microscope images of the same region, one type of squares focused at the air/liquid interface the other squares focused in the bulk. The wrinkles can be observed only at the surface of the liquid. If we move the focal plane of the microscope into the bulk<sup>33</sup> the wrinkles disappear, while the large scale undulations persist.

The nature of the top surface has a strong effect on the observed pattern. Fig. 3 shows reflection microscopy images of the same liquid as the one in Fig. 1, but the liquid is covered by a glass slip that replaces the liquid/air interface with a liquid/glass interface. The texture of the liquid under these circumstances is the same, however, without the small scale wrinkles.

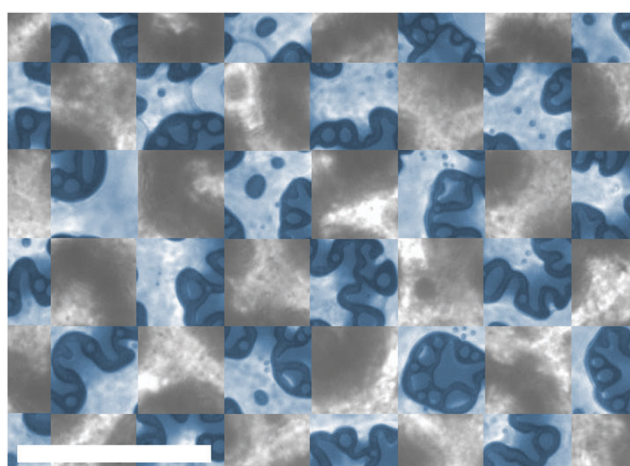


Fig. 2 Reflection microscopy image of a ferrofluid/2,6-lutidine/silicone (3:1:1) mixture at an external magnetic induction of  $\mu_0 H = 9.3$  mT. We show checker-board sections of the surface (blue squares) and the bulk (gray squares). Small scale wrinkling can only be observed at the air/liquid interface. The scale bar is 100  $\mu\text{m}$ .

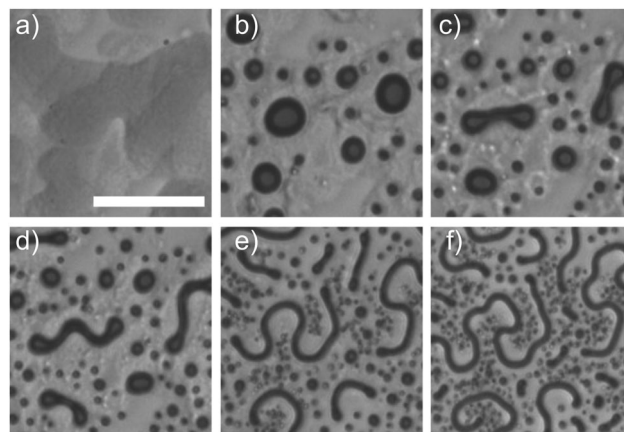


Fig. 3 Reflection microscopy image of a ferrofluid/2,6-lutidine/silicone (3:1:1) mixture at an external magnetic induction of (a)  $\mu_0 H = 0.1$  mT, (b)  $\mu_0 H = 2.9$  mT, (c)  $\mu_0 H = 3.6$  mT, (d)  $\mu_0 H = 4.8$  mT, (e)  $\mu_0 H = 6.3$  mT, (f)  $\mu_0 H = 9.3$  mT, normal to the film having a silicone oxide support and a glass cover slip surface at the top. (a) Exhibits a homogeneous image with no texture. Demixing of the fluid into ferrofluid enriched and ferrofluid poorer phases occurs between (a and b). The cylindrical droplets get deformed into a labyrinth droplet as one increases the field. The onset of the shape transition is between (b and c). Between (c and d) start to elongate. No wrinkling is observed at higher fields. Scale bar in figure (a) is 100  $\mu\text{m}$ .

We can observe a demixing transition and a shape transition but no wrinkling. The wrinkling transition is also absent (data not shown) when using hydrophobic unbreakable plastic cover-slips, or silanized cover slips as the top surface.

In order to quantify the wrinkles we introduce two metrics (see Fig. 4), one measuring the path length  $s - s'$  of a segment of the droplet path, and a second by measuring the short cut length  $|\mathbf{r}(s) - \mathbf{r}(s')|$  between the segment ends. By collecting all possible segments of length  $s - s'$  of the droplet we may average the shortcut length over these segments. The logarithm of the ratio of the segment *versus* average short cut length defines our wrinkle number:

$$\text{wr}(s - s') = \ln \frac{s - s'}{\langle |\mathbf{r}(s) - \mathbf{r}(s')| \rangle} \quad (1)$$

The larger  $\text{wr}$  the more travel distance we save by taking the short cut instead of the segment path. In Fig. 4 we plot the wrinkle number as a function of the segment length for a fixed value of  $H$  for the red droplet in Fig. 1g (black data points) and for the central droplet in Fig. 3f (gray data points).<sup>34</sup> For both droplets the wrinkle number increases with the segment length starting at the noise level of the digitization of the image. The small scale wrinkles of the droplet of Fig. 1g can be clearly seen in the black data as a region of negative curvature in this plot. The increase in the wrinkle number takes a rest when we have surmounted the typical path length ( $\approx 30$   $\mu\text{m}$ ) of a small scale wrinkle. It is therefore possible to introduce an intermediate path lengths  $b$  that short cuts the small scale wrinkles but not the long scale undulations (blue line in Fig. 4). This allows to subdivide the wrinkle number of the full length droplet into a short scale wrinkle number  $\text{wr}_<$  and a large scale wrinkle number  $\text{wr}_>$  for each value of the magnetic field, where the

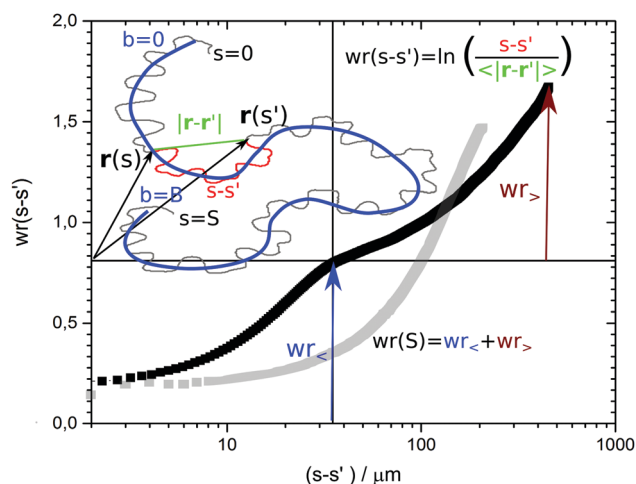


Fig. 4 Plot of the wrinkle number versus the segment length at a magnetic field of 9.3 mT (black cf. Fig. 1g) for the free surface and (gray cf. Fig. 3f) for the glass covered surface. The free surface data exhibits a knee such that the total wrinkle number can be divided into the sum of the small scale wrinkle number  $wr_{<}$  and the large scale wrinkle number  $wr_{>}$  by introducing the intermediate bulk path length (blue line). No such knee is observed in the data from the glass covered surface of Fig. 3f.

short scale wrinkling is the logarithm of the ratio of the total path length  $S$  of the droplet at the surface versus the total intermediate path length  $B$  of the bulk of the droplet:

$$wr_{<} = \ln(S/B) \quad (2)$$

and

$$wr_{>} = \ln(B/|\mathbf{r}(S) - \mathbf{r}(0)|). \quad (3)$$

No such separation of length scale is observed in the gray data of the non-wrinkled labyrinth droplet of Fig. 3f.

In Fig. 5 we plot both wrinkle numbers,  $wr_{<}$  and  $wr_{>}$ , of the red droplet of Fig. 1 versus the external magnetic induction. It can be clearly seen that the onset of the small scale wrinkling is at a different field than the critical field  $H_{lab}$  for the shape transition toward the labyrinth, measured by either the onset of the large scale wrinkle number  $wr_{>}$  or the surface path length  $S$ . The shape transition from circular toward dogbone and labyrinth patterns of non critical mixtures has been well studied and one can write the path length  $S$  or  $B$  of a droplet as

$$S, B = A_{s,b} / \zeta_{s,b} \exp\left(-\frac{1}{2N_{Bo}^{s,b}}\right) \quad (4)$$

where  $N_{Bo}^{s,b} = (\Delta\chi^{eff})^2 t_{s,b} \mu_0 H^2 / 2\sigma_{s,b}$  is the magnetic bond number with  $t_{s,b}$  the thickness in the direction normal to the silicon oxide surface and  $A_{s,b}$  the lateral area of the droplet,  $\zeta_{s,b}$  and  $\sigma_{s,b}$ , the width and the interfacial tension of the interface between the two phases, and  $\Delta\chi^{eff}$  the effective susceptibility contrast between the two phases.<sup>37</sup> The index  $s$  corresponds to the droplet properties at the surface, while the index  $b$  indicates the same properties in the bulk of the liquid. The shape transition is a result of the competition of repulsive dipolar interactions within the droplet trying to elongate the droplet

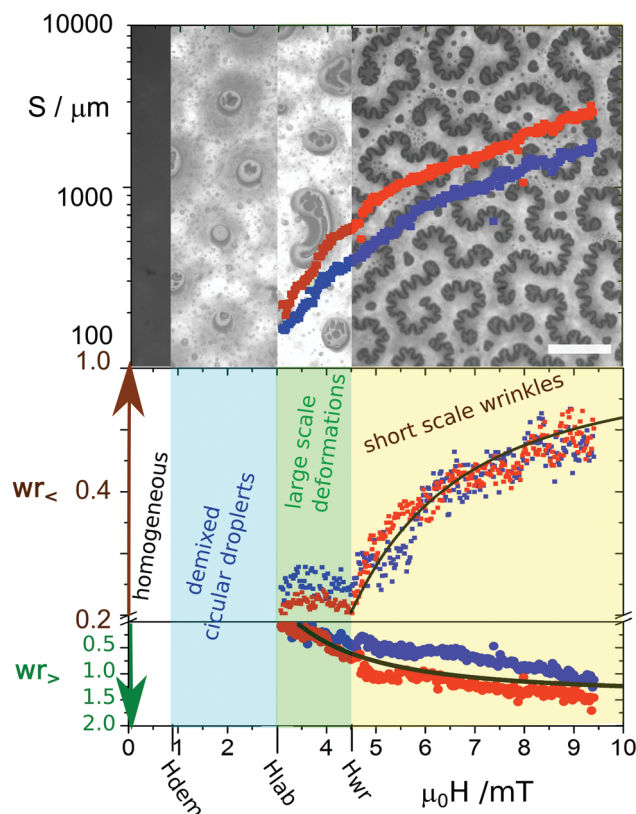


Fig. 5 Plot of the surface path length  $S$ , the small scale wrinkle number  $wr_{<}$ , and the large scale wrinkle number  $wr_{>}$  versus the external magnetic induction for the structures marked with red and blue in Fig. 1. Small scale wrinkles only occur after the circle versus dogbone/labyrinth transition. The black lines are fits according to eqn (5) and a similar equation for  $wr_{>}$ . Scale bar in the images is 100  $\mu\text{m}$ . A movie of the sequence of transitions can be viewed in ref. 35.

and the interfacial tension between the two phases trying to render the droplet shape circular.

Here we study a system that is close to a critical demixing point. It is clear that the wetting behavior of the liquid with any surface will alter the demixing behavior, either by moving the interfacial liquid closer or further from the critical demixing point. If the surface happens to move the interfacial liquid further from the critical demixing point, then the contrast between the two liquids will increase ( $\sigma_s/t_s > \sigma_b/t_b$  or  $N_{Bo}^s < N_{Bo}^b$ ) and the domain wall width between the two phases will decrease close to the surface ( $\zeta_s < \zeta_b$ ).

The total free energy can be divided into a surface and a bulk part, and both are (almost) extensive in the thicknesses  $t_s < t_b$  of each region. It is therefore reasonable to assume the surface to be enslaved by the bulk. The bulk droplet will therefore assume its equilibrium path length independent of the surface. When the bulk droplet shape becomes unstable the length of the droplets grows relatively slow with the magnetic field compared to the surface because of its smaller Bond number.

The area of the surface is smaller than that of the bulk at the onset of the shape instability. Therefore the initial length of the surface path is shorter than that of the bulk. However, the surface path length soon catches up with the bulk due to its smaller

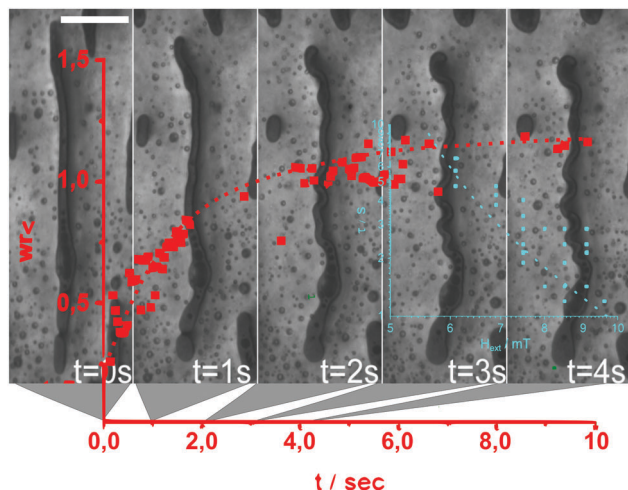


Fig. 6 Relaxation of an unwrinkled extended droplet back to its wrinkled equilibrium shape after switching of an oscillating in plane field for a normal field of 6.3 mT. The scale bar is 50  $\mu\text{m}$ . We extract a plot of the small scale wrinkle number  $wr_{<}(t)$  as a function of time (red) from the images of such movie for a normal field of 6.9 mT. The relaxation time  $\tau$  extracted from such graph is plotted versus the normal external field in the inset (cyan). It follows a  $\tau \propto 1/H_{\text{ext}}(H_{\text{ext}} - H_{\text{wr}})$  behavior that is expected theoretically when assuming magnetic forces to be balanced by viscous forces. A movie of the relaxation can be viewed in ref. 35.

Bond number. When the surface length becomes larger than the bulk this is the situation when the surface path has to start wrinkling. This explains why the wrinkling transition happens after the circle-to-dog-bone (labyrinth) transition.

Inserting eqn (4) into eqn (2) we obtain a theoretical prediction for the small scale wrinkles:

$$wr_{<} = \ln\left(\frac{A_s \xi_b}{A_b \xi_s}\right) + \frac{1}{2} \left( \frac{1}{N_{\text{Bo}}^b} - \frac{1}{N_{\text{Bo}}^s} \right) \quad (5)$$

The black lines in Fig. 5 are fits ( $A_s \xi_b / A_b \xi_s = 30$ ,  $H^2 / 2(1/N_{\text{Bo}}^b - 1/N_{\text{Bo}}^s) = 13 \text{ (mT)}^2$ ) to the measured wrinkle numbers using eqn (5) for  $wr_{<}$ , a similar equation for  $wr_{>}$ , and the assumption that the air/liquid interface moves the interfacial liquid away from the critical demixing point. In the case that the interface moves the liquid closer to the critical demixing point the interfacial path length will not grow longer than the bulk path length and because we assume that the bulk enslaves the surface, the bulk will not be wrinkled by the surface. This is what we believe happens in our experimental mixture in Fig. 3 when covering the liquid with a glass cover slip.

The wrinkles are a thermodynamic equilibrium structure that does not depend on transport coefficients such as the viscosity. We can erase the wrinkles using an in plane oscillating magnetic field of strength 1.6 mT and frequency 10 Hz superposed to the static normal field. An in-plane field in the y-direction induces smooth stripe patterns that relax back to a wrinkled labyrinth when we switch off the in-plane field. In Fig. 6 we depict the pattern for various times after switching off the in-plane field. One can clearly see the relaxation into a wrinkled structure (see the movie Relaxation.avi in the ESI†<sup>35</sup>). In Fig. 6 we plot the

time dependence of the small scale wrinkle number  $wr_{<}(t)$  versus the time (red). The experimental relaxation can be described by a sigmoidal relaxation process:

$$wr_{<}(t) = wr_{<}^{\infty} \tanh((t - t_0)/\tau) \quad (6)$$

with a relaxation time  $\tau(H_{\text{ext}}) \propto 1/H_{\text{ext}}(H_{\text{ex}} - H_{\text{wr}})$  (blue). Such relaxation time dependence is expected from the balance of magnetic forces (that depend on the product of the magnetic field and the magnetization, and must vanish for  $H_{\text{ext}} - H_{\text{wr}}$ ) and viscous forces (that do not depend on the magnetic field).

In conclusion, a ferrofluid mixture close to a critical demixing point is sensitive enough to have substantially different properties near a surface as compared to the bulk. The differences in properties result in different equilibrium lengths of the surface and bulk path lengths of droplets having undergone a dipolar shape transition. Since both parts of the droplets are coupled, the longer surface path has to wrinkle. The experimental geometry of the wrinkles agrees well with predictions taken of both path lengths from well known theories about modulated phases.

## Conflicts of interest

There are no conflicts to declare.

## Acknowledgements

NW thanks the Alexander von Humboldt foundation for a AvH fellowship. J. B. acknowledges financial support by a Ghana MOE – DAAD joined fellowship. We thank Florian Johannes Maier for helping with the numerical analysis of the droplets.

## References

- 1 E. Cerda and L. Mahadevan, Geometry and physics of wrinkling, *Phys. Rev. Lett.*, 2003, **90**, 074302.
- 2 N. Liu, Z. Pan, L. Fu, C. Zhang, B. Dai and Z. Liu, The origin of wrinkles on transferred graphene, *Nano Res.*, 2011, **4**, 996–1004.
- 3 J. Huang, M. Juskiewicz, W. H. de Jeu, E. Cerda, T. Emrick, N. Menon and T. P. Russell, Capillary wrinkling of floating thin polymer films, *Science*, 2007, **317**, 650–653.
- 4 K. Efimenko, M. Rackaitis, E. Manias, A. Vaziri, L. Mahadevan and J. Genzer, Nested self-similar wrinkling patterns in skins, *Nat. Mater.*, 2005, **4**, 293–297.
- 5 M. Seul and D. Andelman, Domain Shapes and Patterns: The Phenomenology of Modulated Phases, *Science*, 1995, **267**, 476–483.
- 6 H. Wang, Y. Zhu, C. Boyd, W. Luo, A. Cebers and R. E. Rosensweig, Periodic branched structures in a phase-separated magnetic colloid, *Phys. Rev. Lett.*, 1994, **72**, 1929–1932.
- 7 Yu A. Buyevich and A. O. Ivanov, Equilibrium properties of ferrocolloids, *Physica A*, 1992, **190**, 276–294.
- 8 A. Yu Zuberev and L. Yu Iskakova, Condensation phase transitions in ferrofluids, *Physica A*, 2004, **335**, 325–338.

- 9 A. Yu. Zubarev and L. Yu. Iskakova, Direct and inverse domain structures in ferrofluids, *Physica A*, 2006, **367**, 55–68.
- 10 A. Yu. Zubarev and L. Yu. Iskakova, Yield stress in thin layers of ferrofluids, *Physica A*, 2006, **365**, 265–281.
- 11 L. Yu. Iskakova, A. P. Romanchuk and A. Yu. Zubarev, Phase and structural transformations in magnetorheological suspensions, *Physica A*, 2006, **366**, 18–30.
- 12 V. S. Mendeleev and A. O. Ivanov, Ferrofluid aggregation in chains under the influence of a magnetic field, *Phys. Rev. E: Stat., Nonlinear, Soft Matter Phys.*, 2004, **70**, 051502.
- 13 Yu. A. Buyevich and A. Yu. Zubarev, Domain structures in thin layers of a ferrocolloid, *J. Phys. II*, 1993, **3**, 1633–1645.
- 14 A. G. Papatthaniou and A. G. Boudouvis, Three-lobe-shaped equilibrium states in magnetic liquid bridges, *Phys. Rev. E: Stat., Nonlinear, Soft Matter Phys.*, 2002, **65**, 035302.
- 15 R. E. Rosensweig, M. Zahn and R. Shumovich, Labyrinthine instability in magnetic and dielectric fluids, *J. Magn. Magn. Mater.*, 1983, **39**, 127–132.
- 16 J. E. Martin and J. Odinek, Evolution of structure in a quiescent Electrorheological fluid, *Phys. Rev. Lett.*, 1992, **69**, 1524–1527.
- 17 H. McConnell, Structures and Transitions in Lipid Monolayers at the Air-Water Interface, *Annu. Rev. Phys. Chem.*, 1991, **42**, 171–195.
- 18 K. Y. C. Lee and H. M. McConnell, Quantized symmetry of liquid monolayer domains, *J. Phys. Chem.*, 1993, **97**, 9532–9539.
- 19 H. A. Stone and H. M. McConnell, Hydrodynamics of Quantized Shape Transitions of Lipid Domains, *Proc. – R. Soc. Edinburgh, Sect. A: Math. Phys. Sci.*, 1995, **448**, 97–111.
- 20 P. Heinig, P. Steffen, S. Wurlitzer and T. M. Fischer, Two-Dimensional Pendant Droplet Tensiometry in a Langmuir Monolayer, *Langmuir*, 2001, **17**, 6633–6637.
- 21 A. H. Eschenfelder, *Magnetic bubble technology*, Springer-Verlag, Berlin, 1980.
- 22 C. L. Dennis, R. P. Borges, L. D. Buda, U. Ebels, J. F. Gregg, M. Hehn, E. Jouguelet, K. Ounadjela, I. Petej, I. L. Prejbeanu and M. J. Thornton, The defining length scales of mesomagnetism: a review, *J. Phys.: Condens. Matter*, 2002, **14**, R1175–R1262.
- 23 H. Vandeparre, M. Piñeira, F. Brau, B. Roman, J. Bico, C. Gay, W. Bao, C. N. Lau, P. M. Reis and P. Damman, Wrinkling Hierarchy in Constrained Thin Sheets from Suspended Graphene to Curtains, *Phys. Rev. Lett.*, 2011, **106**, 224301.
- 24 M. He, N. Xin, Y. Liu and Y. Zhang, Determination of critical properties for binary and ternary mixtures of short chain alcohols and alkanes using a flow apparatus, *J. Supercrit. Fluids*, 2015, **104**, 19–28.
- 25 C. A. Grattoni, R. A. Dawe, C. Y. Seah and J. D. Gray, Lower Critical Solution Coexistence Curve and Physical Properties (Density, Viscosity, Surface Tension, and Interfacial Tension) of 2,6-Lutidine + Water, *J. Chem. Eng. Data*, 1993, **38**, 516–519.
- 26 I. Szalai and S. Dietrich, Global phase diagrams of binary dipolar fluid mixtures, *Mol. Phys.*, 2005, **103**, 2873–2895.
- 27 S. M. Cattes, S. H. L. Klapp and M. Schoen, Condensation, demixing, and orientational ordering of magnetic colloidal suspensions, *Phys. Rev. E: Stat., Nonlinear, Soft Matter Phys.*, 2015, **91**, 052127.
- 28 K. Lichtner, A. J. Archer and S. H. L. Klapp, Phase separation dynamics in a two dimensional magnetic mixture, *J. Chem. Phys.*, 2012, **136**, 024502.
- 29 B. Groh and S. Dietrich, Ferroelectric phase in Stockmayer fluids, *Phys. Rev. E: Stat. Phys., Plasmas, Fluids, Relat. Interdiscip. Top.*, 1994, **50**, 3814–3833.
- 30 B. Groh and S. Dietrich, Long-ranged orientational order in dipolar fluids, *Phys. Rev. Lett.*, 1994, **72**, 2422–2425.
- 31 A. B. Yener and S. H. L. Klapp, Self-assembly of three-dimensional ensembles of magnetic particles with laterally shifted dipoles, *Soft Matter*, 2016, **12**, 2066–2075.
- 32 J. Bugase, J. Berner and Th. M. Fischer, Magnetic field induced modulated phases in a ferrofluid lutidine silicone oil mixture, *Soft Matter*, 2016, **12**, 8521–8527.
- 33 Note that the phase depleted of ferrofluid is fully transparent, and we can resolve objects also in the bulk of the fluid mixture.
- 34 The images are binarized, skeletonized, and dangling branches are cut off the skeleton to produce a curve  $\mathbf{r}(s)$ . The distance  $s - s'$  is then computed from the distances of consecutive pixels. Since the skeletonized curve has a thickness of one pixel there is some chance that the skeletonization of the curve will cut a single real droplet into virtual two droplets. This is what happens in the top of Fig. 5 at some data points near  $H = 7$  mT and  $H = 8$  mT. One droplet is wrongly split into two by the skeletonization. The wrinkle number does not react to the splitting.
- 35 A movie Transitions.avi showing the sequence of transitions and a movie Relaxation.avi showing the relaxation from stretched droplets versus the wrinkled state (ESI†).
- 36 R. de Koker and H. M. McConnell, Circle to dogbone: shapes and shape transitions of lipid monolayer domains, *J. Phys. Chem.*, 1993, **97**, 13419–13424.
- 37 D. Andelman and R. E. Rosensweig; The Phenomenology of Modulated Phases: From Magnetic Solids and Fluids to Organic Films and Polymers, in *Polymers, Liquids and Colloids in Electric Fields: Interfacial Instabilities, Orientation, and Phase-Transitions*, ed. Y. Tsori and U. Steiner, Series in Soft Condensed Matter, World Scientific, Singapore, 2009, ch. 1, vol. 2, pp. 1–56.



## **P3 Lattice symmetries and topologically protected transport of colloidal particles**

Johannes Loehr<sup>a</sup>, Daniel de las Heras<sup>b</sup>, Michael Loenne<sup>c</sup> **Jonas Bugase<sup>a</sup>**,  
Adam Jarosz<sup>d</sup>, Maciej Urbaniak<sup>d</sup>, Feliks Stobiecki<sup>d</sup>, Andreea Tomita<sup>e</sup>,  
Rico Huhnstock<sup>e</sup>, Iris Koch<sup>e</sup>, Arno Ehresmann<sup>e</sup>, Dennis Holzinger<sup>e</sup>,  
and Thomas M. Fischer<sup>\*a</sup>

<sup>a</sup>Experimental Physics Universität Bayreuth, 95440 Bayreuth, Germany

<sup>b</sup>Theoretical Physics Universität Bayreuth, 95440 Bayreuth, Germany

<sup>c</sup>Mathematics, Institute of Physics and Mathematics Universität Bayreuth,  
95440 Bayreuth, Germany

<sup>d</sup>Institute of Molecular Physics, Polish Academy of Sciences,  
ul. M. Smoluchowskiego 17, 60-179 Poznań, Poland

<sup>e</sup>Institute of Physics and Center for Interdisciplinary Nanostructure Science and  
Technology (CINSA-T), University of Kassel, Heinrich-Plett-Strasse 40, D-34132 Kassel,  
Germany

*Soft Matter*, 2017, **13**, pp(5044-5075)

**DIO:10.1039/C7SM00983F**

Received 17<sup>th</sup> May, 2017, Accepted 5<sup>th</sup> July, 2017

---

### **My Contribution**

I designed, performed and analyzed the experiments with the four fold symmetry and contributed to the writing of the manuscript but it was mainly done by J. Loehr, D. de las Heras and T. M. Fischer. Johannes Loehr designed, performed and analyzed the experiments with all other symmetries. The theoretical framework was done by J. Loehr, D. de las Heras, M. Loenne and T. M. Fischer.




 Cite this: *Soft Matter*, 2017,  
13, 5044

## Lattice symmetries and the topologically protected transport of colloidal particles†

 Johannes Loehr,<sup>a</sup> Daniel de las Heras,<sup>ib</sup> Michael Loenne,<sup>c</sup> Jonas Bugase,<sup>a</sup>  
Adam Jarosz,<sup>d</sup> Maciej Urbaniak,<sup>d</sup> Feliks Stobiecki,<sup>d</sup> Andreea Tomita,<sup>e</sup>  
Rico Huhnstock,<sup>e</sup> Iris Koch,<sup>e</sup> Arno Ehresmann,<sup>e</sup> Dennis Holzinger<sup>e</sup> and  
Thomas M. Fischer<sup>ib</sup>\*<sup>a</sup>

The topologically protected transport of colloidal particles on top of periodic magnetic patterns is studied experimentally, theoretically, and with computer simulations. To uncover the interplay between topology and symmetry we use patterns of all possible two dimensional magnetic point group symmetries with equal lengths lattice vectors. Transport of colloids is achieved by modulating the potential with external, homogeneous but time dependent magnetic fields. The modulation loops can be classified into topologically distinct classes. All loops falling into the same class cause motion in the same direction, making the transport robust against internal and external perturbations. We show that the lattice symmetry has a profound influence on the transport modes, the accessibility of transport networks, and the individual transport directions of paramagnetic and diamagnetic colloidal particles. We show how the transport of colloidal particles above a two fold symmetric stripe pattern changes from universal adiabatic transport at large elevations *via* a topologically protected ratchet motion at intermediate elevations toward a non-transport regime at low elevations. Transport above four-fold symmetric patterns is closely related to the two-fold symmetric case. The three-fold symmetric case however consists of a whole family of patterns that continuously vary with a phase variable. We show how this family can be divided into two topologically distinct classes supporting different transport modes and being protected by proper and improper six fold symmetries. We discuss and experimentally demonstrate the topological transition between both classes. All three-fold symmetric patterns support independent transport directions of paramagnetic and diamagnetic particles. The similarities and the differences in the lattice symmetry protected transport of classical over-damped colloidal particles *versus* the topologically protected transport in quantum mechanical systems are emphasized.

 Received 17th May 2017,  
Accepted 5th July 2017

DOI: 10.1039/c7sm00983f

[rsc.li/soft-matter-journal](http://rsc.li/soft-matter-journal)

## 1 Introduction

The theoretical description of topological insulators highlighted the connection between symmetry and topology in quantum phases of matter.<sup>1,2</sup> Symmetries and the topology of quantum matter are deeply intertwined. The exploration of the

role of symmetry in topological phases has led to a topological classification of phases of matter.<sup>3</sup> The complex quantum wave function of an excitation in a lattice can be considered as a two dimensional vector with real and imaginary part components that lives in the first Brillouin zone of the reciprocal lattice. When one identifies the borders of the first Brillouin zone it is topologically a torus. Attaching the quantum wave function vector to this torus mathematically defines a vector bundle that can be characterized by Chern classes. These classes must be compatible with the symmetries of the Hamiltonian. Chern classes are symmetry protected against perturbations compatible with the symmetry. Amongst the most prominent symmetries protecting topological insulators are the time reversal symmetry, the particle hole symmetry, but also the point symmetry of the lattice.<sup>4–6</sup> Different constraints of the lattice symmetries cause physical distinct effects on lattices of different symmetry.<sup>7,8</sup> In topological nontrivial systems Dirac cones play a crucial role. The number of these Dirac cones in a

<sup>a</sup> Experimental Physics, Universität Bayreuth, 95440 Bayreuth, Germany.  
E-mail: Thomas.Fischer@uni-bayreuth.de

<sup>b</sup> Theoretical Physics, Universität Bayreuth, 95440 Bayreuth, Germany

<sup>c</sup> Mathematics, Institute of Physics and Mathematics, Universität Bayreuth,  
95440 Bayreuth, Germany

<sup>d</sup> Institute of Molecular Physics, Polish Academy of Sciences,  
ul. M. Smoluchowskiego 17, 60-179 Poznań, Poland

<sup>e</sup> Institute of Physics and Center for Interdisciplinary Nanostructure Science and  
Technology (CINSaT), University of Kassel, Heinrich-Plett-Strasse 40,  
D-34132 Kassel, Germany

† Electronic supplementary information (ESI) available. See DOI: 10.1039/c7sm00983f

hexagonal and a square lattice differ and their robustness against perturbations is different if they are located at a high symmetry point, a high symmetry line or a generic location of the Brillouin zone.<sup>9</sup>

The variety of phenomena enriches when considering time dependent periodically driven systems. In such systems the frequency or energy of an excitation is conserved only modulo the frequency of the driving field and the first frequency zone can be folded into a circle in the same spirit as folding the first Brillouin zone into a torus.<sup>10,11</sup> Floquet topological insulators are one example of topologically non trivial systems arising from periodic driving.

The discreteness of spectra of quantum phenomena is one ingredient shared also with spectra of bound classical waves and with the nature of topological invariants. The quantum Hall effect is one important example, where transport coefficients increase in discrete steps that contain only fundamental constants of nature including Planck's constant. The discreteness of the steps are caused by topology.<sup>12</sup>

The topological classification of phases is not restricted to quantum systems. There are other non-quantum vector waves in lattices<sup>13–18</sup> that can be characterized in just the same way. Hence the topological discreteness also appears in many classical wave like systems. The topological characterization is not restricted to classical vector bundles. It has been applied to non-equilibrium stochastic systems that describe biochemical reactions.<sup>19</sup> We applied the concept of topological protection to the dissipative transport of magnetic colloidal particles on top of a modulated periodic magnetic potential.<sup>20,21</sup> There the transport of the point particle is fully characterized by the topology of the mathematical manifold on which it moves. The manifold does not carry any vector property. It can be characterized by its genus, a topological invariant somewhat more descriptive than the Chern class. We have shown that the driven transport of paramagnetic or diamagnetic colloidal particles above a two dimensional lattice is topologically protected by topological invariants of the modulation loops used to drive the transport.<sup>20,21</sup> Non-topological transport of particles in a dissipative environment is usually vulnerable because of a spreading of the driven motion with the distribution of properties of the classical particles<sup>22–28</sup> as well as due to the abundance of possible hydrodynamic instabilities<sup>29,30</sup> that limit the control over their motion. Topologically protected particle transport in contrast is robust against sufficiently small continuous modifications of the external modulation. Only when the modulation loops are changed drastically they will fall into another topological class, and the direction of the transport changes in a discrete step.

In this work we investigate how the topological classes of modulation loops are affected by the lattice symmetry. We use experiments, theory and simulations to study transport above lattices of all possible two dimensional magnetic point symmetry groups and examine the impact of the symmetry on the number of transport modes, the number of topological invariants and on the type (adiabatic or ratchet) of transport. We show that lattice symmetry, as in topological crystalline insulators,<sup>4–9</sup> has a profound influence on the topologically protected transport modes.

Applying periodic boundary conditions the unit cell of each lattice is a torus, which defines the action space. That is, the space in which the colloids move. The colloids are driven with periodic modulation loops of an external magnetic field, the direction of which defines the control parameter space. As a result of the interplay between the external magnetic field and the static magnetic field of the pattern, action space is divided into accessible and forbidden regions for the colloidal particles. For every point in an accessible region there exist a direction of the external magnetic field such that the magnetic potential has a minimum at that point. The borders between different regions in action space are characterized by special objects in control space. Modulation loops of the external field that wind around these special objects in control space cause colloidal transport along lattice vectors in action space.

In ref. 20 and 21 we studied the motion of colloids above hexagonal and square patterns, respectively. Here, we extend our previous studies in several ways. We corroborate the theory developed in ref. 20 and 21 with experiments on four-fold symmetric patterns and prove experimentally the existence of ratchet modes in the six-fold symmetric patterns. We also develop a theory for two- and three-fold patterns and prove their validity with experiments. Moreover, we find theoretically two new topological transitions, one in the non-universal stripe pattern, and one in the family of three-fold patterns. All theoretical predictions are tested experimentally.

## 2 Colloidal transport system

In this section we introduce a soft matter system for Floquet crystalline symmetry protected driven transport of colloidal particles on top of two dimensional magnetic lattices of different symmetry.

### 2.1 Magnetic colloids on magnetic lattices

Our system consists of a two dimensional periodic magnetic film having domains magnetized in the  $z$ -direction normal to the film (Fig. 1a). We consider a film that has as much area

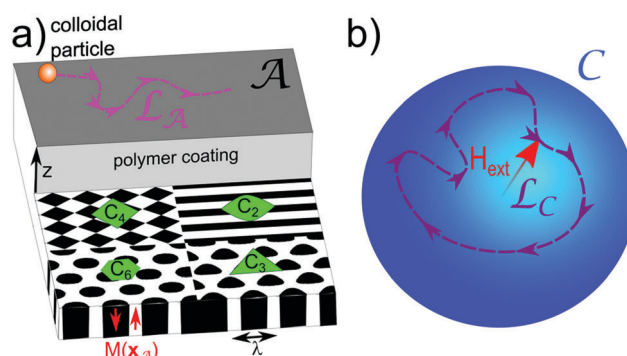


Fig. 1 (a) Magnetic pattern of symmetry  $C_2$ ,  $C_3$ ,  $C_4$ , and  $C_6$  with wavelength  $\lambda = 2\pi/Q$  and magnetization  $M(\mathbf{x}_A)$ . The magnetic colloidal particles move in the two dimensional action space  $\mathcal{A}$  on top of the film at fixed elevation  $z > \lambda$ . (b) A modulation loop  $\mathcal{L}_C$  of the external magnetic field  $\mathbf{H}_{\text{ext}}$  in the control space  $\mathcal{C}$  causes a transport loop  $\mathcal{L}_A$  of the colloidal particle.

magnetized in the  $+z$  as in the  $-z$  direction. The magnetic field  $\mathbf{H}^p$  of the pattern can be derived from a scalar magnetic potential

$$\mathbf{H}^p = -\nabla\psi \quad (1)$$

that satisfies the Laplace equation and can be written as

$$\psi = \sum_{\mathbf{Q}} \psi_{\mathbf{Q}} e^{-Qz} e^{i\mathbf{Q}\cdot\mathbf{x}_A} \quad (2)$$

where the sum is taken over the reciprocal lattice vectors  $\mathbf{Q}$  ( $Q = 2\pi/\lambda$  for the smallest non-zero reciprocal lattice vector) of the two dimensional lattice and  $\mathbf{x}_A$  is a two dimensional vector in the lattice plane. Lower Fourier modes dominate the sum (2) at higher elevation  $z$ .

Magnetic colloids can be confined in a liquid at a fixed elevation  $z$  that is larger than the wavelength of the pattern  $\lambda$  by coating the magnetic film with a polymer film of defined thickness or by immersing the colloids into a ferrofluid that causes magnetic levitation of the colloids.<sup>20</sup> We call the two-dimensional space in which the particles move the action space  $\mathcal{A}$ . We will use a number of geometric spaces and objects. Their definitions are listed in Appendix A.3. The positions of the particles are described by the vector  $\mathbf{x}_A$ .

Magnetic fields induce magnetic moments

$$\mathbf{m} = \chi_{\text{eff}} V \mathbf{H} \quad (3)$$

of the colloids of effective susceptibility  $\chi_{\text{eff}}$  and volume  $V$ . We define the colloidal potential  $U = H^2$ . The colloids thus acquire a potential energy  $E = -\chi_{\text{eff}} V U$ . This depends on the square of the total magnetic field  $\mathbf{H} = \mathbf{H}^p + \mathbf{H}_{\text{ext}}$  which is the superposition of a homogeneous time dependent external field to the heterogeneous pattern field. The potential energy  $E$  has a different sign for paramagnetic and diamagnetic colloids. Hence, paramagnetic particles move to positions that are maxima of  $U$  while diamagnetic colloids move to the minima.

We are particularly interested in the motion of paramagnetic and diamagnetic colloids at an elevation  $z > \lambda$  above the magnetic film such that only the contributions of the lowest non zero reciprocal lattice vectors to eqn (2) are relevant. At this elevation the response of the colloidal particles moving in action space  $\mathcal{A}$  becomes universal, *i.e.* independent of the details of the pattern. The symmetry of the pattern becomes the only important property. If the lattice has a proper  $C_N$  rotation symmetry or an improper  $S_N$  symmetry there are  $N$  reciprocal lattice vectors of lowest absolute value contributing to the universal scalar magnetic potential  $\psi^*$  and we find

$$\psi^* = \tilde{\psi} e^{-Qz} \sum_{n=0}^{N-1} \det(\mathcal{R}_N^n) e^{i[\mathcal{R}_N^n \cdot \mathbf{Q}] \cdot \mathbf{x}_A} \quad (4)$$

where  $\mathbf{Q}$  is one of the lowest absolute value reciprocal unit vectors and  $\mathcal{R}_N$  denotes a proper rotation matrix by  $2\pi/N$  ( $\det(\mathcal{R}_N) = +1$ ) or an improper rotation consisting of a rotation by  $2\pi/N$  and a reflection at the film plane ( $\det(\mathcal{R}_N) = -1$ ). The universal scalar magnetic potential is determined only by the symmetry of the lattice and a prefactor carrying a phase  $\phi$

and an amplitude,  $\tilde{\psi} = |\tilde{\psi}| \exp(i\phi)$ . The amplitude is irrelevant and the phase  $\phi$  is only important in the  $N = 3$  case. The scalar magnetic potential will be the same for all lattices sharing the same point symmetry.

Magnetization patterns generating such universal magnetic potentials are shown in Fig. 2. The magnetization is given by

$$\mathbf{M}(\mathbf{x}_A) = M_s \mathbf{e}_z \text{sign} \left( t(\phi) + \sum_{n=0}^{N-1} \cos([\mathcal{R}_N^n \cdot \mathbf{Q}] \cdot \mathbf{x}_A - \phi) \right) \quad (5)$$

with  $t(\phi) \approx \frac{1}{2} \cos(3\phi) \delta_{N,3}$  chosen such that the magnetic moment of a unit cell (UC) vanishes,

$$\int_{\text{UC}} \mathbf{M}(\mathbf{x}_A) d\mathbf{x}_A = 0. \quad (6)$$

The colloidal potential can now be reduced to the leading non-constant term, which is described by the universal colloidal potential:

$$U^* = e^{Qz} \mathbf{H}_{\text{ext}} \cdot \mathbf{H}^p(\mathbf{x}_A). \quad (7)$$

Note that the prefactor  $e^{Qz}$  rescales the potential such that it is independent of  $z$ , see eqn (4).

As we will see, adiabatic transport where the colloids adiabatically follow the maximum/minimum of the potential is possible along the crystallographic directions of the lattices when the potential is modulated with external fields. We call the space of the external field that may alter the colloidal potential the control space  $\mathcal{C}$ . Following eqn (7) we see that in the universal case changing the magnitude of  $\mathbf{H}_{\text{ext}}$  does not alter the position of the extrema of the colloidal potential. Control space  $\mathcal{C}$ , is thus a sphere of the external fields of constant magnitude. Each direction of the external field, which is a point in  $\mathcal{C}$ , produces a different colloidal potential (see Fig. 1b).

## 2.2 Lattice symmetries and topology

In Fig. 2 we depict the Wigner Seitz unit cells (with lattice vectors  $\mathbf{a}_1$  and  $\mathbf{a}_2$ ) of the periodic magnetic patterns defined by eqn (5) for  $N = 2, 3, 4$  and  $N = 6$  and show the points of these patterns having  $C_N$  (green) or  $S_2, S_4$  or  $S_6$  (red) symmetry. The patterns in Fig. 2 exhaust all possible single lattice constant ( $a_1 = a_2$ ) magnetic point groups in 2D. White areas of the unit cell are magnetized in the positive  $z$ -direction and black areas in the negative  $z$ -direction. There are other patterns creating the same universal potential, the field of which differs from the field of the patterns of Fig. 2 if experienced at lower  $Qz < 1$  (non-universal) elevation. Patterns having both  $C_N$  (green) and  $S_N$  (red) symmetries ( $N = 2$  or  $N = 4$ ) can be generated by using either proper or improper rotations.  $N = 3$  can be generated only with proper rotations. The  $C_6$  and  $S_6$  symmetries arise if we chose  $N = 3$  in eqn (5) and  $\phi = 0$  ( $\phi = \pi/6$ ). They can equally well be produced with  $N = 6$  and using proper (improper) rotations.

Let us start with the topological characterization of action space. For a lattice with two-fold symmetry there is only one relevant reciprocal lattice vector and therefore the lattice is

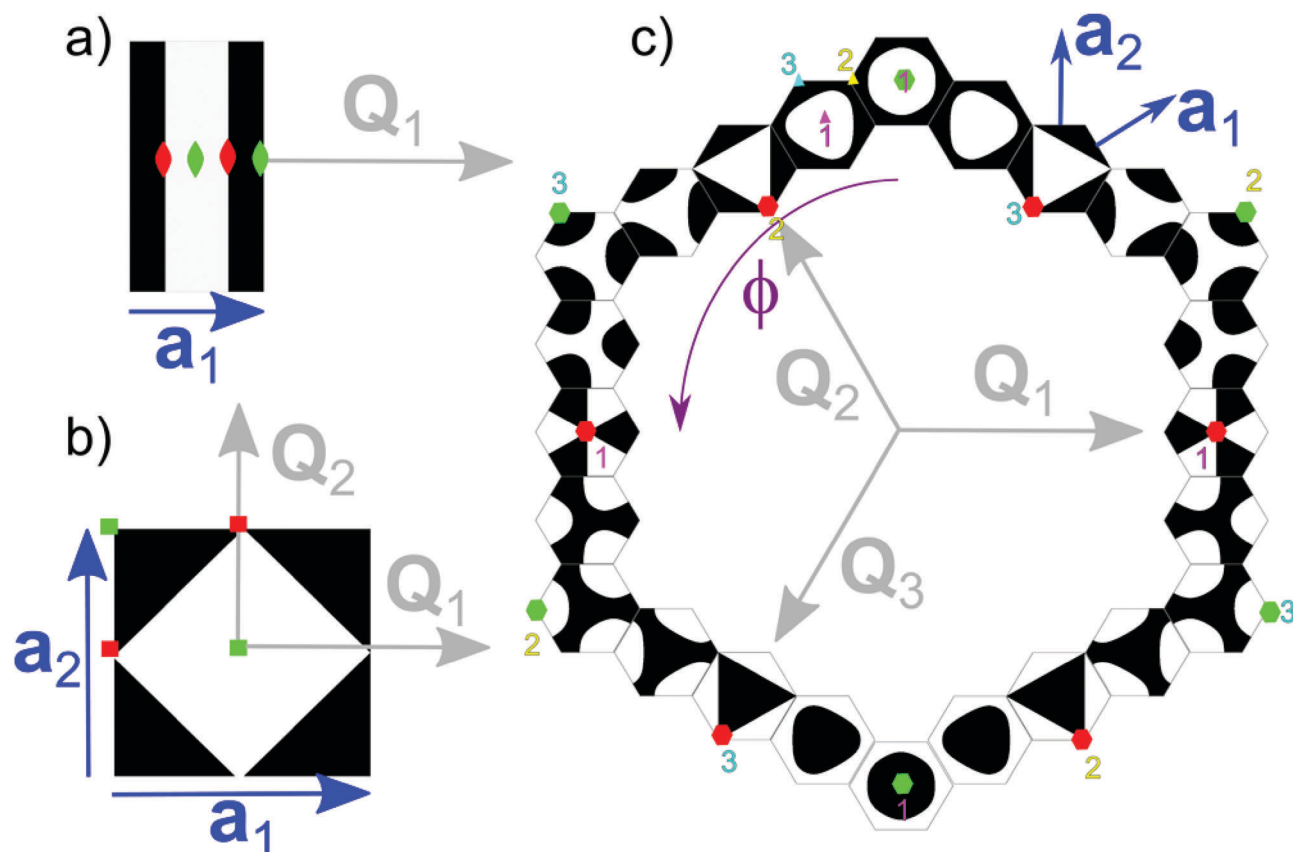


**Fig. 2** Wigner Seitz cells, unit vectors (blue), and reciprocal lattice vectors (gray) of all possible two dimensional single lattice constant magnetic point groups generating lattices. Black and white indicate the discrete down and up magnetized pattern according to eqn (5) that creates a universal colloidal potential at an elevation  $z > \lambda$  above the pattern. The  $\mathbf{Q}_1$  vector is always pointing to the right in the  $x$ -direction. In (a) we show the unit cell of the two-fold and in (b) of the four-fold symmetric pattern, and in (c) 24 smaller three-fold symmetric unit cells. The magnetic pattern of these three-fold symmetric unit cells continuously varies with the phase  $\phi$  of eqn (5). We show a sequence of such cells in steps of  $\Delta\phi = \pi/12$  starting at  $\phi = 0$  at the top. For each case there are 3 symmetry points with  $C_3$  symmetry per unit cell. They are shown in 3 different colors (pink, yellow, cyan) in the unit cell next to  $\phi = 0$ . For special values of  $\phi$  one of these three points acquires a proper or improper six-fold symmetry.  $N$ -Fold symmetric points of all unit cells are marked in green for proper rotation symmetries  $C_N$  and in red for improper rotation symmetries  $S_N$ .

quasi one dimensional (see Fig. 2a). Since the lattice is periodic, we can deform the Wigner Seitz cell to merge the opposite borders. For  $N = 2$  the Wigner Seitz cell is a one dimensional segment, and hence action space  $\mathcal{A}_2$  becomes topologically a circle. For all other symmetries, action space  $\mathcal{A}_N$ , with  $N > 2$ , is a torus.

Action space is topologically nontrivial for both  $N = 2$  and  $N > 2$  since both a circle and a torus have a hole. For  $N = 2$  there is one winding number around the hole, while for a torus there are two winding numbers. The winding number of action space  $\mathcal{A}$  has a very simple meaning in the underlying lattice. A winding around the circle (torus) corresponds to a translation by one unit vector in the lattice.

As we already mentioned, control space  $\mathcal{C}$  is a sphere of radius  $H_{\text{ext}}$ . The two-fold symmetric colloidal potential is independent of the in-plane external field component perpendicular to  $\mathbf{Q}_1$ . Therefore, in the two dimensional problem we only need a reduced control space  $\mathcal{C}_2^r$ , which is the intersection of  $\mathcal{C}$  with the plane spanned by  $\mathbf{Q}_1$  and the vector normal to the film  $\mathbf{n} = \mathbf{e}_z$ . Like action space  $\mathcal{A}_2$  the reduced control space  $\mathcal{C}_2^r$  is a circle.

The topology of the reduced control space  $\mathcal{C}_2^r$  is fundamentally different from the full control space  $\mathcal{C}$ . The latter is a genus zero spherical surface that has no holes. For this reason we can continuously deform any closed loop of the external field  $\mathcal{L}_C$  into any other loop  $\mathcal{L}_C'$ . This is not the case if we restrict the modulation loops to lie on the reduced control space  $\mathcal{C}_2^r$ , which is a circle with a hole. Modulation loops in  $\mathcal{C}_2^r$  can be characterized by their winding number around the hole  $w(\mathcal{L}_C^r)$ . The winding number is a topological invariant and we cannot continuously deform a modulation loop  $\mathcal{L}_C^r$  with one winding number  $w$  into another modulation loop  $\mathcal{L}_C^r$  with a different winding number  $w' \neq w$ .

### 2.3 Classification of modulation loops

The fundamental question that we address in this work is, what are the topological requirements for a modulation loop  $\mathcal{L}_C$  in control space to cause action loops  $\mathcal{L}_A$  with different, non vanishing winding numbers in action space and hence induce transport of the colloidal particles.

For  $N = 2$  the answer is simple in reduced control space  $\mathcal{C}_2^r$  but less obvious in full control space  $\mathcal{C}$ . Reduced control and

action space are non trivial. One might guess that the non-trivial topological classification of modulation loops in reduced control space directly translates into the same topological classification of induced action-loops, *i.e.*

$$w(\mathcal{L}_A) = w(\mathcal{L}_C), \quad \text{for } N = 2. \quad (8)$$

We will show that this indeed is the correct answer to the question for the universal case. But there are other, non-universal answers to this question. At low elevation the transport in the two-fold symmetric potential differs from this simple answer.

Eqn (8) does not hold in full control space, *i.e.* there are loops with  $w(\mathcal{L}_A) \neq w(\mathcal{L}_C)$  for any  $N$ . Otherwise there would not be transport since  $w(\mathcal{L}_C) = 0$  for any loop. Full control space  $\mathcal{C}$  becomes nontrivial if we puncture it at specific points or introduce even more complicated objects on it. The result is a constrained control space  $\tilde{\mathcal{C}}$ , for which the simple answer

$$w(\mathcal{L}_A) = w(\mathcal{L}_{\tilde{\mathcal{C}}}) \quad (9)$$

with  $w(\mathcal{L}_{\tilde{\mathcal{C}}})$  the winding numbers around the objects of  $\tilde{\mathcal{C}}$  holds. The task is to find the objects that we need to project onto full control space and figure out how winding around those objects allows for a classification of the modulation loops into classes that induce topologically different transport of colloids in action space.

## 2.4 Computer simulations

We use Brownian dynamics to simulate the motion of a single point paramagnetic colloid above the different patterns. The motion of the particle is described by the stochastic differential Langevin equation

$$\gamma \frac{d\mathbf{x}_A(t)}{dt} = -\nabla_A E(\mathbf{x}_A, \mathbf{H}_{\text{ext}}(t)) + \mathbf{f}(t),$$

with  $t$  the time,  $\gamma$  the friction coefficient, and  $\mathbf{f}$  a Gaussian random force. The variance of the random force is determined by the fluctuation-dissipation theorem. As usual, we integrate the equation of motion in time using a standard Euler algorithm. We always equilibrate the system before the modulation loop in control space starts, such that the colloidal particles always start in the minimum of the potential energy  $E$  at  $t = 0$ .

The phase diagrams of the transport modes that we present in the next sections were initially obtained with computer simulations and can now also be predicted theoretically.

## 2.5 Outline

The rest of the paper is organized as follows. In Section 3 we treat the case  $N = 2$ . The simplicity of  $\mathcal{C}_2^r$  allows us to visualize many concepts that cannot be visualized for  $N > 2$  such as the full dynamics in phase space. We also study the non-universal transport for  $N = 2$ , and the connection to previous works.<sup>32–35</sup> We outline the concept of topologically protected ratchets with this very simple example. We then extend the treatment of  $N = 2$  to the full control space, introducing the concept of the constrained control space  $\tilde{\mathcal{C}}$ . The case  $N = 4$  is related to the case  $N = 2$  and is treated in Section 4. In Section 5 we analyze the case  $N = 3$

that consists of a whole family of patterns continuously varying with the phase  $\phi$  of the pattern. This includes the two special cases,  $C_6$  symmetry ( $\phi = 0$ ) and  $S_6$  symmetry ( $\phi = \pi/6$ ). We find a new topological transition between  $C_6$ - and  $S_6$ -like three-fold symmetric lattices. Section 6 contains a discussion of the experiments, a comparison to the theoretical and numerical predictions, and a discussion of the results in comparison to quantum systems. Finally Section 7 summarizes the main conclusions concerning transport.

## 3 Two-fold symmetry

In this section we study the transport on top of a two-fold symmetric pattern. We start with the universal case and subsequently reduce the elevation of the colloids towards non universal cases. This allows us to first study the transition from topologically protected adiabatic motion towards ratchet motion, and then to a non transporting regime.

### 3.1 Theory

A stripe pattern is a magnetic pattern with two-fold symmetry (see Fig. 2a). The magnetic field of a thick ( $tQ > 1$ ,  $t$  being the thickness of the magnetic film) pattern of stripes of opposite magnetization  $\pm M$  alternating along the  $x$  direction reads:

$$\begin{aligned} H_x^p + iH_z^p &= \frac{2M}{\pi} \ln[\tan(Q(x + iz))] \\ &= \sum_{n=0}^{\infty} \frac{8M}{(2n+1)^2} e^{i(2n+1)Q(x+iz)}, \end{aligned} \quad (10)$$

where  $H_x^p$  are the (real) components of the pattern magnetic field, and in the last part of eqn (10) we have decomposed the field into its Fourier-components. The non-universal colloidal potential valid at any height  $z$  reads:

$$U = (H_x^p + H_{\text{ext}} \cos \varphi_{\text{ext}})^2 + (H_z^p + H_{\text{ext}} \sin \varphi_{\text{ext}})^2, \quad (11)$$

where

$$\mathbf{H}_{\text{ext}} = H_{\text{ext}} \begin{pmatrix} \sin \varphi_{\text{ext}} \\ \cos \varphi_{\text{ext}} \end{pmatrix}, \quad \varphi_{\text{ext}} \in [0, 2\pi] \quad (12)$$

denotes the external magnetic field lying in the reduced control space  $\mathcal{C}_2^r$ . In the limit  $Qz > 1$  the pattern field is well described by

$$\mathbf{H}^p(Qz > 1) = 8Me^{-Qz} \begin{pmatrix} \sin Qx \\ \cos Qx \end{pmatrix}, \quad Qx \in [0, 2\pi] \quad (13)$$

and the universal potential reads, *cf.* (7)

$$U^* = 8MH_{\text{ext}} \cos(Qx - \varphi_{\text{ext}}). \quad (14)$$

The over-damped Brownian motion of a colloidal particle in the  $x$ -direction is given by

$$\gamma \dot{x} = \zeta_{\text{eff}} V \frac{\partial U(x, \varphi_{\text{ext}})}{\partial x} + f_{\text{Brown}} \quad (15)$$

where  $f_{\text{Brown}}$  is a zero average random force fulfilling the fluctuation dissipation theorem,  $\gamma \propto \eta$  the friction coefficient

of the colloid in the liquid of viscosity  $\eta$ , and the effective magnetic susceptibility  $\chi_{\text{eff}}$  has a different sign for the paramagnets and diamagnets. Since our colloidal potential is sufficiently strong we can neglect the random force.

There are two kinds of colloidal dynamics that occur on separate time scales, when we adiabatically modulate the direction of the external field, which is described by  $\varphi_{\text{ext}}(t)$ . One is the intrinsic dynamics of the colloids on an intrinsic short time scale  $t_{\text{int}}$

$$\gamma \dot{x}(t_{\text{int}}) = \chi_{\text{eff}} V \frac{\partial U(x(t_{\text{int}}), \varphi_{\text{ext}}(t_{\text{fixed}}))}{\partial x} \quad (16)$$

with which the colloids follow the path of steepest descent along the slope of the colloidal potential along the  $x$ -direction towards an extremum in  $U$ . The typical angular speed of this intrinsic motion is of the order  $\omega_{\text{int}} = Q\dot{x} \propto e^{-Qz} \chi_{\text{eff}} \mu_0 M H_{\text{ext}} (QV^{1/3})^2 / \eta$ ; (the intrinsic angular frequency renormalizes by an additional factor  $tQ < 1$  for

thin magnetic films). Since the external modulation frequency  $\omega_{\text{ext}} \ll \omega_{\text{int}}$  is significantly slower this happens at fixed external field ( $\varphi_{\text{ext}}(t) = \varphi_{\text{ext}}(t_{\text{fixed}})$ ). The other timescale is an adiabatic creeping of the colloid with the maximum/minimum of the colloidal potential,

$$0 = \pm \frac{\partial U(x(t_{\text{ext}}), \varphi_{\text{ext}}(t_{\text{ext}}))}{\partial x}, \quad (17)$$

with a small velocity dictated by the much slower time scale  $t_{\text{ext}}$  of the external field modulation. Making use of the periodicity of the pattern we wrap the  $Qx$ -coordinate into a circle of circumference  $2\pi$  such that action space  $\mathcal{A}$  is a circle. Reduced control space  $\mathcal{C}_2^r$  is also a circle with radius  $H_{\text{ext}}$  and coordinate  $\varphi_{\text{ext}}$ . The full dynamics occurs in phase space  $\mathcal{C}_2^r \otimes \mathcal{A}$ , which is the product space of the reduced control and action space and thus a torus.

In Fig. 3a we depict the reduced phase space  $\mathcal{C}_2^r \otimes \mathcal{A}$ , together with the directions  $Qx$  of action space and  $\varphi_{\text{ext}}$  of the reduced

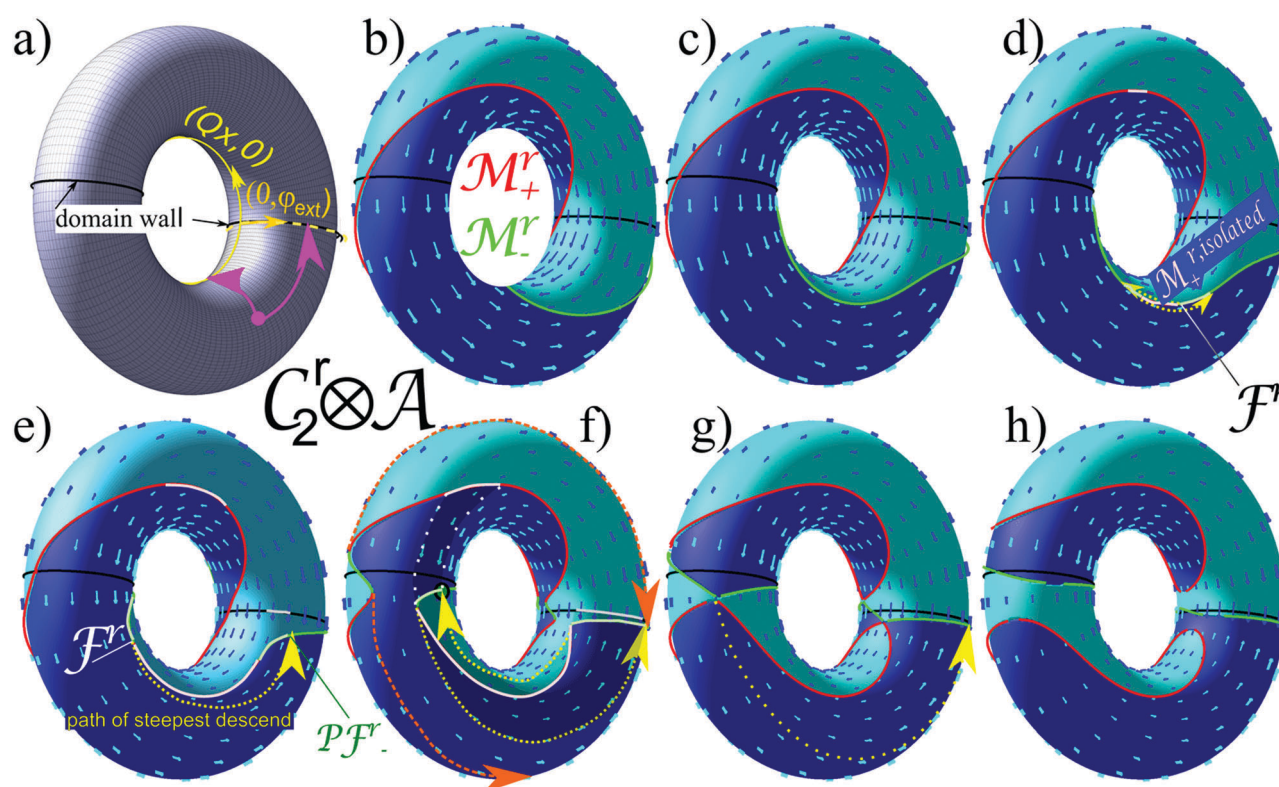


**Fig. 3** Reduced phase space of the two-fold symmetric system: (a) the black lines depict the locations of the domain walls separating regions of opposite magnetization in phase space, which are two copies of control space at  $x = 0, \pi$ . We may use the first one as reduced control space  $\mathcal{C}^r$  (orange). Equally a level curve at fixed angle  $\varphi$  (yellow) is a copy of action space. A point in phase space may be projected onto either control or action space, see an example in panel (a) pink arrows. (b) Reduced phase space and intrinsic dynamics of paramagnetic colloids for the universal potential in the limit  $Qz > 1$ . The stationary manifolds  $\mathcal{M}_-^r$  and  $\mathcal{M}_+^r$  are depicted in green and red. The intrinsic dynamics is shown as a vector field of generalized velocities with cyan arrows (pointing in positive  $x$ -direction) and blue arrows (pointing in negative  $-x$ -direction). Adiabatic motion of colloidal particles occurs on the stable stationary manifold via the external modulation. (c) At a lower non universal elevation  $Qz = 0.4$ . The topology is still the same as in the universal case. As in all the following cases we choose  $H_{\text{ext}} = M$ . (d) Development of fences in  $\mathcal{M}_-^r$  at  $Qz = 0.34$  and the transition towards topological protected ratchet jumps (yellow) from the fence (border between pink and green color on  $\mathcal{M}^r$ ) toward the pseudo fence (border between green and light green color on  $\mathcal{M}^r$ ) for paramagnetic particles (see Appendix A.3 for a concise definition of fence and pseudo fence). Both fence and pseudo fences on  $\mathcal{M}$  are projected into the same fence points in control space (border between gray and black on the domain wall). Preimages of the gray ( $m = 4$ ) excess line of control space are the two pink and two bright green lines. Preimages of the black ( $m = 2$ ) part of control space are the full red and full green colored lines. (e) Dynamics at an elevation  $Qz = 0.2$ . (f) At  $Qz = 0.1$  fences also start to develop in  $\mathcal{M}_+^r$  causing ratchet jumps for the diamagnets (not shown) and additional feeder ratchet jumps (orange) starting from  $\mathcal{M}_-^r, \text{isolated}$  for the paramagnets. (g) Dynamics at the transition elevation  $Qz = 0.09$  toward a non transporting regime. (h) Phase space and dynamics at low  $Qz = 0.07$  elevation. There are now four disconnected stationary manifolds (two of each kind) which all have zero winding number in action space.

control space. As indicated by the pink arrows in Fig. 3a each point  $(x, \varphi_{\text{ext}})$  can be projected into the copy  $x = 0$  of reduced control space  $(0, \varphi_{\text{ext}}) = P_{C_2^r}(Qx, \varphi_{\text{ext}})$  as well as into the copy  $\varphi_{\text{ext}} = 0$  of action space  $(Qx, 0) = P_A(Qx, \varphi_{\text{ext}})$ .

Fig. 3b–h are plots of the phase space  $C_2^r \otimes \mathcal{A}$  at different elevations  $Qz$  above the pattern and for an external field-strength of  $H_{\text{ext}} = M$ . As we will see in the non-universal case the magnitude of  $H_{\text{ext}}$  matters. The intrinsic dynamics, see eqn (16), is shown as a vector field on the torus. According to eqn (16) the trajectories move along lines of constant external field direction  $\varphi_{\text{ext}}(t_{\text{fixed}}) = \text{const}$ , either in  $Qx$  or  $-Qx$  direction. Regions of phase space with one sense of motion are colored in blue, regions of phase space with opposite sense in cyan. Both regions are separated from each other by the reduced stationary manifold  $\mathcal{M}^r$ , a line consisting of all points for which the potential is stationary  $\partial_x U = 0$ . A stationary point is either a minimum  $(Qx, \varphi_{\text{ext}}) \in \mathcal{M}_+^r$  (red) or a maximum  $(Qx, \varphi_{\text{ext}}) \in \mathcal{M}_-^r$  (green). The intrinsic dynamics of the paramagnetic colloids starts at the red minimum line  $\mathcal{M}_+^r$  and ends at the green maximum line  $\mathcal{M}_-^r$ .

The reduced stationary manifold  $\mathcal{M}^r$  of the universal potential (Fig. 3b) consists of two lines: the line  $\varphi_{\text{ext}} = Qx$  (red) is the set of minima  $\mathcal{M}_+^r$  and the line  $\varphi_{\text{ext}} = Qx + \pi$  (green) is the set of maxima  $\mathcal{M}_-^r$ . Following eqn (17) the adiabatic creeping of the particles has to happen along the stationary manifolds. Paramagnetic colloids will adiabatically follow the green  $\mathcal{M}_-^r$  line while diamagnetic ones will follow  $\mathcal{M}_+^r$  (red). The simplicity of the universal stationary manifold (Fig. 3b) thereby converts any motion in control space into similar motion in action space. If we loop around the control circle we also loop around the action circle and thus induce transport by one unit vector. Both, paramagnetic and diamagnetic particles move at a fixed distance  $\lambda/2$ . A general modulation loop  $\mathcal{L}_C^r$  in reduced control space causes an action loop  $\mathcal{L}_A$  in action space with similar winding number  $w_A = w_C^r$ . The particles can stay on the corresponding manifold during the entire modulation. Therefore the dynamics is completely adiabatic and thus dominated by the external modulation.

When we lower the colloidal plane to  $Qz = 0.4$  the manifold  $\mathcal{M}^r$  deforms (Fig. 3c). Eventually at  $Qz = 0.34$ ,  $\mathcal{M}_-^r$  becomes parallel to the tangent vector of action space  $\mathbf{e}_x$  in one critical point of  $\mathcal{M}_-^r$ . At this critical point  $\partial_x U = \partial_x^2 U = \partial_x^3 U = 0$  and therefore the point is no longer a maximum. As one further lowers  $Qz$  an isolated section  $\mathcal{M}_+^{r,\text{isolated}}$  (pink) interrupts  $\mathcal{M}_-^r$ .

Two fence points  $\mathcal{F}^r = \{(x, \varphi_{\text{ext}}) | \partial_x U = \partial_x^2 U = 0\}$  as common borders between  $\mathcal{M}_+^{r,\text{isolated}}$  (pink) and  $\mathcal{M}_-^r$  (bright green) develop from the formerly closed  $\mathcal{M}_-^r$  loop (Fig. 3d). When a paramagnetic colloid adiabatically creeps along  $\mathcal{M}_-^r$  via the externally induced dynamics and reaches the fence  $\mathcal{F}^r$  it must leave the stationary manifold, follows the intrinsic dynamics and jumps (yellow arrow) toward a new maximum that we call the pseudo fence  $\mathcal{P}\mathcal{F}_-^r$  (border between the bright and full green in Fig. 3e). A pseudo fence is a point on  $\mathcal{M}$  different from the fence that has the same projection onto reduced control space (border between the black and gray line) as the fence but different projections onto action space.

The intrinsic dynamics is irreversible, *i.e.* one can move along the path of steepest descent only in one direction. When we are at the critical elevation the  $\mathcal{M}_+^{r,\text{isolated}}$  interruption has zero length, fence and pseudo fence fall on top of each other. Like this the path of steepest descent has zero length. When we decrease the elevation  $Qz$  the path of steepest descent continuously grows. Although it is no longer on  $\mathcal{M}^r$  it falls into the same homotopy class as the section of  $\mathcal{M}^r$  that it bypasses. That is, both are topologically equivalent and transport by one unit vector can still be achieved by winding around the control space. The dynamics of the colloids, however, undergoes a phase transition from adiabatic toward a ratchet motion.<sup>36–42</sup> The ratchet jumps occur along the path of steepest descent with jump times short compared to the external modulation dynamics. The result of a ratchet transport is the same as the adiabatic motion at higher elevations because of the homotopy between the avoided section of  $\mathcal{M}^r$  and the path of steepest descent. Like this the transport is topologically protected at the adiabatic to ratchet transition.

If we further decrease the elevation to  $Qz = 0.1$  the same thing happens to the other sub-manifold  $\mathcal{M}_+^r$ . It is now interrupted by a  $\mathcal{M}_-^{r,\text{isolated}}$  section resulting in irreversible jumps for the diamagnetic colloids (Fig. 3f). This section also opens up a new possible ratchet jump of paramagnetic particles initially located on  $\mathcal{M}_-^{r,\text{isolated}}$  onto the disconnected other parts of  $\mathcal{M}_-^r$ . The special thing about these feeder jumps is, that once a colloidal particle leaves the isolated section it will never return due to the absence of pseudo fences in  $\mathcal{M}_-^{r,\text{isolated}}$ .

The projection of a point in  $C^r \otimes \mathcal{A}$  onto a point in  $C^r$  defines a mapping from  $\mathcal{M}^r$  onto  $C^r$ . The inverse of this map is not a map because the projection maps several points of  $\mathcal{M}^r$  onto the same point in  $C^r$ . We call the number of preimages of the projection on  $\mathcal{M}^r$  the multiplicity. Note that, the two (bright green) sections between pseudo fence and fence, the (pink)  $\mathcal{M}_+^{r,\text{isolated}}$  insertion as well as a non isolated section (pink) of  $\mathcal{M}_+^r$  are projected onto the same (gray) excess segment of control space. Consequently the (gray) excess segment has multiplicity  $m = 4$  (it has four preimages on the manifold  $\mathcal{M}^r$ ). The rest of  $\mathcal{M}^r$  is projected twice on the remaining (black, multiplicity  $m = 2$ ) section of  $C_2^r$ . Like this there are sections of control space with different multiplicity. When we move from the  $m = 2$ -region of control space to the  $m = 4$  region a maximum minimum pair is created in  $\mathcal{M}^r$ .

The topology of  $\mathcal{M}^r$  does not change at the adiabatic to ratchet transition. It is only the distribution of points on  $\mathcal{M}^r$  into the subsets  $\mathcal{M}_-^r$  and  $\mathcal{M}_+^r$  that changes. A transition of the topology of  $\mathcal{M}^r$  occurs at  $Qz = 0.09$  when the formerly disconnected parts of  $\mathcal{M}^r$  touch each other in four fence points (Fig. 3g) and then separate into four disconnected parts (Fig. 3h). Two of the new disconnected parts after the disjoining are entirely of type  $\mathcal{M}_-^r$  and two are of type  $\mathcal{M}_+^r$ . The  $\mathcal{M}_-^r$  parts are localized near the domain walls, while the  $\mathcal{M}_+^r$  parts lie on top of a domain. All four parts of  $\mathcal{M}^r$  have non vanishing winding number around the reduced control space but vanishing winding numbers around action space. Any control loop will thus only

create periodic motion in action space that is associated with no net transport over a period.

We have given a description of the dynamics of paramagnets. The dynamics of diamagnets is the reversed intrinsic dynamics coupled with the external dynamics on  $\mathcal{M}_+^r$ . For the universal case at high elevations both types of particles move exactly the same way however they are separated by half the wavelength  $\Delta Qx = \pi$  of the pattern. At lower elevation the transitions to a ratchet motion occurs for different elevations  $Qz = 0.34$  (Fig. 3d) for the paramagnets and  $Qz = 0.1$  (Fig. 3f) for the diamagnets. The transition from transport to no transport happens for both particles simultaneously at an elevation of  $Qz = 0.09$  (Fig. 3g). Paramagnets are then confined to the domain walls and diamagnets to the domains.

### 3.2 Experiments

We have performed experiments with paramagnetic colloids above the stripe pattern of wavelength  $\lambda = 7.2 \mu\text{m}$ , and magnetization  $M \approx 20 \text{ kA m}^{-1}$  of a magnetic garnet film.<sup>43,44</sup> We covered the garnet film with a ferrofluid of defined thickness  $d$ . Magnetic levitation lifts the colloids to the mid plane of the film at a fixed elevation  $z$ . Since we were limited in the variation of the thickness  $d$  we used the amplitude  $H_{\text{ext}}$  of the external field as a second control parameter. Both, decreasing the field or decreasing the elevation renders the transport behavior non-universal. The modulation of the external magnetic field that drove the dynamics was generated by three coils arranged along the  $x$ ,  $y$ , and  $z$  axes.<sup>31</sup> We applied a palindrome modulation loop  $\mathcal{L}_{cr} = \tilde{\mathcal{L}}_{cr} \tilde{\mathcal{L}}_{cr}^{-1}$ , i.e. a combination of a forward loop  $\tilde{\mathcal{L}}_{cr}$  of winding number  $w(\tilde{\mathcal{L}}_{cr}) = 1$  followed by the time reversed backward loop  $\tilde{\mathcal{L}}_{cr}^{-1}$  with winding number  $w(\tilde{\mathcal{L}}_{cr}^{-1}) = -1$ , each subloop has a duration of  $\Delta t = 5 \text{ s}$ .

We measured the corresponding trajectories in reduced phase space  $\mathcal{C}_2^r \otimes \mathcal{A}$  at different heights. By video tracking we obtained the coordinate  $x_{\mathcal{A}}(t)$  of the trajectory in action space. Simultaneously we determine  $\varphi_{\text{ext}}(t)$  by measuring the width of an up magnetized stripe that periodically varies with the external field and is visualized in the same video (see ref. 45) *via* the polar Faraday effect.

At the universal elevation (Fig. 4a) the colloids creep adiabatically along the stationary manifold  $\mathcal{M}_-^r$ . Forward (green) and backward (olive) trajectories fall almost on top of each other. If we lower the elevation we can observe ratchet motion (Fig. 4b). There we can identify the sections of the trajectories that lie on  $\mathcal{M}_-^r$  as those where the speed of the colloids on the trajectories is slow (adiabatic) (see green data in Fig. 4b). The paths of steepest descent are the regions where the velocity is high (intrinsic dynamics). In the forward loop the adiabatic motion passes the pseudo fence and the particle jumps when it reaches the fence. The path of steepest descent reunites with the backward trajectory at the pseudo fence. The two sections on  $\mathcal{M}_-^r$  between fence and pseudo fence together with the paths of steepest descent connecting fence and pseudo fence define the hysteresis between forward and backward ratchet loops. A fully adiabatic motion has negligible hysteresis.

At even lower elevations, below the topological transition height, we no longer observe transport. The paramagnetic particles are attached to the domain walls (Fig. 4c).

In a ratchet motion the path of steepest descent, and therefore the hysteresis, develops continuously from the critical point. The winding number  $w(\tilde{\mathcal{L}}_{\mathcal{A}}) = -w(\tilde{\mathcal{L}}_{\mathcal{A}}^{-1})$  of the forward loop does not change across this continuous transition. In contrast, the topological transition towards the non transporting regime is discontinuous.

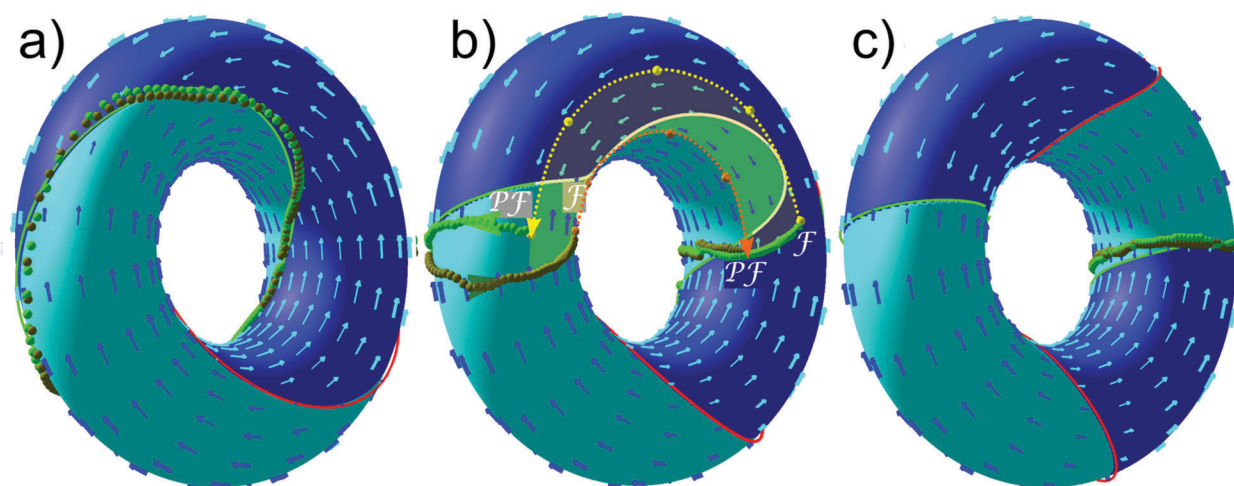


**Fig. 4** Reduced phase space (torus), intrinsic dynamics (vector field), stationary manifolds (green and red solid lines), and experimental trajectories (green, olive, yellow and orange) for three different non-universal elevations. (a) Adiabatic motion in a nearly universal potential  $Qz = 4.34$ ,  $H_{\text{ext}} = 0.2M$ . (b) Ratchet motion at an elevation  $Qz = 0.43$ ,  $H_{\text{ext}} = 0.2M$ . (c) No motion at a elevation  $Qz = 0.43$ ,  $H_{\text{ext}} = 0.1M$  below the topological transition. Experimentally measured data for a forward (backward) modulation loop with  $w_c = 1(-1)$  is shown as green (olive) spheres for adiabatic, i.e. slow, motion and in yellow (orange) for the fast ratchet jumps. The ratchet motion in (b) exhibits hysteresis between forward and backward motion (yellow shaded area). The experimental data does not perfectly match the theory (solid green line) since the changes of the stripe pattern of the garnet film with the external field (relevant at non-universal elevation) have not been included into the theory. Both experimental data and theory however fall into the same homotopy class. A video clip of the adiabatic motion of the paramagnetic colloidal particle in (a) is provided in ref. 45.

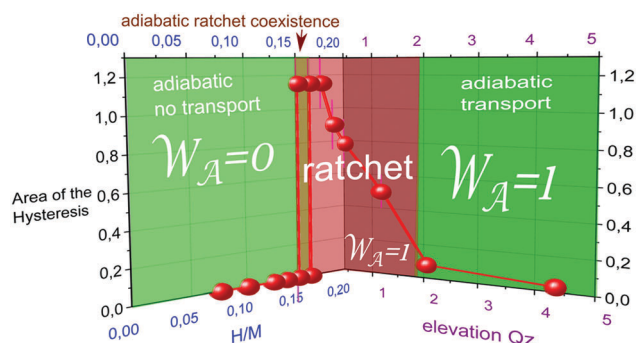


Fig. 5 Experimentally measured area of the hysteresis of the transport. The area of the hysteresis is measured on the surface of the torus  $\mathcal{C}_2^r \otimes \mathcal{A}$ . The total area of a torus is  $(2\pi)^2 \approx 40$ . On the right we lowered the elevation  $Qz$ . This reveals the continuous transition from adiabatic transport toward ratchet motion. On the left side we decrease the external field amplitude at constant elevation. This reveals the discontinuous topological transition towards no transport.

In Fig. 5 we plot the area of the hysteresis *versus* the non-universality parameters (external field  $H_{\text{ext}}$  and elevation  $Qz$ ). Both the continuous adiabatic toward ratchet transition as well as the discontinuous ratchet to adiabatic non-transport transition can be clearly identified from the figure.

### 3.3 Constrained control space

In Section 4 we will discuss the universal potential of a four-fold symmetric pattern. It is useful to first reiterate the universal case of the two-fold symmetric problem, using full control space  $\mathcal{C}$ .

In the Section 3.2 we reduced the control space of the stripe system to fields that are lying in the plane spanned by the normal vector  $\mathbf{n}$  to the pattern and by the unique reciprocal unit vector  $\mathbf{Q}$ . We just dropped the physically possible external field component along the indifferent  $\pm\mathbf{n} \times \mathbf{Q}$  direction. Here we do not ignore this component. Hence, since the magnitude of the external field  $H_{\text{ext}}$  does not play a role for the universal case, full control space is a sphere. The constrained control space  $\tilde{\mathcal{C}}_2$  of the stripe pattern is a two punctured sphere. The two points along the  $\pm\mathbf{n} \times \mathbf{Q}$  direction are removed from the sphere of the full control space  $\mathcal{C}$  since these points produce an indifferent constant potential in action space.

Topologically, the two punctured sphere  $\tilde{\mathcal{C}}_2$  and the circle  $\mathcal{C}_2^r$  are equivalent. Since only the topology of control space is important we may expand  $\mathcal{C}_2^r$  to the constrained control space  $\tilde{\mathcal{C}}_2$ . Note that the winding number of a modulation loop in  $\mathcal{C}_2^r$  becomes the winding number of a modulation loop around the indifferent  $\pm\mathbf{n} \times \mathbf{Q}$  axis through the two removed points of the punctured sphere in  $\tilde{\mathcal{C}}_2$ . The reduced control space is just the grand circle on the sphere around this axis. We can predict the result of modulation loops in the constrained control space  $\tilde{\mathcal{C}}_2$ : winding around the punctured points induces transport in action space.

To make the connection to the topologically trivial full control spaces of lattices with higher point symmetries, we can

reinsert the removed points into the punctured sphere  $\tilde{\mathcal{C}}_2$ . That is, we recover the topologically trivial full control space  $\mathcal{C}$  allowing fields pointing into the indifferent direction. This enables us to continuously deform a modulation loop with one winding number around the axis into a modulation loop with different winding number. The transition in winding number occurs when the modulation loop passes through the reinserted point.

Note that the indifferent direction satisfies

$$\nabla_{\mathcal{A}} U^* = 0, \quad (18)$$

and

$$\det(\nabla_{\mathcal{A}} \nabla_{\mathcal{A}} U^*) = 0, \quad (19)$$

for any point  $\mathbf{x}_{\mathcal{A}} \in \mathcal{A}$ . We call points in  $\mathcal{C} \otimes \mathcal{A}$  that fulfill eqn (18) and (19) the fences  $\mathcal{F}$  on  $\mathcal{M}$ . For the stripe pattern and the universal case fence points only exist in  $\mathcal{C} \otimes \mathcal{A}$ , not in  $\mathcal{C}_1^r \otimes \mathcal{A}$ . In the stationary manifold of the reduced control space  $\mathcal{M}^r$  the sub-manifolds are two disconnected lines (maximum and minimum) without fences (Fig. 3b). On the full stationary manifold  $\mathcal{M}$  the fence consists of two copies (one for each of the opposite indifferent points in  $\mathcal{C}$ ) of the one dimensional action space and thus consists of two disconnected circles.

The fences separate the maxima of the stationary manifold from the minima (Fig. 6). Hence using the constrained control space the stationary manifold  $\mathcal{M}$  is a two dimensional manifold that is not disconnected.  $\mathcal{M}_-$  and  $\mathcal{M}_+$  are both copies of the punctured sphere, with the puncture point enlarged to a circular fence and there joined to one closed surface. Fig. 6 shows the topology of the universal stationary manifold  $\mathcal{M}$  for the full control space.  $\mathcal{M}_+$  is depicted in red and  $\mathcal{M}_-$  in green.

The constrained control space  $\tilde{\mathcal{C}}_2$  can be subdivided into two hemispheres, the northern hemisphere for which  $H_{\text{ext},z} > 0$  and the southern hemisphere ( $H_{\text{ext},z} < 0$ ). Both hemispheres are simply connected areas, *i.e.* areas where every loop is zero

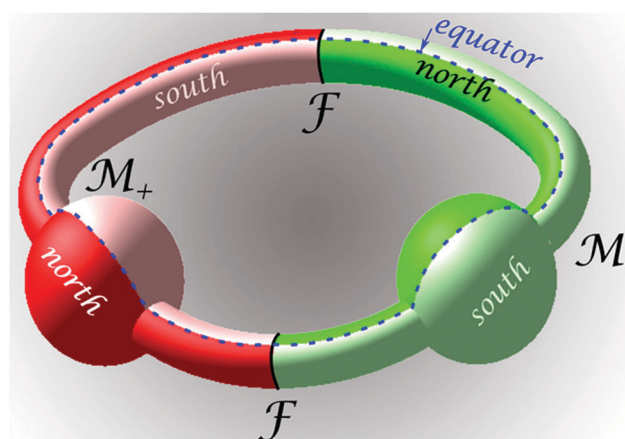


Fig. 6 The stationary manifold for the universal potential of the stripe pattern for the full control space  $\mathcal{C}$ .  $\mathcal{M}_+$  is depicted in red and  $\mathcal{M}_-$  in green. Both are connected by two circular fences  $\mathcal{F}$ . Copies of the northern hemispheres of  $\mathcal{C}$  are shown in full colors, while the southern ones are shown in light colors. (See Appendix A.3 for a concise definition of the hemispheres and the equator.)

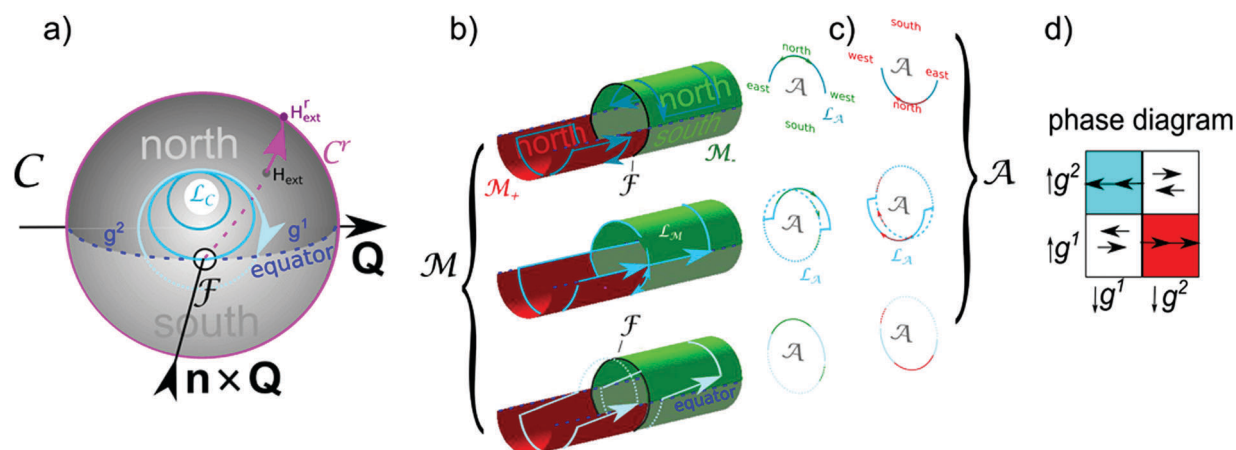


Fig. 7 (a) Full control space of the stripe pattern. (b) Section of the stationary manifold  $\mathcal{M}$  and (c) its projection into action space. Several modulation loops  $\mathcal{L}_C$  in  $\mathcal{C}$  and their preimages  $\mathcal{L}_M$  on  $\mathcal{M}$  and the further projections  $\mathcal{L}_A$  into  $\mathcal{A}$  are shown. In (a) the reduced control space is shown in pink together with a projection of a full external field  $\mathbf{H}_{\text{ext}}$  into the reduced external field  $\mathbf{H}_{\text{ext}}^r$  is also shown. (d) Phase diagram of the transport modes for the fundamental loops  $\mathcal{L}_C = \downarrow g^i \uparrow g^j$ . Colored squares indicate transport, white squares indicate no transport.

homotopic. The areas are glued together at the two sections  $g^1$  and  $g^2$  of the equator between the puncture points. In Fig. 6 we show the simply connected areas of the stationary manifold that are projected into both hemispheres of  $\tilde{\mathcal{C}}_2$ .

Two lines circle the stationary manifold, see Fig. 6. We call these lines the equator since they are projected onto the equator of  $\tilde{\mathcal{C}}_2$ , see Fig. 7a. When the equator hits the puncture point in  $\tilde{\mathcal{C}}_2$  the two equators of the stationary manifold cross the fences in  $\mathcal{M}$ . Topologically  $\mathcal{M}$  is a genus one surface with two winding numbers. The winding numbers of the fences are different from the winding numbers of the equator.

Fig. 7 shows the topological transition of the transport modes on  $\mathcal{M}$  and  $\mathcal{A}$  due to the continuous deformation of a control loop in  $\mathcal{C}$ . We start with a control loop (dark blue loop) that is entirely in the north and hence does not wind around the indifferent point. The loop has two preimages on  $\mathcal{M}$ , one on  $\mathcal{M}_-$  and one on  $\mathcal{M}_+$ . Both are zero homotopic. Now we further deform the modulation loop such that it crosses the fence point (blue loop). The preimage on  $\mathcal{M}$  is the union of the two formerly disconnected loops and the fence itself. Mathematically the preimage is not a loop but a lemniscate.<sup>46</sup> When we slightly enlarge the loop (cyan), such that it is now winding around the fence point in  $\mathcal{C}$ , the lemniscate on  $\mathcal{M}$  disjoins again into two loops on  $\mathcal{M}_-$  and  $\mathcal{M}_+$ . Now, both loops have non vanishing winding numbers. The projection of the loop in  $\mathcal{M}_-$  ( $\mathcal{M}_+$ ) corresponds to a maximum (minimum) of the potential in  $\mathcal{A}$  that adiabatically moves around with a winding number similar to the winding number around the indifferent axis in  $\mathcal{C}$ ,  $w_A = w_C$ .

We now understand how to produce a topological transition of the transport modes by continuously deforming the loop in control space. The transport direction in action space is topologically protected for any deformation of the modulation loop that does not alter the winding number around the fence points. A topological transition occurs when we move the loop across one of the fence points.

We can characterize the simplest modulation loops by the two segments of the equator that they cross. We define  $\downarrow g^i$ ,  $i = 1, 2$  as a south traveling path that passes the equator segment  $g^i$  between the two fence points. We complete the loop with an analogous north traveling path,  $\uparrow g^j$ . In Fig. 7d we depict a phase diagram of the transport for the fundamental loops  $\mathcal{L}_C = \downarrow g^i \uparrow g^j$ . Modulation loops that do not cross the equator, as well as those passing the same equator segment south and north, cause no transport. Modulation loops passing one segment south and the other one north induce transport.

## 4 Four fold symmetry

In ref. 21 we study in detail theoretically and with computer simulations four-fold symmetric patterns. Here we summarize the theoretical results, present experimental data, and show the connection to the two-fold symmetric system.

### 4.1 Theory

The four-fold symmetric magnetic potential

$$\psi_4(z, x, y) = \psi_2(z, x) + \psi_2(z, y) \quad (20)$$

is closely related to the two-fold symmetric potential  $\psi_2$ , where  $\mathbf{e}_x$  points along  $\mathbf{Q}_1$  and  $\mathbf{e}_y$  points along  $\mathbf{Q}_2$ . Action space  $\mathcal{A}_4 = \mathcal{A}_2 \otimes \mathcal{A}_2$  is the product space of two circles and thus a torus with both  $Qx$  and  $Qy$  varying from 0 to  $2\pi$ . There is no indifferent direction and hence it is simpler to use full control space  $\mathcal{C}$ . However there exist fence-points satisfying eqn (18) and (19). These fence points play the same role as in  $N = 2$ -case in generating transport.

The universal scalar magnetic potential is the superposition of two stripe potentials that separate the variables  $x$  and  $y$  in action space. Therefore, we have four fence points on the equator of the control space sitting in the  $\pm \mathbf{e}_x$  and  $\pm \mathbf{e}_y$  directions (Fig. 8a).

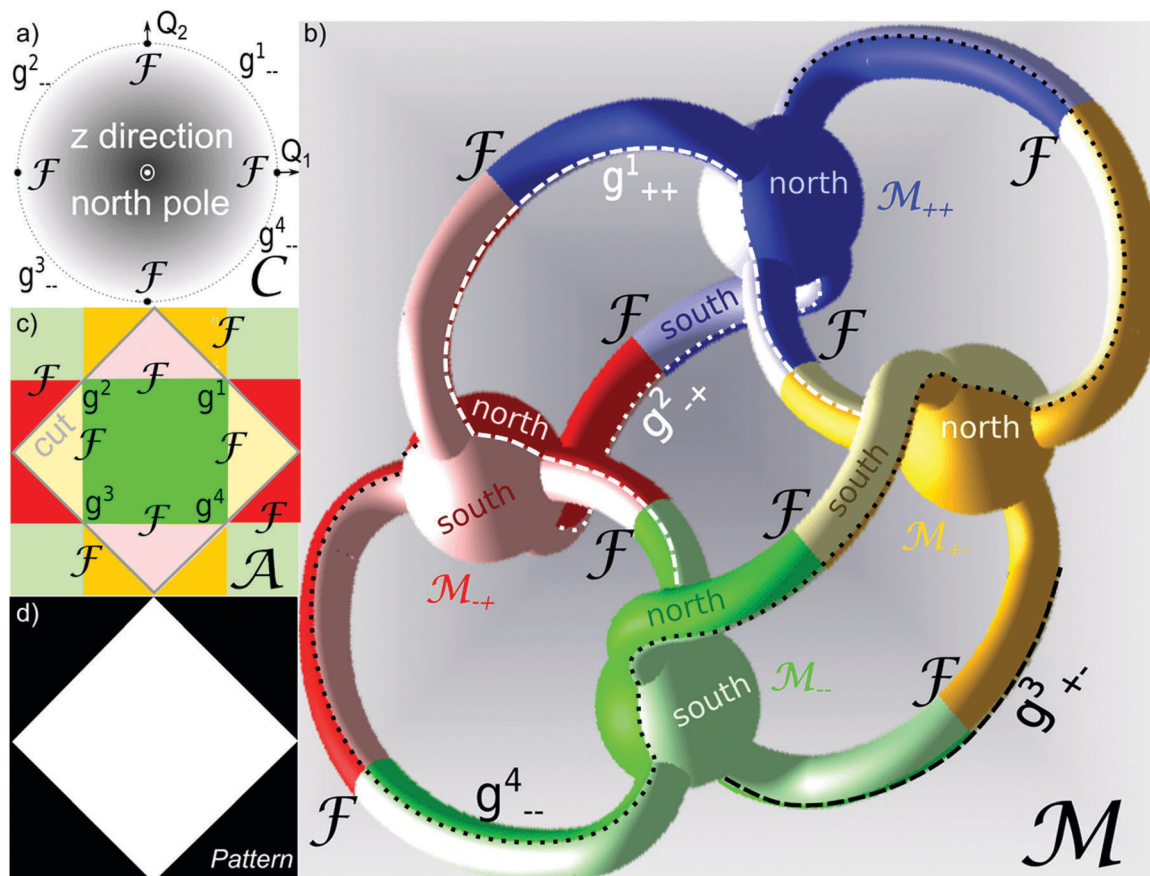


Fig. 8 (a) Top view of the four-fold symmetric control space including the fence points and the maximum segments  $g^i_{\pm}$ ,  $i = 1, 2, 3, 4$  of the four gates. (b) Genus five stationary manifold  $\mathcal{M}$ . Blue colors correspond to minima ( $\mathcal{M}_{++}$ ), green to maxima ( $\mathcal{M}_{--}$ ), red and yellow to saddle points. (c) Projection of the half of  $\mathcal{M}$  lying closer to  $\mathcal{M}_{--}$  into action space. The cut in  $\mathcal{A}$  is the projection of the points in  $\mathcal{M}$  separating both halves. (d) Magnetic pattern generating the four-fold symmetric universal potential. (see Appendix A.3 for a concise definition of the gates).

We define the unit vectors

$$\mathbf{e}_1(\mathbf{x}_A) = \frac{\partial_1 \mathbf{H}^P}{|\partial_1 \mathbf{H}^P|}, \quad \mathbf{e}_2(\mathbf{x}_A) = \frac{\partial_2 \mathbf{H}^P}{|\partial_2 \mathbf{H}^P|}, \quad (21)$$

where  $\partial_{1,2}$  denote the partial derivatives with respect to the two coordinates in  $\mathcal{A}$ . Points in  $\mathcal{A}$  with  $\mathbf{e}_1 \times \mathbf{e}_2 \neq 0$  are made stationary by two opposite external fields<sup>20,21</sup>

$$\mathbf{H}_{\text{ext}}^{(s)} = \pm \frac{\mathbf{e}_1 \times \mathbf{e}_2}{|\mathbf{e}_1 \times \mathbf{e}_2|}. \quad (22)$$

The two signs in (22) cause opposite curvature of  $U^*$  and thus each point in  $\mathcal{A}$  can be made either an extremum (maximum or minimum) or a saddle point. Hence, we can split action space into forbidden and accessible regions (see Fig. 8c). Allowed regions are regions of extrema and they are colored green, while forbidden regions are regions of saddle points and are colored red and yellow.

Each field in control space renders 4 points in action space stationary, a maximum a minimum and two saddle-points. Hence our stationary manifold consists of four copies of control space (instead of two for the case  $N = 2$ ). The indices of the four sub-manifolds  $\mathcal{M}_{++}$ ,  $\mathcal{M}_{+-}$ ,  $\mathcal{M}_{-+}$ , and  $\mathcal{M}_{--}$  correspond to a minimum (index +) or a maximum (index -) along the

$x$  (first index) and  $y$  (second index) coordinates. The four fence points in control space deform into circular fences in  $\mathcal{M}$ . The four sub-manifolds are glued together at eight fences to form the full stationary manifold, see Fig. 8b. The stationary manifold is a genus five surface.

The fences in  $\mathcal{M}$  are projected onto lines in action space that are the borders between the forbidden and allowed regions. The fences do not intersect on  $\mathcal{M}$  but they do in  $\mathcal{A}$ . This is possible because the fences meet at special points in  $\mathcal{A}$  with  $\mathbf{e}_1 \times \mathbf{e}_2 = 0$ , that we call the gates. As we will show below, the gates are the only points that connect two consecutive allowed regions. From eqn (7), (21) and (22) we conclude that the gates are rendered stationary by the whole grand circle on  $\mathcal{C}$  around  $\mathbf{e}_1 = \mathbf{e}_2$ . For the four-fold symmetric pattern there are four coinciding gates  $g^i$ ,  $i = 1, 2, 3, 4$  in  $\mathcal{C}$  that run across the equator right through the four fence points, see Fig. 8a. In  $\mathcal{C} \otimes \mathcal{A}$  each gate is a line on  $\mathcal{M}$  that lies in a single copy of the equator of control space and that is projected into the gate in  $\mathcal{A}$ . Since one gate in  $\mathcal{C}$  cuts through all four fences the gate in  $\mathcal{A}$  must be the same as the intersection of fences in  $\mathcal{A}$ .

In  $\mathcal{C}$  the fence points cut each gate into 4 segments  $g^i_{++}$ ,  $g^i_{+-}$ ,  $g^i_{-+}$ ,  $g^i_{--}$ , that are projections of the gates in the corresponding sub-manifolds of  $\mathcal{M}$ . Each gate crosses four of the eight fences

in  $\mathcal{M}$  and passes over all four sub-manifolds. Each fence crosses two of the four gates. The gate  $g_{\alpha\beta}^{i+1}$  in  $\mathcal{C}$  coincides with the gate  $g_{\alpha\beta}^i$  rotated by  $\pi/2$ . Therefore the maximum segments of the gates  $g_{-}^i$ ,  $i = 1, 2, 3, 4$  fill the whole equator and subdivide  $\mathcal{C}$  as well as all sub-manifolds  $\mathcal{M}_{\alpha,\beta}$  and their projections on  $\mathcal{A}$  into simply connected northern and southern hemispheres. Northern and southern allowed regions touch each other in  $\mathcal{A}$  only at the gates. Nontrivial adiabatic transport therefore must pass these singular points.

In the following we will first deal with the transport of paramagnetic particles. Since these reside on the maxima of  $U^*$ , we are only interested in loops on  $\mathcal{M}_{--}$ . Modulation loops that remain in one hemisphere of control space are zero homotopic loops of the four punctured sphere and have zero homotopic preimage loops on  $\mathcal{M}$ . The simplest non trivial modulation loop must cross the equator twice. Such loop  $\mathcal{L}_C = \downarrow g^i \uparrow g^j$  consists of two paths  $\downarrow g^i$  and  $\uparrow g^j$ .  $\downarrow g^i$  is a path from north to south passing the gate  $g_{-}^i$  and  $\uparrow g^j$  is the reverse path passing through gate  $g_{-}^j$  from south to north. The winding numbers in control space around the fences cause similar winding in action space. Fig. 9 shows the phase diagram of the transport directions of the simplest gate crossing modulation loops. The topological transition between different transport

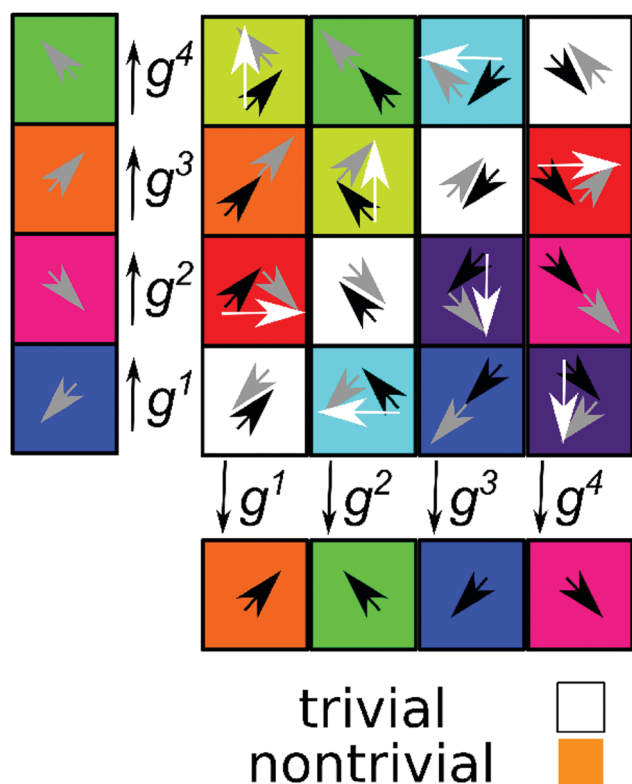


**Fig. 9** Phase diagram of the transport modes in a four-fold symmetric system. Black arrows denote the traveling direction in the first, south heading part of the modulation, gray ones describe the transport direction of the second part, and white arrows describe the travel direction of the full loop. The colors of the squares indicate the traveling direction. Loops passing through the same gate twice do not induce transport (white). All other combinations induce transport in one of the eight neighboring unit cells.

modes is similar to the two-fold case. Modulation loops passing a fence cause topological transitions.

Diamagnetic particles move synchronously with the paramagnetic ones at a fixed distance  $\mathbf{d} = 1/2(\mathbf{a}_1 + \mathbf{a}_2)$ , to the paramagnets.

## 4.2 Experiments

Four fold symmetric patterns have been created by lithography.<sup>47–50</sup> The lithographic magnetic patterns are designed to have the four-fold symmetric pattern of Fig. 2b with a period  $a = 7 \mu\text{m}$ . The strength of the pattern field directly on top of the surface of the thin  $Qt < 1$  lithographic film is  $H^p \approx 3 \text{ kA m}^{-1}$ . Details on the production process are given in the Appendix A.2.

Lithographic edge effects of the pattern production process render white regions larger than the black regions such that the average magnetization of the film is non-zero. This breaks the  $S_4$ -symmetry of the pattern, but it does not affect the  $S_4$ -symmetry of the universal limit  $Qz > 1$  and the  $C_4$  symmetry is preserved for the pattern and the universal limit. We coat the patterned magnetic film with a photo-resist of thickness  $1.6 \mu\text{m}$ . The thickness is a compromise of achieving universality and keeping the magnetic field of the pattern sufficiently strong. Paramagnetic colloids (diameter  $d = 2.7 \mu\text{m}$ ) immersed into deionized water are placed on top of the coating.

In Fig. 10a we apply fundamental modulation loops. They all fall in the class  $\mathcal{L}_C = \downarrow g^i \uparrow g^j$ , but have different proximity to the fence point in the  $\mathbf{Q}_1$  direction in  $\mathcal{C}$ . In Fig. 10b we plot the corresponding experimental trajectories of paramagnetic particles. No matter which particular modulation loop within the same homotopy class we choose, the global result after completing the loop is the transport of the particle by one unit vector  $\mathbf{a}_2$ . Modulation loops closer to the encircled fence point

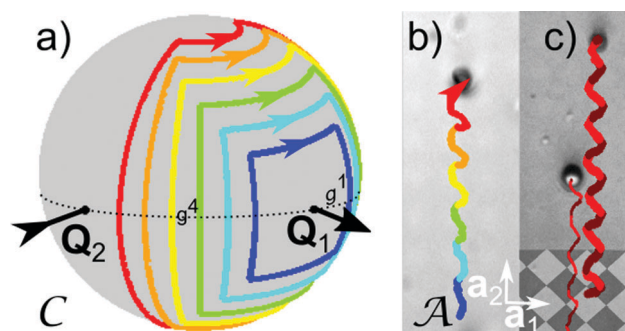


**Fig. 10** (a) various modulation loops in control space of the type  $\mathcal{L}_C = \downarrow g^i \uparrow g^j$ . (b) Resulting trajectories of paramagnetic colloids. All modulation loops induce transport into the same  $\mathbf{a}_2$ -direction. (c) Trajectories of a paramagnetic (thick line) and a diamagnetic colloid (thin line) subjected to the large (red) modulation loop. Trajectories are colored in dark red for the  $\downarrow g^i$  segment and in bright red for the  $\uparrow g^j$  segment of the loop. Both types of particles are synchronously transported into the same direction. The trajectories however are shifted by  $\mathbf{d} = 1/2(\mathbf{a}_1 + \mathbf{a}_2)$ . The background in (b and c) are reflection microscopy images of the four-fold symmetric pattern. We have added the theoretical pattern to the lower part of (c) for clarity. The length of the arrows indicating the lattice vectors is equivalent to the lattice constant  $a = 7 \mu\text{m}$ . A video clip of the motion of the paramagnetic and the diamagnetic colloidal particle in (c) is provided in ref. 45.

have a straighter trajectory than loops passing the equator far from it (see Fig. 10b).

In Fig. 10c we repeat the experiment with paramagnetic and diamagnetic colloids using the largest modulation loop (red). We immerse paramagnetic and non magnetic (polystyrene  $d = 4 \mu\text{m}$ , susceptibility  $\sim -10^{-5}$ ) particles in ferrofluid which renders the non magnetic particles effectively diamagnetic. The direction of the magnetic field inside the ferrofluid is used for the direction in control space. It has a higher tilt angle to the film normal than the tilt of the external field applied by the coils, because of refraction at the glass ferrofluid interface. All loops with colloids immersed in ferrofluids are corrected for this effect. Both particles are transported in  $\mathbf{a}_2$  direction by the red loop and the predicted shift of both trajectories by  $1/2(\mathbf{a}_1 + \mathbf{a}_2)$  is clearly visible.

In Fig. 11 we show the motion of a paramagnetic particle subject to a modulation poly-loop that consists of all sixteen fundamental loops  $\downarrow g^i \uparrow g^j$  of the phase diagram of Fig. 9. We plot the fundamental sections of the trajectory of the particles

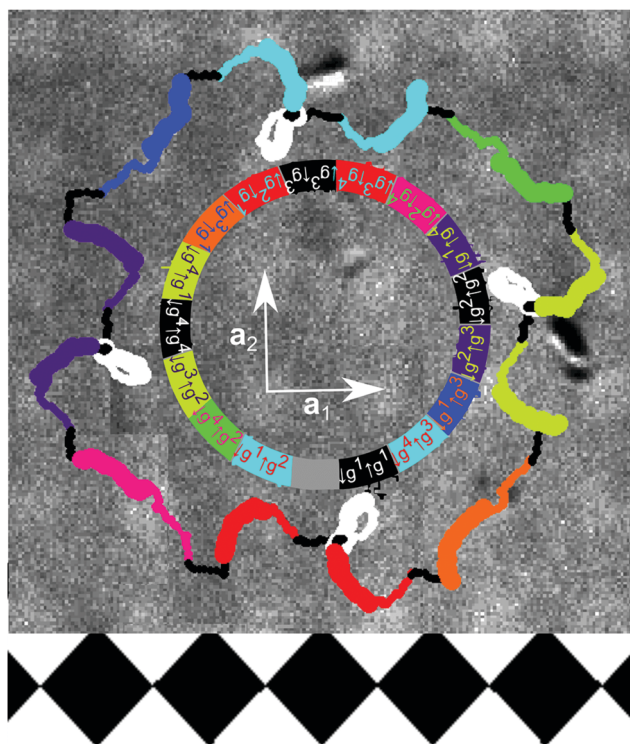


**Fig. 11** Experimental trajectory of a paramagnetic colloidal particle in action space  $\mathcal{A}$  caused by a modulation poly-loop in  $\mathcal{C}$ . The poly-loop consists of a sequence of all fundamental modulation loops in the phase diagram of Fig. 9. The single fundamental loops are colored according to the color in the phase diagram in Fig. 9. South traveling segments are marked as thick lines while north traveling segments are marked as thin lines. Consecutive loops are connected by trivial constant latitude connections that remain in the north of  $\mathcal{C}$  (black trajectories). The type of the single loops is indicated inside the region surrounded by the trajectory. The background is the reflection microscopy image of the underlying square magnetic pattern. At the bottom we show a scheme of the theoretical pattern aligned and oriented to the weakly visible experimental pattern on the top. A video clip of the motion of the paramagnetic colloidal particle is provided in ref. 45.

in the colors of the corresponding fundamental loops in the phase diagram (Fig. 9). It can easily be seen that all fundamental loops induce the theoretically predicted transport. Due to the lack of  $S_4$ -symmetry the lemniscates of the zero homotopic loops in  $\mathcal{A}$  (white) lose their inversion symmetry with respect to the gate in  $\mathcal{A}$  (the crossing point of the lemniscate) resulting in a big and a tiny white loop. We conclude that the experimental response of the particles to all modulation loops is in perfect agreement with the theoretical predictions.

## 5 Three-fold symmetry

In ref. 20 we studied the motion on a  $C_6$ -symmetric pattern theoretically and provided experiments of the adiabatic motion on this pattern. The  $C_6$ -symmetric pattern is part of the family of three-fold symmetric patterns. Here, we extend the theory to this entire family, explain a new topological transition within the family and corroborate the theory with experiments on adiabatic and ratchet transport for all family members. We also confirm experimentally the new topological transition from  $C_6$ -like toward  $S_6$ -like topology.

### 5.1 Control space, stationary manifold and action space

The transport on the three-fold symmetric pattern is more complex than on the two-fold and four-fold patterns. The increased complexity is related to the fact that the three reciprocal lattice vectors  $\mathbf{Q}_1$ ,  $\mathbf{Q}_2$  and  $\mathbf{Q}_3$  are linearly dependent. In Fig. 12 we show the control spaces, the stationary manifolds, and the action spaces of the three-fold symmetric system for various values of the phase  $\phi$  of the pattern. The phase  $\phi$  varies in an interval  $0 \leq \phi \leq \pi/6$  which covers all possible three-fold symmetries including  $C_6$  ( $\phi = 0$ ) and  $S_6$  ( $\phi = \pi/6$ ). We call the range  $\pi/9 < \phi \leq \pi/6$  the  $S_6$ -like case and the range  $0 \leq \phi < \pi/9$  the  $C_6$ -like case. The range  $\pi/6 < \phi < 2\pi$  repeats those patterns, however, centered around one of the other two three-fold symmetric points and/or interchanging up and down magnetized regions, see Fig. 2c. For each value of the phase  $\phi$  of the pattern the stationary manifold  $\mathcal{M}$  in Fig. 12 is a genus seven surface. As in the two and four-fold cases there are fences of  $\mathcal{M}$  separating different sub-manifolds. We distinguish two different fences: (i) the maximum fence  $\mathcal{F}_- = \mathcal{M}_- \cap \mathcal{M}_0$ , which is the border between the regions of maxima of the colloidal potential (green colors) and the saddle point regions (red colors), and (ii) the minimum fence  $\mathcal{F}_+ = \mathcal{M}_+ \cap \mathcal{M}_0$ , which is the border between saddle points and minima (blue colors).

Due to the separability of the two-fold and four-fold problem the fences were projected onto single points in control space. For  $N = 3$  the fences in control space  $\mathcal{C}$  are not points but closed lines. In Fig. 12a the maximum fences  $\mathcal{F}_-$  are shown as green lines and the minimum fences  $\mathcal{F}_+$  as blue lines in control space. The fences in  $\mathcal{C}$  separate regions of different multiplicity of preimages in  $\mathcal{M}$ . For any value of  $\phi$  there is one multiply connected area (gray) that we call the tropics. This area has multiplicity  $m = 4$ , that is, one external field renders 4 points in action space  $\mathcal{A}$  stationary: one maximum, one minimum and

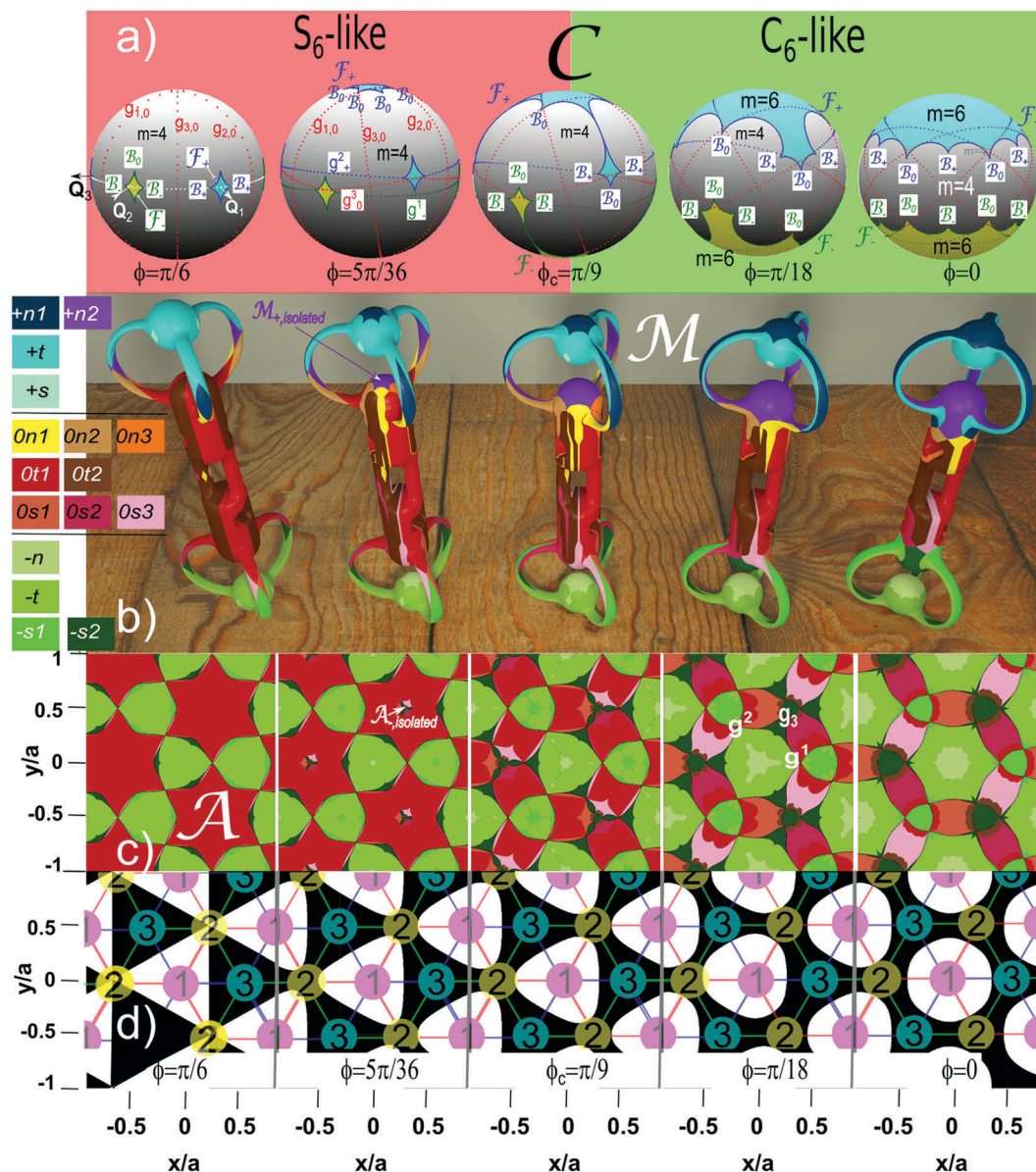


**Fig. 12** Topology of the three-fold symmetric case as a function of the phase  $\phi$ : (a) control spaces with areas of different multiplicity  $m = 4$  (gray),  $m = 6$  extra maximum areas (yellow) which are surrounded by the southern fence  $\mathcal{F}_-$  (green lines) and  $m = 6$  extra minimum areas (cyan) surrounded by the northern fence  $\mathcal{F}_+$  (blue lines). The gates  $g$  are colored according to their segments. (b) Genus seven stationary manifolds  $\mathcal{M}$ . Blue colors correspond to minima ( $M_+$ ), red colors to saddle points ( $M_0$ ) and green colors to maxima ( $M_-$ ). Fences are the boundaries between the color families and pseudo fences are the boundaries between the colors of one family. Areas with labeled with a prefix (n) are projected into the northern area or the northern satellites in  $\mathcal{C}$ , with a prefix (s) to the south, with a prefix (t) to the tropical  $m = 4$  area of  $\mathcal{C}$ . (c) Projection of the lower half of the stationary manifold into action space  $\mathcal{A}$ . The projection of the upper half exactly matches the lower projection, however, with the colors of the upper half replacing those of the lower half. The areas  $0t1$  and  $0t2$  contain cuts (not shown) that connect the shown projection of the southern half of  $\mathcal{M}_0$  to its similar twin projection of the northern half. (d) Magnetic patterns corresponding to the different phases. Up magnetized regions shown in white and down magnetized regions in black. The pink, yellow and cyan circles mark the three high symmetry points of the lattice and the high symmetry lines connecting the points form the 12-, 23-, and 31-network. Higher resolution images of  $\mathcal{A}$ ,  $\mathcal{C}$ , and  $\mathcal{M}$  for each of the phases with further details can be found in the Appendix A.1, definitions of the various geometrical objects in Appendix A.3.

two saddle points. In addition there are concave excess regions of multiplicity  $m = 6$ . In the yellow regions surrounded by  $\mathcal{F}_-$  there is an extra maximum and an extra saddle point, while in the cyan regions (surrounded by  $\mathcal{F}_+$ ) there is an additional minimum and also a saddle point. The control space always shows the  $C_3$  symmetry and the inversion symmetry  $U^*(\mathbf{H}_{\text{ext}}) = -U^*(-\mathbf{H}_{\text{ext}})$ ,

see eqn (7). For this reason the cyan regions are the inverted yellow regions on the opposite side of control space. A rotation of control space by  $2\pi/3$  leaves the control space invariant. Not all excess regions are visible in Fig. 12a. We can infer the location of hidden excess regions from the visible excess regions using these two symmetry operations.

The stationary manifold is formed from multiple copies (according to the multiplicity) of the areas in  $\mathcal{C}$ . As already mentioned the two fences separate the three sub-manifolds of  $\mathcal{M}$ . But on  $\mathcal{M}$  there are additional preimages of the fences in  $\mathcal{C}$  that are different from the fences in  $\mathcal{M}$ . As in the two-fold case we call these pseudo fences. The pseudo fences in  $\mathcal{M}$  and in  $\mathcal{A}$  (Fig. 12b and c) are the borders between the areas with different colors belonging to the same color family (red, green or blue).

In the three-fold case we have an additional type of point that we did not have in the two- and four- fold cases. They are bifurcation points,<sup>51</sup> located on the fences on  $\mathcal{M}$ . These are the only points where more than two areas of different colors meet. We have  $\mathcal{B}_-$  ( $\mathcal{B}_+$ ) bifurcation points where three areas on  $\mathcal{M}_-$  ( $\mathcal{M}_+$ ) and one area on  $\mathcal{M}_0$  meet, and  $\mathcal{B}_0$  bifurcation points where three areas on  $\mathcal{M}_0$  and one area in either  $\mathcal{M}_-$  or  $\mathcal{M}_+$  meet. Both types of bifurcation points split the fences on  $\mathcal{M}$ , as well as their projection onto  $\mathcal{C}$  and onto  $\mathcal{A}$ , into single segments (Fig. 12a).

We now consider a control loop  $\mathcal{L}_C$  that passes through a multiplicity  $m = 6$  excess region. When the loop crosses the fence towards this region the multiplicity increases by two. This happens *via* the creation of an extremum–saddle point pair at the fence on  $\mathcal{M}$ . At the same time the other preexisting stationary points pass a pseudo fence. When the modulation loop leaves the excess region the multiplicity returns to  $m = 4$ . Now a extremum–saddle point pair is annihilated at the fence. When the loop transports a paramagnetic colloidal particle, the particle is now either adiabatically transported through the pseudo fence or the colloid carrying maximum is annihilated at the fence resulting in ratchet motion.

The type of transport is directly related to the number of bifurcation points of each excess area enclosed by the modulation loop. When the modulation loop in  $\mathcal{C}$  encircles an even number of  $\mathcal{B}^-$  ( $\mathcal{B}^+$ ) bifurcation points of one excess area, then the exit of the excess area corresponds to a pseudo fence on  $\mathcal{M}_-$  ( $\mathcal{M}_+$ ) and the transport is adiabatic. If the number of encircled  $\mathcal{B}^-$  ( $\mathcal{B}^+$ ) bifurcation points in an excess area is odd the exit of the excess area corresponds to the fence of  $\mathcal{M}_-$  and the loop induces a ratchet. This ratchet is time reversible if the number of encircled  $\mathcal{B}^0$  bifurcation points is a multiple of 2 (3) for each excess area in the  $S_6$  ( $C_6$ )-like case, and non-time reversible otherwise. A time reversal ratchet is a ratchet where the reversed modulation results in the reversed transport direction.

## 5.2 $S_6$ - $C_6$ -Topological transition

The topology of the  $S_6$ -like ( $C_6$ -like) systems is the same as the  $S_6$ - ( $C_6$ ) symmetric system. A topological transition between  $S_6$ -like and  $C_6$ -like occurs at a critical phase  $\phi_c = \pi/9$  of the pattern. The topological transition can be easily seen in control space. Control space consists of areas with different multiplicity. The shape and location of the areas vary with the phase  $\phi$ . The topology of these areas, however, only differs for the two situations  $\pi/9 < \phi \leq \pi/6$  ( $S_6$ -like) and  $|\phi| < \pi/9$  ( $C_6$ -like). Fig. 12a shows examples of the control spaces  $\mathcal{C}$  for these two cases as well as for the critical transition value  $\phi_c = \pi/9$ .

For any value of the phase  $\phi$  there is one multiply connected area in control space  $\mathcal{C}$ , the tropics (gray) having four preimages ( $m = 4$ ). In the  $S_6$ -like case there are four areas (yellow) surrounded by a maximum fence  $\mathcal{F}_-$  (green) with multiplicity  $m = 6$  housing an extra maximum–saddle point pair. One area is a (hidden) southern area (opposite to the visible cyan northern area) surrounded by a maximum fence  $\mathcal{F}_-$  with 6 segments joined at six  $\mathcal{B}_0$  bifurcation points. The other three are southern satellites surrounded by a maximum fence  $\mathcal{F}_-$  with four segments joined at two  $\mathcal{B}_0$  and two  $\mathcal{B}_-$  bifurcation points. We call these areas southern satellites since at the topological transition they merge with the southern area. The southern area shrinks to zero as the phase approaches  $\phi = \pi/6$  ( $S_6$ -symmetry). Four further areas of multiplicity  $m = 6$  (cyan) housing an extra minimum-, saddle point pair are located opposite to the yellow ones.

The topological transition occurs at  $\phi_c = \pi/9$  where the three southern satellites join with the corresponding southern area. Simultaneously the northern satellites join with the northern area. In each satellite one  $\mathcal{B}_0$  bifurcation point merges with one  $\mathcal{B}_0$  bifurcation point from the polar area. Thus the two polar fence segments of a satellite are both unified with two fence segments of the polar region. This results in a new topology with only two polar areas for the  $C_6$ -like case. Both areas are surrounded by a fence with twelve segments that are separated by a sequence of bifurcation points alternating between  $\mathcal{B}_0$  and  $\mathcal{B}_-$  ( $\mathcal{B}_+$ ).

Due to the inversion symmetry  $U^*(\mathbf{H}_{\text{ext}}) = -U^*(-\mathbf{H}_{\text{ext}})$  the transport of diamagnetic particles on  $\mathcal{M}_+$  is the same as those of the transport of paramagnetic particles on  $\mathcal{M}_-$  at the inverted external magnetic field. In Fig. 12b we depict the topology of the stationary manifold for five different phases  $\phi$ . The true stationary manifold is embedded in a four dimensional curved phase space and we can only show its topology by deforming it until it finally is embedded into three dimensions. The deformation partially breaks the three-fold  $C_3$ -symmetry, however, the inversion symmetry shows up as a up-down mirror symmetry of the manifolds, accompanied by an inversion of the sign of the index of the submanifolds.

In the  $S_6$ -like case there is a (hidden) preimage on  $\mathcal{M}$  of the southern excess area of  $\mathcal{C}$  that is entirely surrounded by  $\mathcal{M}_0$  areas and therefore disconnected from the rest of  $\mathcal{M}_-$ . We call this region  $\mathcal{M}_-^{\text{isolated}}$  and it lies opposite to the visible  $\mathcal{M}_+^{\text{isolated}}$  region in Fig. 12b. This isolated area is surrounded by fences and does not contain pseudo fences. Therefore, all paths of steepest descend can only lead away from it since return points lie on pseudo fences. For this reason the isolated area  $\mathcal{M}_-^{\text{isolated}}$  might be emptied once of a colloid but can never be refilled. Since we are interested in the motion occurring by the periodic repetition of modulation loops this area and hence its projection into  $\mathcal{C}$  is completely irrelevant. After the topological transition to the  $C_6$ -like case the formerly irrelevant polar areas on  $\mathcal{C}$  incorporate the three corresponding satellites. Hence  $\mathcal{M}_-^{\text{isolated}}$  is no longer disconnected from the rest of  $\mathcal{M}_-$  and becomes relevant for the motion.

For any  $\phi$  the stationary manifold  $\mathcal{M}$  is a genus seven surface and there are thus 14 different winding numbers. In the  $S_6$ -like case only two linear independent winding numbers correspond to loops  $\mathcal{L}_{\mathcal{M}} \subset \mathcal{M}_-$  that are lying entirely in  $\mathcal{M}_-$ . Therefore there are only two ways of nontrivial adiabatic transport modes. When  $\mathcal{M}_-^{\text{isolated}}$  joins with the other part of  $\mathcal{M}_-$  ( $\phi = \pi/9$ ) two additional windings around holes of  $\mathcal{M}_-$  occur allowing two new transport routes through the formerly isolated region of  $\mathcal{A}$ .

Fig. 12c shows the projection of the lower half of the stationary manifold into action space  $\mathcal{A}$ . The projection of the upper half exactly matches the lower projection, however, with the colors of the upper half replacing those of the lower half. Fig. 12d shows possible magnetization patterns that generate the universal potentials  $U^*$ . We also show the three-fold symmetric points  $\mathbf{x}_{\mathcal{A},1}$ ,  $\mathbf{x}_{\mathcal{A},2}$ , and  $\mathbf{x}_{\mathcal{A},3}$  within the pattern. Their connections form a 12-, 23-, and 31-network which are the three kinds of high symmetry lines of the lattice.

### 5.3 Modulation loops in the $S_6$ -like case

As in the four-fold symmetric case, in the three-fold case two neighboring allowed regions in  $\mathcal{A}$  only touch each other at a single point, the gate. Hence modulation loops in  $\mathcal{C}$  causing adiabatic transport in  $\mathcal{A}$  have to pass through the grand circles of the gates in  $\mathcal{C}$ .

In the three-fold symmetric case there are six gates  $g^i$ ,  $g_i$ ,  $i = 1, 2, 3$  of two different types  $g^i$  and  $g_i$ . All gates in  $\mathcal{M}$  are closed curves dissected twice by  $\mathcal{F}_+$  and twice by  $\mathcal{F}_-$  (the gates on  $\mathcal{M}$  are shown in more detailed images of  $\mathcal{M}$  in the Appendix A.1 of this work). Hence, for the projection of each gate into  $\mathcal{C}$  there is one minimum gate segment  $g_+$  (blue in Fig. 12a) projected from  $\mathcal{M}_+$ , one maximum segment  $g_-$  (green) projected from  $\mathcal{M}_-$ , and two saddle point gate segments  $g_0$  (red).

Whenever we cross a gate segment of type  $g_-^i$  or  $g_{i,-}$  in the  $m = 4$  (gray) region of  $\mathcal{C}$  the unique maximum in  $\mathcal{A}$  adiabatically passes from one allowed area through the gate  $g_-^i$  or  $g_{i,-}$  in  $\mathcal{A}$  to the allowed area on the other side. For the  $S_6$ -like case the maximum segments  $g_{i,-}$  of the three gates  $g_i$ ,  $i = 1, 2, 3$  lie entirely in the irrelevant southern excess region of  $\mathcal{C}$  and are hence unimportant for transport. For the  $C_6$ -like case all six gates cross both polar excess regions. Therefore all gates become important for transport. Eventually if we have  $C_6$ -symmetry (at  $\phi = 0$ ) the difference in character between both types of gates  $g^i$  and  $g_i$  completely vanishes. Gates cross each other in  $\mathcal{C}$  but in  $\mathcal{M}$  they do not cross. Only when we have a  $S_6$ -symmetry ( $\phi = \pi/6$ ) the three gates  $g_i$  of the isolated allowed region merge such that they touch each other in  $\mathcal{M}$  and are all projected into the one monkey saddle point in  $\mathcal{A}$ . Otherwise the gates are separated curves on  $\mathcal{M}$  much in the same way as in the four-fold case.

For the  $S_6$ -like case we can characterize fundamental modulation loops  $\mathcal{L}_{\mathcal{C}} = \downarrow s \uparrow s'$  in  $\mathcal{C}$  by two loop segments. One is a south heading path  $\downarrow s$  and the other is a north heading path  $\uparrow s'$ . There are three possible types of south traveling paths. It is either of type  $\downarrow g_-^i$ , of type  $\downarrow \mathcal{F}_{-l}^i$ , or of type  $\downarrow \mathcal{F}_{-r}^i$  with  $i = 1, 2, 3$  in all cases.

Each gate segment  $g_-^i$  has two  $B_-$  bifurcation points close to it. A path of type  $\downarrow g_-^i$  is a path that moves south between these two bifurcation points. It might thereby completely stay in the gray  $m = 4$  area or eventually enter a southern satellite (yellow) and exit it again *via* the same southern fence segment. Examples of all types of paths are shown in Fig. 13a. A path of type  $\downarrow \mathcal{F}_{-l}^i$  passes left of the two bifurcation points. It thereby has to enter the  $m = 6$  satellite to the left of gate  $g_-^i$  through one of the two upper fence segments. The path exits the satellite *via* the lower right fence segment that is also crossed by the corresponding gate segment  $g_-^i$ . A path of type  $\downarrow \mathcal{F}_{-r}^i$  is the equivalent path that passes right of the two bifurcation points and enters the satellite to the right of gate  $g_-^i$ . Since the paths  $\downarrow \mathcal{F}_{-l}^i$  and  $\downarrow \mathcal{F}_{-r}^i$  are fence crossing paths they induce ratchet motion and therefore they do not necessarily have to cross the gate. The paths  $\downarrow \mathcal{F}_{-l}^i$  and  $\downarrow \mathcal{F}_{-r}^i$  are topologically protected by the path  $\downarrow g^i$  through the neighboring gate.

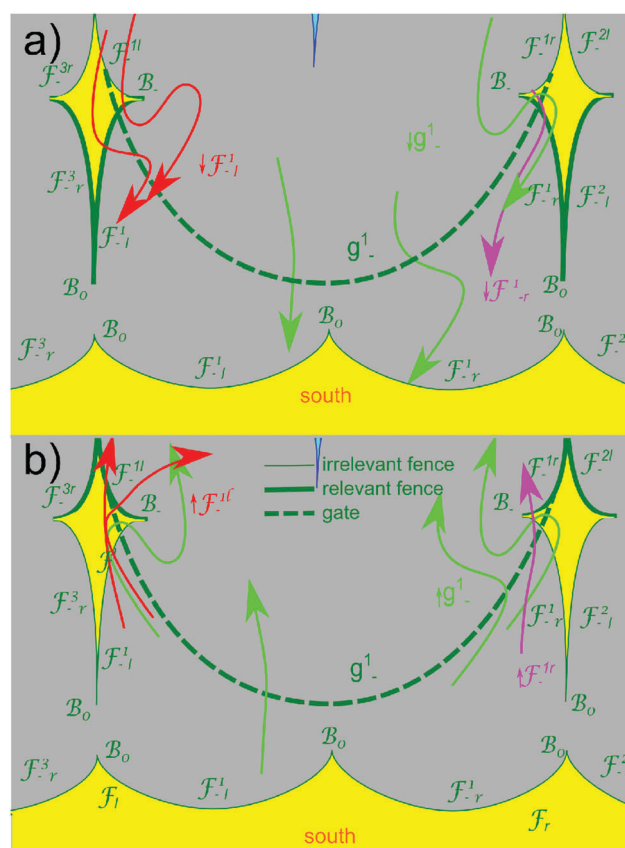


Fig. 13 Paths in the southern hemisphere of  $\mathcal{C}$  relevant for the loops in the  $S_6$ -like case. Paths of type  $\downarrow g_-^i$  and  $\uparrow g_-^i$  are shown in green,  $\downarrow \mathcal{F}_{-l}^i$  and  $\uparrow \mathcal{F}_{-l}^i$  in red and  $\downarrow \mathcal{F}_{-r}^i$  and  $\uparrow \mathcal{F}_{-r}^i$  in purple. The fences of the satellites are enumerated according to the gate closest to them. The index  $l$  ( $r$ ) indicates that the fences are left (right) of the corresponding gate and the position of the index (subscript or superscript) indicates the location of the fence segment in the satellite (up or down). The fence segments of the irrelevant polar fence share the names with those segments of the satellites with which they will join beyond the topological transition. (a) South traveling paths for which the lower fences (highlighted) are relevant. (b) North traveling paths for which the upper fence segments (highlighted) are relevant. See Appendix A.3 for definitions and terminology.

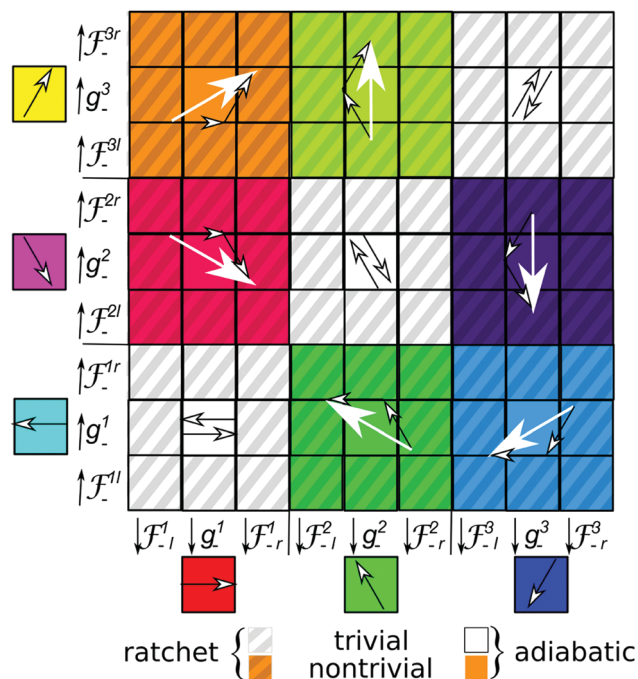


Fig. 14 Phase diagram of the transport of paramagnetic colloids for  $S_6$ -like case. All paths (small arrows) occur on the 31-network. The terminology of the paths is explained in Section 5.3.

We complete the fundamental loop with a north traveling path of type  $\uparrow g^i$ ,  $\uparrow \mathcal{F}^{il}$  or  $\uparrow \mathcal{F}^{ir}$ . A path of type  $\uparrow \mathcal{F}^{il}$  is a north traveling path that passes left of the two bifurcation points. It enters the satellite left of gate  $g^i$  and exits it *via* the upper right fence segment attached to the gate segment  $g^i$  (for examples see Fig. 13b).

In Fig. 14 we depict the phase diagram of the transport induced by the fundamental loops  $\mathcal{L}_C = \downarrow s \uparrow s'$  for the  $S_6$ -like case. Loops for which both paths are of type  $g$  are adiabatic, while loops containing at least one path of type  $\mathcal{F}$  are ratchets. Note that the transport direction is independent of how we enter an  $m = 6$  satellite region. We therefore do not specify the point of entry in the phase diagram. The entry determines whether a ratchet loop is a time reversal or non time reversal loop. If the entry and the exit are attached to a different gate segment the modulation loop is predicted to cause a non-time reversal ratchet. In contrast, loops where paths enter and exit the satellites through the fence segments attached to the same gate are time reversal ratchet loops.

#### 5.4 Modulation loops in the $C_6$ -like case

The  $C_6$ -like case is easier than the  $S_6$ -like case. There is one single southern fence. Non trivial transport of paramagnetic particles occurs for modulation loops that cross the southern fence. Fundamental loops  $\mathcal{L}_C = \downarrow s \uparrow s'$  can be characterized by the south traveling path  $\downarrow s$  through fence segment  $s$  and the path  $\uparrow s'$  traveling north through fence segment  $s'$ . We abbreviate the fence segments for the  $C_6$ -like case with the names of the segments for the  $S_6$ -like case from which they developed. The type of transport as well as the direction can also be

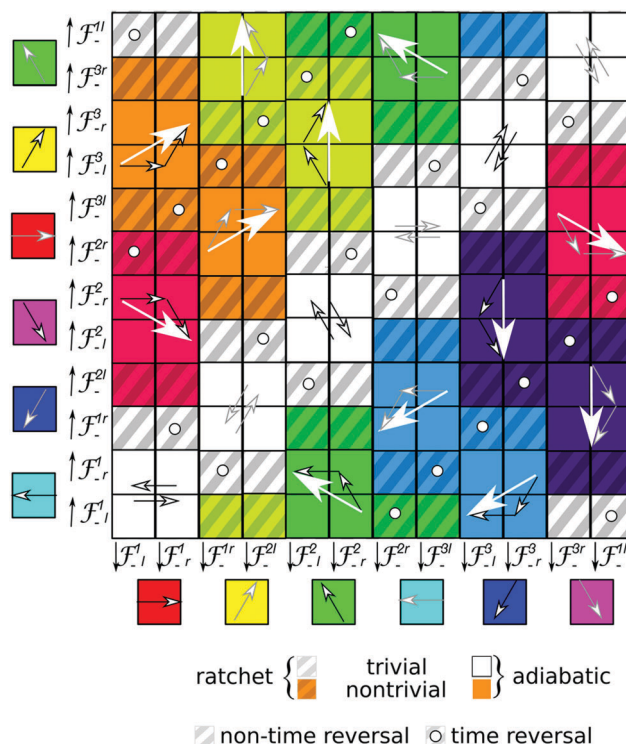


Fig. 15 Phase diagram of the transport for  $C_6$ -like case. Ratchets are topologically protected by the adiabatic loop sharing the same south traveling path. Paths occur on the 31-network (black) or on the 12-network (gray arrows). The choice of network depends on the south heading path  $\downarrow \mathcal{F}^i$ . The terminology of the paths is explained in Sections 5.3 and 5.4.

explained by the bifurcation points the modulation loop encloses. The exact way the gates are crossed is still important. The gates, however, lie in such a way that crossing a fence segment dictates which gate the loop must pass. Hence, the fence segments passed by the loop fully determine the transport direction. Fig. 15 depicts the phase diagram of the transport directions of the  $C_6$ -like case. It is a checker board of adiabatic and ratchet loops. Despite the topological transition the clustering of colors and therefore directions is quite similar to the phase diagram of the  $S_6$ -like case (Fig. 14). Note that in contrast to the  $S_6$  situation we use the same fence segments for both directions of the modulation loops.

Due to the symmetry of the universal potential  $U^*$  diamagnetic transport can be achieved in the same way by simply reversing the field  $\mathbf{H}_{\text{ext}} \rightarrow -\mathbf{H}_{\text{ext}}$ . In contrast to the four-fold case the transport in all three-fold cases is more versatile. Paramagnetic and diamagnetic colloids are no longer fixed to the same transport direction but can be transported fully independently, because  $\mathcal{F}_-$  and  $\mathcal{F}_+$  are well separated in  $\mathcal{C}$ .

#### 5.5 Three and six fold symmetry

Let us reconsider the symmetry of the three-fold lattice. As we have seen there are three points  $\mathbf{x}_A^1 = 0$ ,  $\mathbf{x}_A^2 = (\mathbf{a}_1 + \mathbf{a}_2)/3$  and  $\mathbf{x}_A^3 = -(\mathbf{a}_1 + \mathbf{a}_2)/3$  in the unit cell of  $\mathcal{A}$  with three-fold symmetry (see Fig. 2c). As we vary  $\phi$  one of these points acquires a higher  $C_6$  symmetry at  $\phi = n\pi/3$ , with  $n = 1, 2, 3, \dots$ . The higher

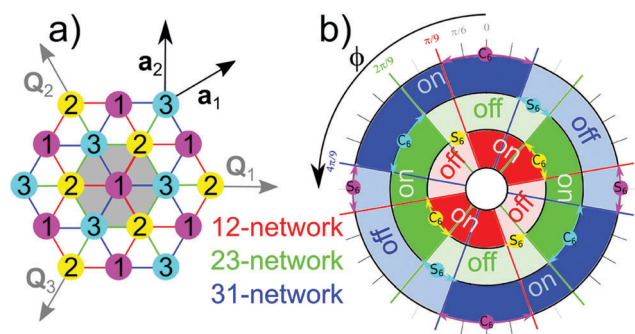


Fig. 16 (a) Threefold unit cell with the three possible symmetry points  $\mathbf{x}_1$  (purple),  $\mathbf{x}_2$  (yellow) and  $\mathbf{x}_3$  (cyan). There are three networks along which transport is possible, the 12-network (red lines), the 31-network (blue) and the 23-network (green). (b) State of each network as a function of the phase of the pattern. Activated (on) networks have full colors while deactivated (off) networks have light colors. Phases  $\phi$ , where one of the symmetry points acquires higher  $S_6$  or  $C_6$  symmetry are marked by circles of the color of the high symmetry point. Topological transitions between  $S_6$  and  $C_6$  symmetries are also marked with colored thick lines. The state of a network can only change at the topological transition. See Appendix A.3 for definitions and terminology.

symmetry permutes amongst the three points. Similarly, one of the points acquires a  $S_6$  symmetry for  $\phi = \pi/6 + n\pi/3$ . Connections between two different points  $\mathbf{x}_A^i$  and  $\mathbf{x}_A^j$  define a  $ij$ -network that might enable transport between two unit cells. There are three possible networks: the 12-network, the 23-network, and the 31-network (see Fig. 16a).

For a polar orientation of the external field at least one of the three points is a minimum and at least one is a maximum. At the  $S_6$  symmetry point the potential has a monkey saddle for a polar external field orientation and a normal saddle point otherwise. In any case the  $S_6$  point lies in the forbidden region. Hence the  $S_6$  symmetry shuts off all connections to the point with  $S_6$  symmetry. Only the network between the remaining two symmetry points can be used for transport *via* appropriate modulation loops. In contrast when the pattern acquires  $C_6$  symmetry the point with  $C_6$  symmetry is connected to both other symmetry points *via* two networks. The network between the lower  $C_3$  symmetry points is shut off.

As we vary  $\phi$  from 0 to  $2\pi$  each network is switched on and off twice. For any  $\phi$  at least one network is on and at least one network is off. The exact number of active networks depends on whether  $\phi$  is in the neighborhood of a  $C_6$  or a  $S_6$  symmetry. In Fig. 16b we plot the symmetry of the three points and the state of the three networks as a function of  $\phi$ . Note the close relationship to an antiferromagnetic equilibrium Ising system in a triangular lattice.<sup>52</sup> Both systems are geometrically frustrated, with not all possible connections between sites being turned on.

### 5.6 Experiments on the $S_6$ -like symmetry

Three fold symmetric patterns with lattice constant  $a = 7 \mu\text{m}$  have been created in the same way as the four-fold patterns. Here again lithographic edge effects of the patterning process render white regions larger than the black regions such that the

average magnetization of the film is non-zero. This breaks the  $S_6$ -symmetry and shifts the phase  $\phi < \phi_{\text{mask}}$  of the patterns away from the phase  $\phi_{\text{mask}}$  of the lithographic mask toward the  $C_6$ -like symmetric direction.

To show the topological protection of the transport directions in the  $S_6$ -like case we apply different fundamental modulation loops that all fall in the classes  $\mathcal{L}_C = \downarrow \mathcal{F}_{-r}^2 \uparrow \mathcal{F}_{-r}^{3l}, \downarrow g^2 \uparrow g^3$ , or  $\downarrow \mathcal{F}_{-l}^2 \uparrow \mathcal{F}_{-l}^{3r}$ , but have different proximity to the satellite centered at  $-\mathbf{Q}_1$  in  $\mathcal{C}$ . In Fig. 17 we plot the corresponding trajectories of paramagnetic particles on a  $S_6$ -like pattern. All loops induce transport in the  $\mathbf{a}_2$  direction, which is in accordance with the predictions of Section 5.3. It does not matter which particular modulation loop within the same homotopy class we choose, the global result after completing the loop is the transport of the paramagnetic particle by one unit vector  $\mathbf{a}_2$ . Modulation loops closer to the encircled satellite have a straighter trajectory than loops passing the equator far from it (see Fig. 17). For small as well as for large modulation loops passing the equator close to one of the southern (green) satellites, we observe the transition from adiabatic toward ratchet motion (dashed modulation loops in Fig. 17a). Therefore, ratchet loops are observed in a larger region than expected from the theoretically predicted positions of the  $B_-$  bifurcation points and the fences of the satellites. However their occurrence is topologically equivalent to the theoretical model. Note that passing the blue fences is irrelevant for the motion of paramagnetic particles. The difference between the adiabatic and ratchet motion will be shown in detail in Section 5.7.

In a second step we immersed the paramagnetic particles into a ferrofluid on top of the pattern and added effectively

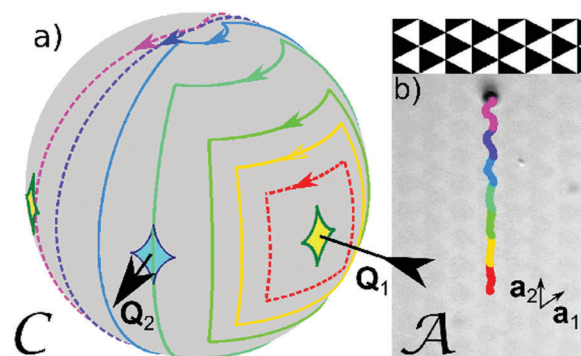


Fig. 17 (a) Different modulation loops in  $\mathcal{C}$  encircling the satellite around  $-\mathbf{Q}_1$ . The loops fall into the three classes  $\mathcal{L}_C = \downarrow \mathcal{F}_{-r}^2 \uparrow \mathcal{F}_{-r}^{3l}$  (dashed red),  $\mathcal{L}_C = \downarrow g^2 \uparrow g^3$  (solid yellow, green, light green, and blue) and  $\mathcal{L}_C = \downarrow \mathcal{F}_{-l}^2 \uparrow \mathcal{F}_{-l}^{3r}$  (dashed purple and magenta), where dashed lines are indicating modulation loops that induce ratchets. (b) Corresponding experimental trajectories of a paramagnetic colloidal particle on top of the  $S_6$ -pattern. The (dashed) ratchet loops fall into the same homotopy class as the (solid) adiabatic loops and therefore the travel direction (along  $\mathbf{a}_2$ ) is topologically protected. Passing blue fences is irrelevant for the motion of the paramagnets. Note that some of the experimentally observed ratchet loops do not pass through the theoretical green fences of control space. The background in (b) is the reflection microscopy image of the underlying lithographic magnetic pattern. A video clip of the motion of the paramagnetic colloidal particle is provided in ref. 45.

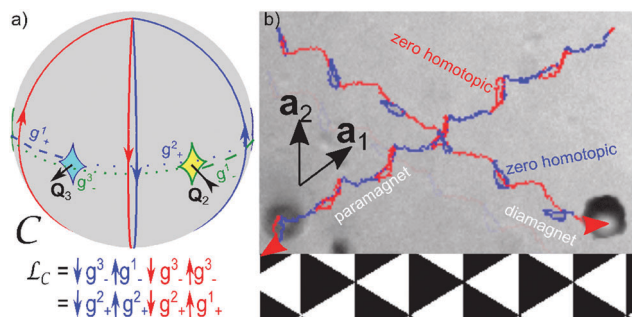


Fig. 18 (a) Control space  $\mathcal{C}$  with the applied modulation double loop  $\mathcal{L}_C = \downarrow g^3 \uparrow g^1 \downarrow g^3 \uparrow g^3 = \downarrow g_+^3 \uparrow g_+^1 \downarrow g_+^3 \uparrow g_+^3$  consisting of two joint fundamental modulation loops. (b) Experimental trajectories of a paramagnetic and a diamagnetic colloidal particle in action space  $\mathcal{A}$  caused by this loop. The result is the transport of paramagnetic and diamagnetic particles in directions differing by an angle of  $2\pi/3$ . While the first (blue) fundamental loop transports the paramagnetic particles it is zero homotopic for the diamagnetic particles and vice versa for the second (red) loop. The background is the reflection microscopy image of the lithographic magnetic pattern. A video clip of the motion of the paramagnetic colloidal particle is provided in ref. 45.

diamagnetic particles. We subjected both types of particles to a double loop  $\mathcal{L}_C = \mathcal{L}_C^1 \mathcal{L}_C^2$  consisting of two fundamental loops  $\mathcal{L}_C^1 = \downarrow g^3 \uparrow g^1 = \downarrow g_+^3 \uparrow g_+^1$ , and  $\mathcal{L}_C^2 = \downarrow g^3 \uparrow g^3 = \downarrow g_+^3 \uparrow g_+^3$  (Fig. 18a). The first loop  $\mathcal{L}_C^1$  (blue) transports the paramagnetic particles by the unit vector  $-\mathbf{a}_1$ .  $\mathcal{L}_C^1$  is zero homotopic for the diamagnets since it is only crossing the same minimum segment  $g_+^3$  twice. The second fundamental loop  $\mathcal{L}_C^2$  (red) is zero homotopic for the paramagnets and transports the diamagnets in the different  $\mathbf{a}_1$ - $\mathbf{a}_2$  direction. The resulting trajectories of paramagnetic and diamagnetic particles to the double loop  $\mathcal{L}_C$  are shown in Fig. 18b. The double loop  $\mathcal{L}_C$  is an example of a combination of two modulation loops that induces transport of paramagnetic and diamagnetic particles in two independent arbitrary directions on top of a  $S_6$ -like pattern.

The experimental trajectories not only are in accordance with the theory for the previous loops, but for all possible fundamental loops. To experimentally show this we applied a poly-loop for paramagnetic particles that combines all the fundamental loops of the phase diagram of Fig. 14. In Fig. 19 we plot the experimental trajectory of paramagnetic particles with the fundamental sections colored with the color of the corresponding theoretical fundamental loop of Fig. 14. All fundamental loops transport into the theoretically predicted directions. In conclusion the experimental response of the particles on a  $S_6$ -like pattern to all shown modulation loops is in topological agreement with the theoretical predictions. The only phenomenon that we could not observe in our experiments is a non time reversal ratchet. The reasons for this are discussed in Section 6.

### 5.7 Experiments on the $C_6$ -like symmetry

The experimental trajectories of the adiabatic modulation loops of the  $C_6$ -like case are also in accordance with the theory.

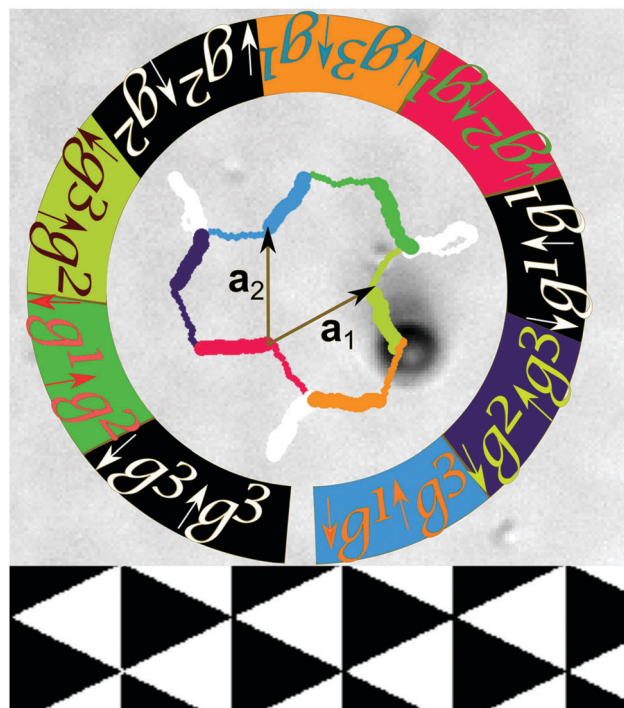


Fig. 19 Experimental trajectory of a paramagnetic colloidal particle on top of a  $S_6$  pattern caused by a modulation poly-loop in  $\mathcal{C}$  consisting of a sequence of all fundamental modulation loops. The fundamental loops are colored according to the loops in the phase diagram in Fig. 14. South traveling segments are marked as thick lines. North traveling segments are marked as thin lines. A video clip of the motion of the paramagnetic colloidal particle is provided in ref. 45.

Fig. 20 shows the trajectory of a paramagnetic particle subject to an adiabatic poly-loop that consists of all different adiabatic right fence segment crossing fundamental loops of the phase diagram in Fig. 15 combined. We plot the trajectories of the particles in the color of the corresponding fundamental loops of the phase diagram. All adiabatic loops transport into the directions predicted by the theory.

In contrast to the universal two-fold and four-fold symmetric patterns the three and sixfold symmetric patterns not only support adiabatic motion but also ratchet type motion can be observed. To visualize the characteristics of the different types of motion we use palindrome modulation loops  $\mathcal{L}_C = \tilde{\mathcal{L}}_C \tilde{\mathcal{L}}_C^{-1} = \downarrow \mathcal{F}^{3r} \uparrow s \downarrow s \uparrow \mathcal{F}^{3r} = \mathcal{L}_C^{-1}$ . They consist of a loop  $\tilde{\mathcal{L}}_C = \downarrow \mathcal{F}^{3r} \uparrow s$  that is first played in the forward direction and afterwards played again but this time reversed, *i.e.*, in the backward direction. While the first path  $\downarrow \mathcal{F}^{3r}$  of  $\tilde{\mathcal{L}}_C$  is kept the same, the second path  $\uparrow s$  varies along the eleventh column of the phase diagram (Fig. 15). We start with (a)  $s = \mathcal{F}^{11}$  which makes  $\mathcal{L}_C$  an adiabatic zero homotopic loop and then trace the transition towards adiabatic transport (d) ( $s = \mathcal{F}^{21}$ ) via two different non time reversal ratchets (b) ( $s = \mathcal{F}_1^1$ ) and (c) ( $s = \mathcal{F}_r^1$ ). Afterwards we show the crossover toward another adiabatic transport direction (g) ( $s = \mathcal{F}^{2r}$ ), this time by passing a time reversal ratchet (e) ( $s = \mathcal{F}_1^2$ ) and another non time reversal ratchet (f) ( $s = \mathcal{F}_r^2$ ). Trajectories of these motions are shown in Fig. 21.

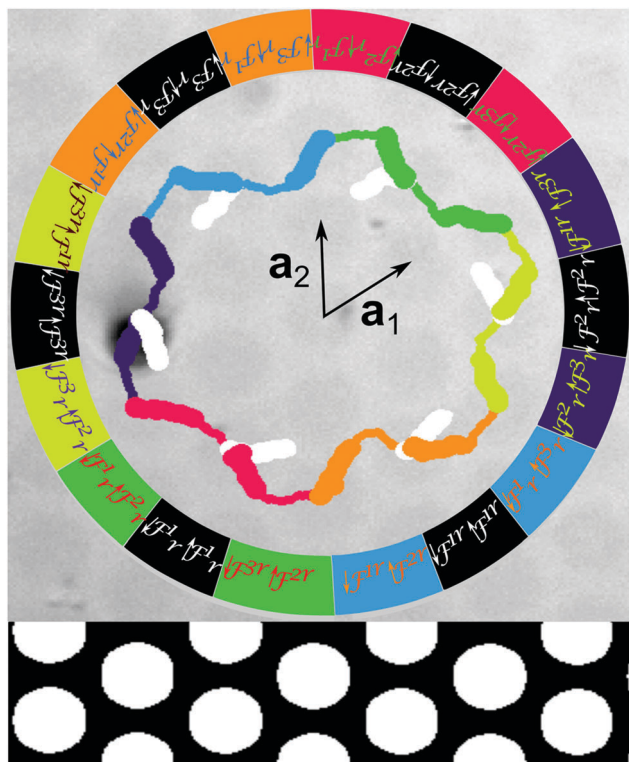


Fig. 20 Experimental trajectory of a paramagnetic colloidal particle on top of a  $C_6$ -pattern. The colloidal particle is subjected to a modulation poly-loop in  $\mathcal{C}$  which is a combination of all adiabatic right fence crossing fundamental modulation loops. The single fundamental loops are colored according to the loops in the phase diagram in Fig. 15. South traveling segments are again marked as thick lines while north traveling segments are thin lines. Similar to the theory the circular bubble domains have positive magnetization. However the reflection microscopy image in the background has an inverted contrast such that the bubbles are dark. A video clip of the motion of the paramagnetic colloidal particle is provided in ref. 45.

Obviously, if the induced motion is adiabatic the colloidal particle is tracing some path in  $\mathcal{A}$  during the forward motion, and then returns to the initial position by tracing the exact same path in the backward direction. Three such adiabatic paths (a, d and g) are shown in Fig. 21. All adiabatic paths are caused by modulation loops making use of only upper type fence crossings and cause motion on the 12-network only. In contrast the irreversible nature of ratchet jumps causes the colloidal particles to move on a different path in  $\mathcal{A}$  during the forward and backward modulation loop. The reason for this is that the forward loop  $\tilde{\mathcal{L}}_C$  uses a south traveling path crossing an upper type fence  $\mathcal{F}^{3r}$  and a north traveling path crossing a lower type fence. When  $\tilde{\mathcal{L}}_C$  is played forward the colloid travels the first half adiabatically from  $\mathbf{x}_{A,1}$  toward  $\mathbf{x}_{A,2}$  since the modulation path enters the southern excess region and upper type fence crossings support motion on the 12-network. The second half of  $\tilde{\mathcal{L}}_C$  must bring the particle back to  $\mathbf{x}_{A,1}$ . However, adiabatic motion with lower type fence crossing paths is possible only on the 31-network and our particle is currently at  $\mathbf{x}_{A,2}$  that is not part of this network. Hence the particle performs a ratchet

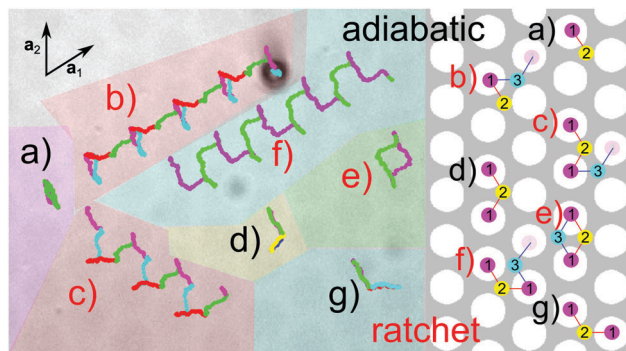


Fig. 21 Experimental trajectories of paramagnetic colloidal particles in action space  $\mathcal{A}$  above a  $C_6$ -symmetric pattern. The trajectories are caused by various zero homotopic palindrome modulation loops  $\mathcal{L}_C = \downarrow \mathcal{F}^{3r} \uparrow s \downarrow s \uparrow \mathcal{F}^{3r}$  with (a)  $s = \mathcal{F}^{1l}$  (b)  $s = \mathcal{F}_1^1$ , (c)  $s = \mathcal{F}_r^1$ , (d)  $s = \mathcal{F}^{2l}$ , (e)  $s = \mathcal{F}_3^2$ , (f)  $s = \mathcal{F}_r^2$ , and (g)  $s = \mathcal{F}^{2r}$ . The paths in  $\mathcal{A}$  are colored according to the four paths of the modulation loop as indicated by the squares in the phase diagram Fig. 15. In the cases (a, d and g) the motion is adiabatic and the colloidal path in  $\mathcal{A}$  consists of two forward paths that coincide with the backward path. The case (e) corresponds to a time reversible ratchet with a zero homotopic path in  $\mathcal{A}$ . However the colloid is moving on different forward and backward paths that belong to two different networks indicated to the right. The other cases (b, c and f) are non time reversible ratchets where the zero homotopic modulation loops in  $\mathcal{C}$  induce non-zero homotopic (open) paths of the colloids in  $\mathcal{A}$ . The predicted paths between the high symmetry points for all loops are shown to the right. Video clips of the motion of the paramagnetic colloidal particle caused by the loops in (b, d and e), are provided in ref. 45.

jump back toward  $\mathbf{x}_{A,1}$ . When  $\tilde{\mathcal{L}}_C$  is played backward the particle adiabatically moves from  $\mathbf{x}_{A,1}$  toward  $\mathbf{x}_{A,3}$  and jumps back *via* a ratchet jump. The full palindrome loop hence visits the high symmetry points in the sequence:  $\mathbf{x}_{A,1}$ ,  $\mathbf{x}_{A,2}$ ,  $\mathbf{x}_{A,1}$ ,  $\mathbf{x}_{A,3}$ ,  $\mathbf{x}_{A,1}$ . For time reversal ratchets the colloidal particle returns to its initial position after the full modulation loop  $\mathcal{L}_C$ , however by using a backward path in  $\mathcal{A}$  different from the forward path. Such a time reversible ratchet path is shown in Fig. 21e. In general palindrome modulation loops cause non-time reversal ratchet motion. The particle does not return to its initial position after a complete modulation loop but is transported by one unit vector. Three non-time reversible ratchet paths of this type are shown in Fig. 21b, c, and f.

The characteristics of the adiabatic and ratchet motion can also be inferred without looking at the differences between the forward and backward paths in  $\mathcal{A}$ . We measure the speed  $\dot{s}_A$  of the colloids in  $\mathcal{A}$  versus the normalized path length  $s_C$  of the modulation loop. We parametrize the forward modulation loop  $\tilde{\mathcal{L}}_C$  from 0 to  $2\pi$  and the backward loop  $\tilde{\mathcal{L}}_C^{-1}$  from  $2\pi$  to 0 such that the path length  $s_C$  in Fig. 22 runs back and forth between 0 and  $2\pi$ . Ratchet loops can be distinguished from adiabatic loops by the ratchet jumps that have a significantly higher speed than the adiabatic motion. These jumps occur during the second half (magenta) of the forward and the second half (green) of the backward modulation when the modulation hits the fences and leaves the southern excess region in  $\mathcal{C}$ . There are also smaller maxima in the speed of the adiabatic motion when the beads pass the gates. The increased gate speed is a result of

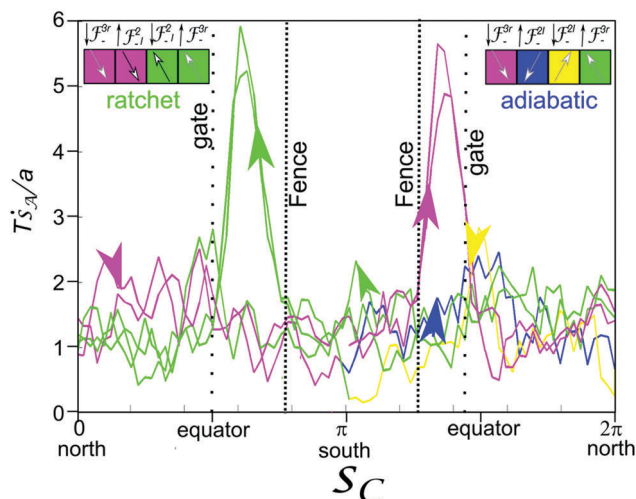


Fig. 22 Speed  $\dot{s}_A$  in  $\mathcal{A}$  of the colloidal motion induced by the palindrome modulation loop (d) and (e) of Fig. 21. The speed is normalized by the lattice constant  $a$  and the period  $T$  of one sub loop. It is plotted against the normalized path length  $s_C$  of the modulation in  $\mathcal{C}$  ranging from 0 to  $2\pi$  for the forward modulation and from  $2\pi$  to 0 for the backward modulation. Ratchet jumps in the ratchet modulation loop (maximum speed) occur in the second half of the forward (magenta maximum) and backward path (green maximum) when the modulation loop leaves the southern excess region in  $\mathcal{C}$  via the fence. Also the adiabatic speed profile (magenta/blue/yellow/green modulation, (d) in Fig. 21) exhibits maxima when the modulation crosses the gates. But they are clearly smaller than the maxima of the ratchet jumps.

the way that curves which are passing the gates in  $\mathcal{M}$  are projected into  $\mathcal{A}$  and  $\mathcal{C}$ . The projections are causing a maximum in the conversion of the speed in action space versus the speed in control space at the gate. In our special case the gates seem to be located less polar than the fences, which contradicts the theoretical predictions for the  $C_6$ -symmetric case but is in accordance with theoretical predictions for weakly broken  $C_6$ -symmetry.

We are hence able to independently characterize the type of motion and the particular path taken by the colloids. Both the experimentally determined types of motion as well as the directions are in perfect agreement with the theoretically predicted phase diagram (Fig. 15) for the  $C_6$ -like case.

For the  $S_6$ -like case we also observe adiabatic and ratchet motion in topological agreement to the theory. However, we did not succeed in finding palindrome loops causing non-time reversible ratchets as predicted by the theory and simulations. Instead, we observe that loops, which are supposed to induce non time reversal ratchets, cause the coexistence of time reversible ratchets with different directions above different unit cells. The directions thereby correspond to either the theoretically predicted forward or backward direction.

### 5.8 Experiments on the $S_6$ - $C_6$ -topological transition

To illustrate the  $S_6$ - $C_6$ -topological transition we produced lithographic patterns with a slowly varying pattern phase  $\phi(x)$ . This continuously converts a  $C_6$  pattern into a  $S_6$  pattern within a spacial range of approximately 20 unit cells. In Fig. 23 we

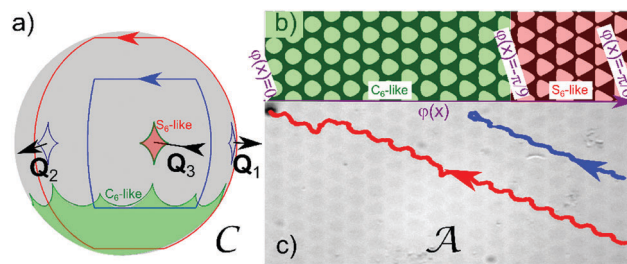


Fig. 23 Motion of colloids in a phase gradient pattern. (a) Control space with two modulation loops (blue and red) circulating around  $-Q_3$ . We have plotted the relevant excess satellite regions of the  $S_6$ -symmetric case (red area) and the excess region of the  $C_6$ -symmetric case (green area). (b) Scheme of the slowly varying phase pattern. The pattern is  $C_6$ -like to the left and  $S_6$ -like to the right. (c) Experimental trajectories of paramagnetic particles induced by the two modulation loops. Both loops encircle the  $S_6$ -symmetric satellite excess region and thus induce transport on the  $S_6$ -like pattern. The blue modulation loop barely touches the  $C_6$ -like fence in  $\mathcal{C}$  which destroys the motion of the corresponding particle when it reaches  $C_6$ -like territory. The red loop in contrast fully enters the southern  $C_6$ -symmetric excess region in control space and leaves it only once. Therefore the red trajectory persists well in to the  $C_6$ -like territory. A video clip of the motion of the paramagnetic colloidal particle is provided in ref. 45.

show the motion of paramagnetic particles on such a phase gradient pattern induced by two different modulation loops (blue and red) encircling the  $-Q_3$  point. Both loops induce transport on the  $S_6$ -like pattern. However as the phase of the pattern declines towards zero (the phase of the  $C_6$ -pattern) the encircled satellite excess region of control space moves out of the blue loop such that the motion ceases beyond the critical phase  $\phi < \phi_c = \pi/9$ . The blue loop then touches the southern fence of the  $C_6$ -symmetric pattern, which is no longer sufficient to induce transport on the  $C_6$ -like pattern. The red loop fully crosses the southern fences of the  $C_6$ -symmetric pattern. Therefore the motion of the particle persists as it enters  $C_6$ -like territory in action space  $\mathcal{A}$ . The direction of transport is thereby topologically protected over the transition.

Upon the transition between  $S_6$  and  $C_6$  also the state of networks available for transport changes. While in the  $C_6$ -like pattern the 12- and the 31-networks are active the first one is switched off in a  $S_6$ -like pattern and only the 31-network is available for transport (see Fig. 16). To experimentally demonstrate this we apply a double loop of the type  $\mathcal{L}_C = \mathcal{L}_C^{12} \mathcal{L}_C^{31}$  with  $\mathcal{L}_C^{12} = \downarrow \mathcal{F}_{-r}^2 \uparrow \mathcal{F}_{-r}^1$  a fundamental loop passing through the lower fence segments (blue loop) and  $\mathcal{L}_C^{31} = \downarrow \mathcal{F}_{-r}^2 \uparrow \mathcal{F}_{-r}^1$  (red loop) a fundamental loop passing through upper fence segments of the  $C_6$ -symmetric case as shown in Fig. 24d. For the  $C_6$ -like patterns the theory predicts an alternating use of the 12-network and the 31-network. The overall transport direction is the same for both fundamental loops. The same double loop converts into a  $\mathcal{L}_C = \downarrow g_-^2 \uparrow g_-^1 \downarrow g_-^2 \uparrow g_-^1$  loop for the  $S_6$ -like case where transport is only possible on the 31-network. In Fig. 24a and b we show the motion subject to this modulation loop on the  $C_6$ -like and the  $S_6$ -like patterns, respectively. Clearly the motion of the paramagnetic particle on the  $C_6$ -like pattern makes use of the 12- and the 31-network. We observe an alternating

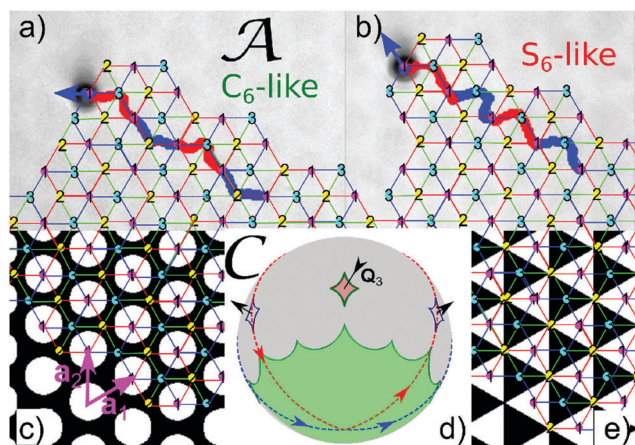


Fig. 24 Motion of paramagnetic colloids on (a) a  $C_6$  symmetric pattern (scheme in (c)) and (b) a  $S_6$  symmetric pattern (scheme in (e)). The particles are subject to a modulation double loop  $\mathcal{L}_C = \mathcal{L}_C^{12} \mathcal{L}_C^{31}$  with  $\mathcal{L}_C^{12} = \downarrow \mathcal{F}_{-r}^2 \uparrow \mathcal{F}_{-r}^1$  (blue loop) and  $\mathcal{L}_C^{31} = \downarrow \mathcal{F}_{-r}^2 \uparrow \mathcal{F}_{-r}^1$  (red loop) crossing different segments of the  $C_6$ -fence. (d) Control space with the combined modulation loop consisting of two fundamental loops (blue and red) which are both encircling the  $S_6$ -symmetric excess region. We have plotted the relevant excess regions of the  $S_6$ -symmetric ( $\phi = -\pi/6$ ) case (red area) and the  $C_6$ -symmetric case (green area). The induced motion on a  $C_6$ -symmetric pattern is shown in (a). Both sub-loops induce motion on different networks resulting in a trajectory that alternately uses the 12 and the 31 network. In the  $S_6$ -symmetric pattern only the 31-network is active. Therefore the induced motion shown in (b) has to use the 31-network during both sub-loops.

transport over these two networks. On the  $S_6$ -like pattern transport happens *via* the 31-network only. The motion is again topologically protected in the direction, *i.e.* the modulation that before enforced the use the other network now also has to use the 31-network into the same direction.

## 6 Discussion

We have seen that most of the theoretically predicted features are experimentally robust. This ensures that colloids elevated only a few microns above the pattern behave pretty much the same way as predicted for universal potentials. The few deviations of experiment and theory can mostly be attributed to non-universal proximity effects. These arise from larger reciprocal lattice vectors contributing to the colloidal potential. We have shown, however, that higher reciprocal lattice vectors change the position of certain transport direction transitions, but not the topology of the problem as long as their influence is not too strong. Experimental proofs for proximity effects have been shown at different elevations for the two-fold symmetric problem. These effects will of course also play a role on lattices of higher symmetry and for non-symmetric magnetic lattices where such symmetry is broken by higher reciprocal lattice vector contributions. For the higher symmetric patterns we did not discuss these effects in detail and minimized them by performing experiments at sufficient elevation above the pattern. However, they are still visible in some experimental features. In the four-fold symmetric experiments for example the fence point is not a point but a finite area. Modulation loops must wind around this

larger area instead of winding around the theoretical point and hence modulation loops can not be chosen arbitrarily small to cause adiabatic transport.

The Bravais lattice of any periodic pattern has inversion symmetry and thus  $C_2$  symmetry. Filling the unit cell of such a Bravais lattice with a magnetization pattern that has no net magnetic moment will generate a Fourier series that has contributions from Fourier coefficients at the non zero reciprocal lattice vectors. The contributions from the shortest reciprocal lattice vectors will always have one of the universal rotation symmetries. The symmetry can be broken by higher order reciprocal lattice vectors. The magnetic field contribution to a reciprocal lattice vector decays in the  $z$ -direction with the magnitude of the reciprocal lattice vectors, which is the reason why every transport at sufficient elevation of the order of the period will have exactly the characteristics of one of the patterns described in this paper. The transport remains topologically protected also for the symmetry broken case when the breaking of the symmetry is not too strong. There will be a topological transition to a non-transport regime for any type of pattern if one places the colloids close enough to the pattern. There might be other topological transport modes for symmetry broken patterns at intermediate elevation. These however are not universal as they will depend on all details of the pattern, field strength *etc.*

A difference between experiment and theory that cannot be explained with non universal proximity effects is the absence of non time reversible ratchets in the three-fold symmetric  $S_6$ -like case. There instead of non time reversible ratchets we observed the coexistence of time reversible ratchets of different direction above different unit cells of the pattern. We attribute those effects to the noise of the magnetic patterns. Presumably the net magnetization of each unit cell does not vanish as required by eqn (6), but acquires values that might differ from one unit cell to the next. A non vanishing magnetization acts like an additional external field in the  $z$ -direction and therefore shifts the satellites to the north or to the south. We may see the effect of magnetization noise for the simple example of an additional staggered magnetization alternating between positive and negative values in neighboring unit cells. The staggered magnetization doubles the unit cell and therefore also doubles the length of the fence. Each satellite becomes a double satellite around which the fence circles twice. When we increase the magnitude of the staggered magnetization one half of the double satellite moves north while the other half moves south (see Fig. 25). Let us consider a modulation loop segment (red) that passes the unsplit double satellite on opposing segments. We expect this loop to induce a non time reversal ratchet. When the satellite splits the modulation loop segment will eventually pass the upper half of the double satellite south of the two  $\mathcal{B}_-$  bifurcation points and the lower half north of the other two  $\mathcal{B}_-$  bifurcation points. This, however, will now cause time reversible ratchets into different directions on one and the other half of the larger unit cell. This is exactly what we observe in the experiments, however, of course not in the simple staggered way predicted by our simplified period doubled theory.

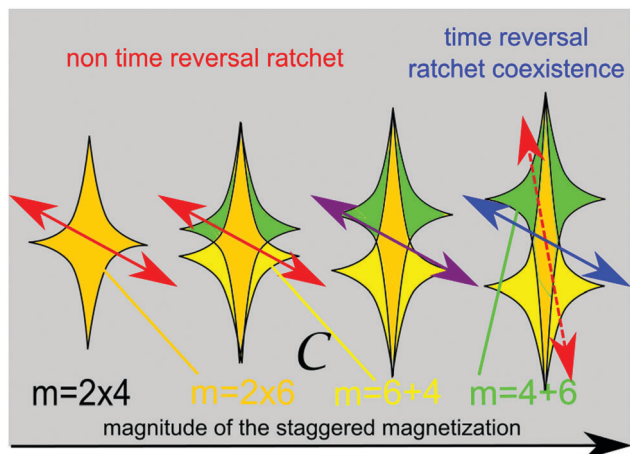


Fig. 25 Splitting of a satellite when switching on a staggered magnetization that doubles the period, doubles the fence and doubles the multiplicity  $m$ . The net magnetization of the two new different half unit cells shifts one half of the satellite fence to the north and the other half to the south. As a result a path that initially passed the fences on opposite sides of the satellites (red arrow) now cuts the northern (southern) half of the double satellites on the neighboring southern (northern) fence segments (blue arrow). Instead of a non time reversal ratchet this produces time reversible ratchets with different directions in one and the other new half unit cell.

In Fig. 22 we measured the speed of adiabatically moving colloidal particles. Gates in control space can then be identified by the location of the maximum speed in  $\mathcal{A}$ . The experiments measured the positions of the extremum segments of the gates to lie in the  $m = 4$  region, while the theory of the  $C_6$  symmetric case predicts that they lie inside of the excess area in  $\mathcal{C}$ . We have already mentioned that there might be a mismatch between the phase of the lithographic mask and the phase of the actual pattern. Indeed the lithographic writing process presumably produces a magnetization pattern with a phase that differs from the desired phase. A phase that is slightly different from the  $C_6$ -symmetry would allow for gates in the tropics of  $\mathcal{C}$  and hence explain the observed deviation. Since the exact path of the gate on  $\mathcal{M}$  is a feature that is not topologically robust it is conceivable that either the phase shift or proximity effects might cause this discrepancy.

To achieve adiabatic transport our modulation loops in control space must be modulated at an angular frequency  $\omega_{\text{ext}}$  that is significantly smaller than the intrinsic angular frequency  $\omega_{\text{int}} \propto e^{-Qz}M$ . For the lithographic magnetic patterns this restricts our modulation frequencies to  $\omega_{\text{ext}} \approx 0.1$  Hz. For useful applications one would have to improve the saturation magnetization or the thickness of the lithographic patterns to increase the modulation frequency. The garnet films we used for the two-fold stripe pattern as well as for experiments on  $C_6$ -like patterns in ref. 20 allowed for the use of up to two orders of magnitude higher modulation frequencies. The closer the particles are to the pattern the faster we might modulate the field, however, the less universal will be the behavior of the transport. An elevation of roughly half the lattice constant seems to be a good compromise that does not yet change the topology of the transport.

We describe our ratchet as a deterministic ratchet, *i.e.* thermal diffusion of particles only happens during very short and therefore irrelevant times when the colloidal particles sit right on the fence. This short diffusion will not lead to a broadening distribution of transport directions as long as we avoid the  $\mathcal{B}_0$  points. When using modulation loops passing close to a  $\mathcal{B}_0$  point the particles may access the two alternative paths of steepest descent also in the surroundings of this point. Thermal effects broaden the fences. A transition to a thermal ratchet will occur for temperatures where the broadened fences overlap. Some of the topological properties might persist even then and thus also explain the omni-directional transport observed in such thermal ratchets.<sup>28</sup>

Comparing our system with topological crystalline insulators<sup>4–9</sup> we note that the gates in our system are the analogues to the Dirac-cones in the quantum systems. Gates are lying on high symmetry points in the lattices with even  $C_4$ , and  $C_6$  symmetries, while they lie on the  $ij$ -network for the three-fold symmetric lattices. The situation is comparable to the position of Dirac-cones lying on high symmetry points and lines in the first Brillouin zone of the lattices of different symmetry. As in topological crystalline insulators their number and robustness varies based on the symmetry of the lattice.

Comparing our driven system with Floquet topological quantum systems<sup>10,11</sup> we note that time dependent interactions of Floquet topological insulators usually must wind around the north–south axis to cause topologically non trivial behavior. This is because the unperturbed time independent Hamiltonian operator is diagonalized with respect to the  $z$ -component of the spin respectively pseudo spin operator. Different time dependent driving, such as THz-oscillating magnetic fields, stress modulation, or modest in plane electric field modulations<sup>53</sup> are experimental ways to achieve non trivial behavior. Only perturbations that have non commuting contributions of non-diagonalized spin components will couple the different bands and cause non trivial dynamics. Floquet topological insulators so far have been investigated mainly with respect to time reversal symmetry and particle hole symmetry protecting the topology. We are not aware of a crystalline Floquet topological insulator, which would be the quantum system in closest analogy to our system. Due to the lattice symmetry in our colloidal system we have a variety of different axes around which the perturbing external field may be wound. The reason for this is the multi-fold lattice symmetry that causes multiple stable points in the absence of a perturbing external field. In contrast to the quantum systems we have a richer variety of driving loops that can wind around alternative points of control space.

We should also mention that the dynamics of our colloidal system occurs in direct space not in reciprocal space. Direct space is an affine lattice having no natural origin. Each unit cell is equivalent to any other unit cell. Floquet topological quantum systems operate in reciprocal space where we can distinguish the first Brillouin zone from all the higher order Brillouin zones. For example in a hexagonal lattice the  $\Gamma$ -point in reciprocal space plays a different role than the  $K$ -points, while in our affine three-fold lattice all high symmetry points are equivalent and cause

lattice symmetries to have different effects in our colloidal system than in quantum systems.

Finally our system is dissipative causing irreversible relaxation processes to contribute to the dynamics. These irreversible processes can be rendered unimportant only on the stationary manifold *via* the adiabatic driving, but not on the paths of steepest descent. This is causing the non-time reversible ratchet processes that have no analogue in the topological quantum systems.

## 7 Conclusions

Paramagnetic and diamagnetic colloids above a magnetic pattern can be transported by modulating the potential with time dependent homogeneous external fields. If such modulation loops wind around specific points (fence points for the two- and four-fold symmetries, bifurcation points for the three- and six-fold symmetry) or pass through fence segments (three- and six-fold symmetry) in control space the topologically trivial modulation can be translated into non trivial motion of colloids. A summary of the relevant points and segments is shown as stereographic projection of control space for lattices of  $C_2$ ,  $C_4$ ,  $S_6$ -like, and  $C_6$ -like symmetry in Fig. 26. It shows the deep connection between symmetry and topology since all objects are completely different for the various symmetries. The lattice symmetry determines the transport modes, which are possible along the primitive lattice vectors.

Modulation loops can be sorted into topologically equivalent classes, according to their winding around those points and/or by the sequence of segment crossings. All modulation loops

belonging to the same class induce motion in the same direction, which makes the transport very robust against perturbations. Noise in the pattern only affects the less robust features of the transport while it doesn't alter its topological class.

On top of  $C_2$ - and the  $C_4$ -symmetric patterns para- and diamagnets are adiabatically transported into the same direction. In contrast above 3-fold and 6-fold symmetric patterns both types of particles can be transported into independent directions and the motion happens either adiabatically or *via* irreversible ratchets.

Classes of modulation loops causing transport modes into one direction cluster around the adiabatic paths. Ratchet modulation loops are topological protected by their neighboring adiabatic loops and hence transport into the same direction. The whole variety of possible transport is described by a set of topological invariants, which are winding numbers around the holes of the stationary surfaces  $\mathcal{M}$ .

The robustness of the topological transport can be used to transport a collection of colloids with a broad distribution of properties, such as size-polydispersity without dispersion. This is a clear advantage over other collective transport methods such as thermal ratchets, external gradients and active motion. The possibility of independent motion of paramagnets and diamagnets facilitates other applications such as guiding chemical reactions and assembly.<sup>20</sup>

## A Appendix

### A.1 Three fold symmetric stationary manifolds

In Fig. 27–31 we give a high resolution view of  $\mathcal{C}$ ,  $\mathcal{A}$ , and  $\mathcal{M}$  of the three-fold symmetric patterns at five different values of  $\phi$ , where we explain specific details in one of the figures each. These details apply to all different phases if not stated otherwise. The positions of the six gates in each space is explained in Fig. 27 and remains the same throughout the rest of the figures. In Fig. 28 we show the color coding of the areas in  $\mathcal{C}$  as well as the color coding shared between  $\mathcal{M}$  and  $\mathcal{A}$ . The poles of  $\mathcal{C}$  have  $2 \times 6$  preimages in  $\mathcal{M}$  that all lie on the central axis of  $\mathcal{M}$  either on a pole of a hemispherical cap or at the apex or base of the three central holes. When projecting  $\mathcal{M}$  into  $\mathcal{A}$  the poles on the hemispheres fall onto the three-fold symmetric points of  $\mathcal{A}$ , while the saddle point poles of  $\mathcal{M}_0$  in the three central holes are expelled in the surroundings of  $\mathbf{x}_{\mathcal{A},2}$ . The topological transition happens in Fig. 27. Two  $\mathcal{B}_0$  bifurcation points (pseudo bifurcation points) one from a satellite and one from a polar fence (polar pseudo fence) annihilate when the satellite excess area coalesces with the polar excess area at the ends of the full (dashed) arrows. Since only the lower half of  $\mathcal{M}$  is projected into  $\mathcal{A}$  there occur two cuts in the brown and red tropical regions of  $\mathcal{M}_0$ . The cut in  $\mathcal{M}$  and its projection into  $\mathcal{A}$  is shown in Fig. 31. The cut in  $\mathcal{A}$  circles twice around  $\mathbf{x}_{\mathcal{A},2}$  and around  $\mathbf{x}_{\mathcal{A},3}$  and twists each of the six times it passes a gate thereby alternating between the lower half lying inside and outside the cut. The cuts in the other figures are topologically equivalent to those in Fig. 31. The projection of areas in  $\mathcal{M}$  into  $\mathcal{C}$  preserves the

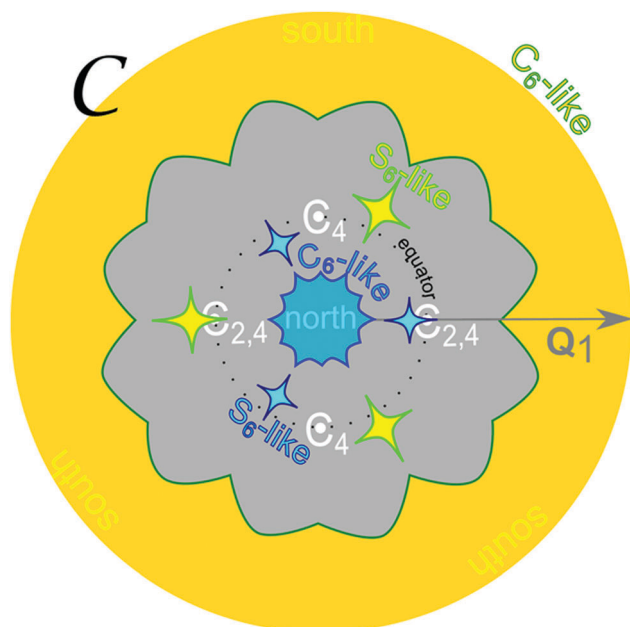


Fig. 26 Stereographic projection of control space with all relevant objects for the lattices of different symmetry. White circles are relevant for both paramagnets and diamagnets while green fences are relevant for the paramagnets only and blue fences are relevant for diamagnets only.

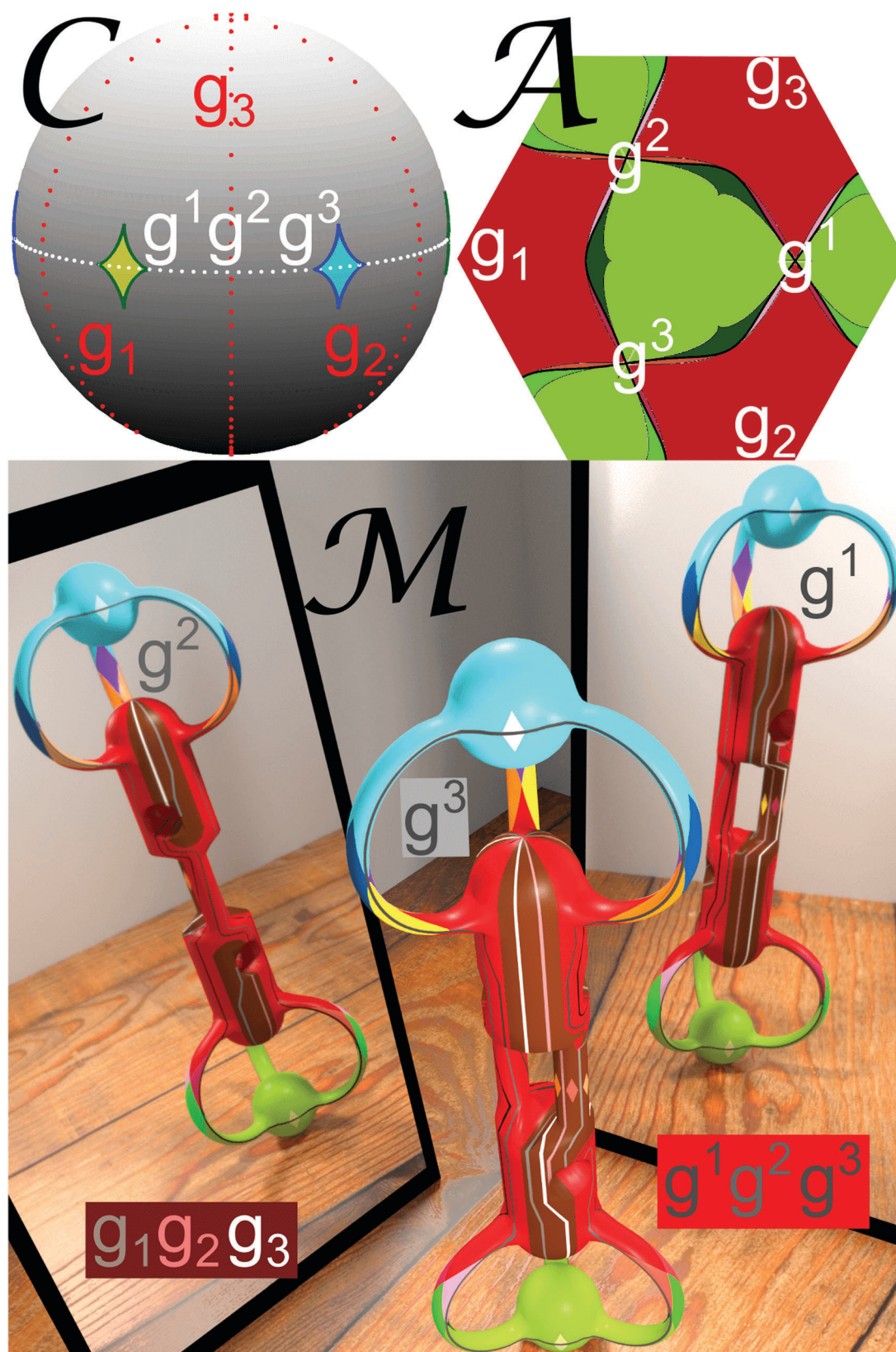


Fig. 27 Universal topology of  $\mathcal{C}$ ,  $\mathcal{A}$  and  $\mathcal{M}$  for a pattern with  $S_6$  symmetry ( $\phi = \pi/6$ ). We have marked the six gates  $g_1$ ,  $g_2$ ,  $g_3$ ,  $g^1$ ,  $g^2$ ,  $g^3$  that are projected into the six gate points in  $\mathcal{A}$ . On  $\mathcal{M}$  the upper gates  $g^1$ ,  $g^2$ ,  $g^3$  travel on the handles while the lower gates  $g_1$ ,  $g_2$ ,  $g_3$  pass through polar regions that will become isolated in the  $S_6$ -like case.

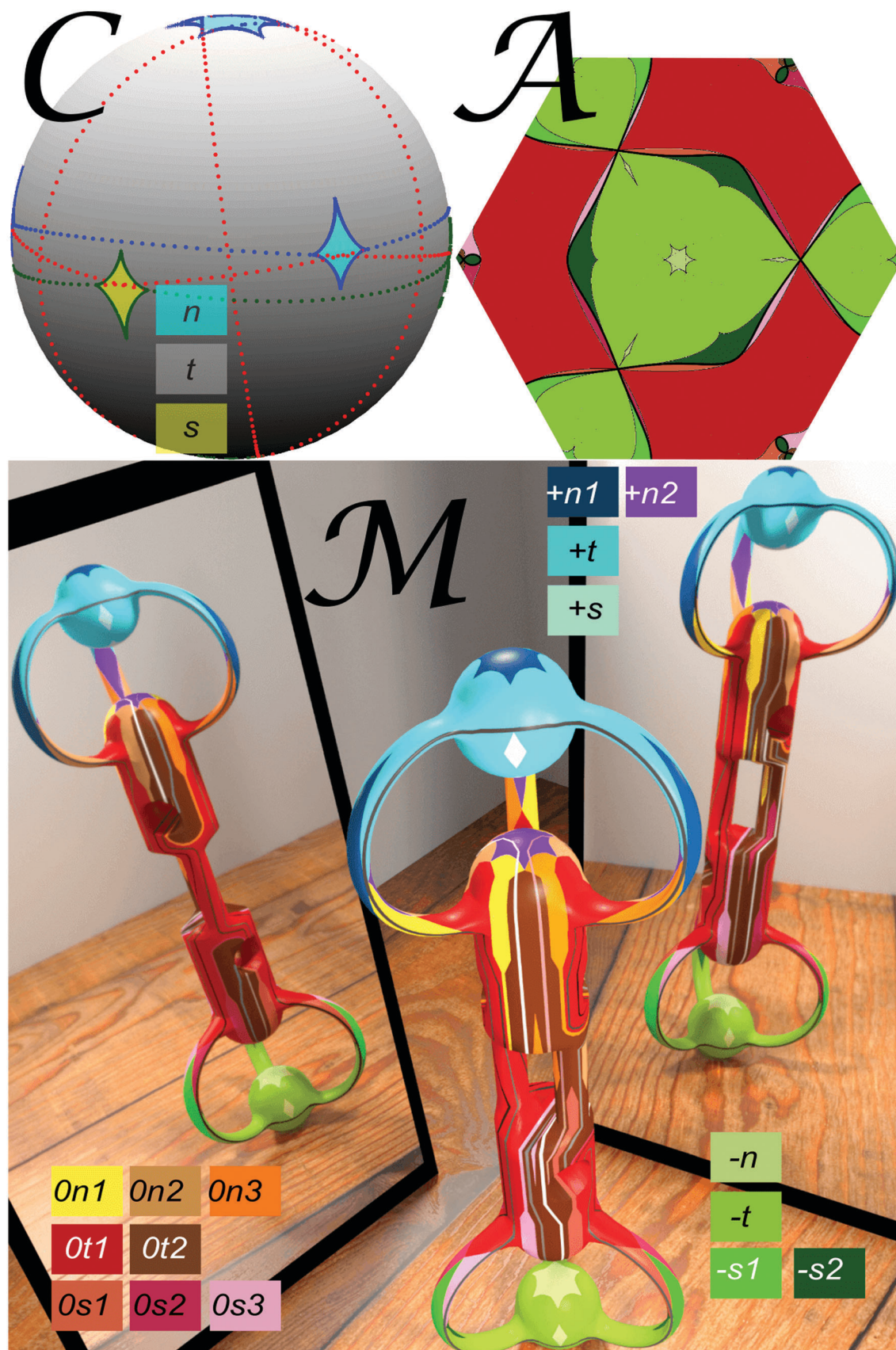


Fig. 28 Universal topology of  $\mathcal{C}$ ,  $\mathcal{A}$  and  $\mathcal{M}$  for a pattern with  $S_6$ -like symmetry ( $\phi = 5\pi/36$ ) together with color codes for the areas of  $\mathcal{C}$  and the shared color codes of  $\mathcal{M}$  and  $\mathcal{A}$ . The coloring of the gates is the same as in Fig. 27.

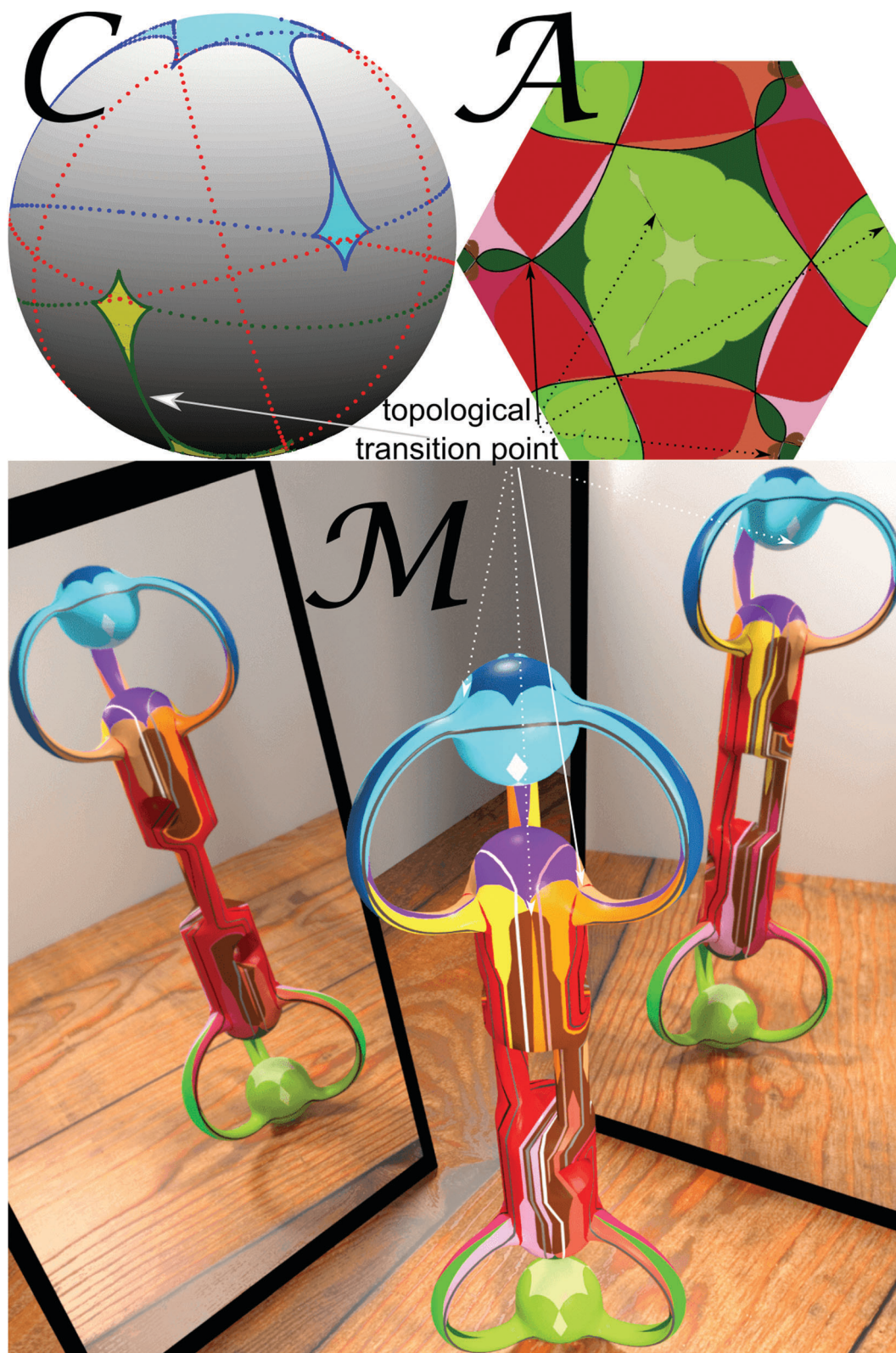


Fig. 29 Universal topology of  $\mathcal{C}$ ,  $\mathcal{A}$  and  $\mathcal{M}$  for a pattern at the transition from  $S_6$ -like to  $C_6$ -like symmetry ( $\phi_c = \pi/9$ ) with gates colored similar to Fig. 27. Two  $B_0$  (pseudo) bifurcation points from two (pseudo) fences annihilate at the topological transition points at the solid (dashed) arrows where the satellites merge with the polar excess areas.

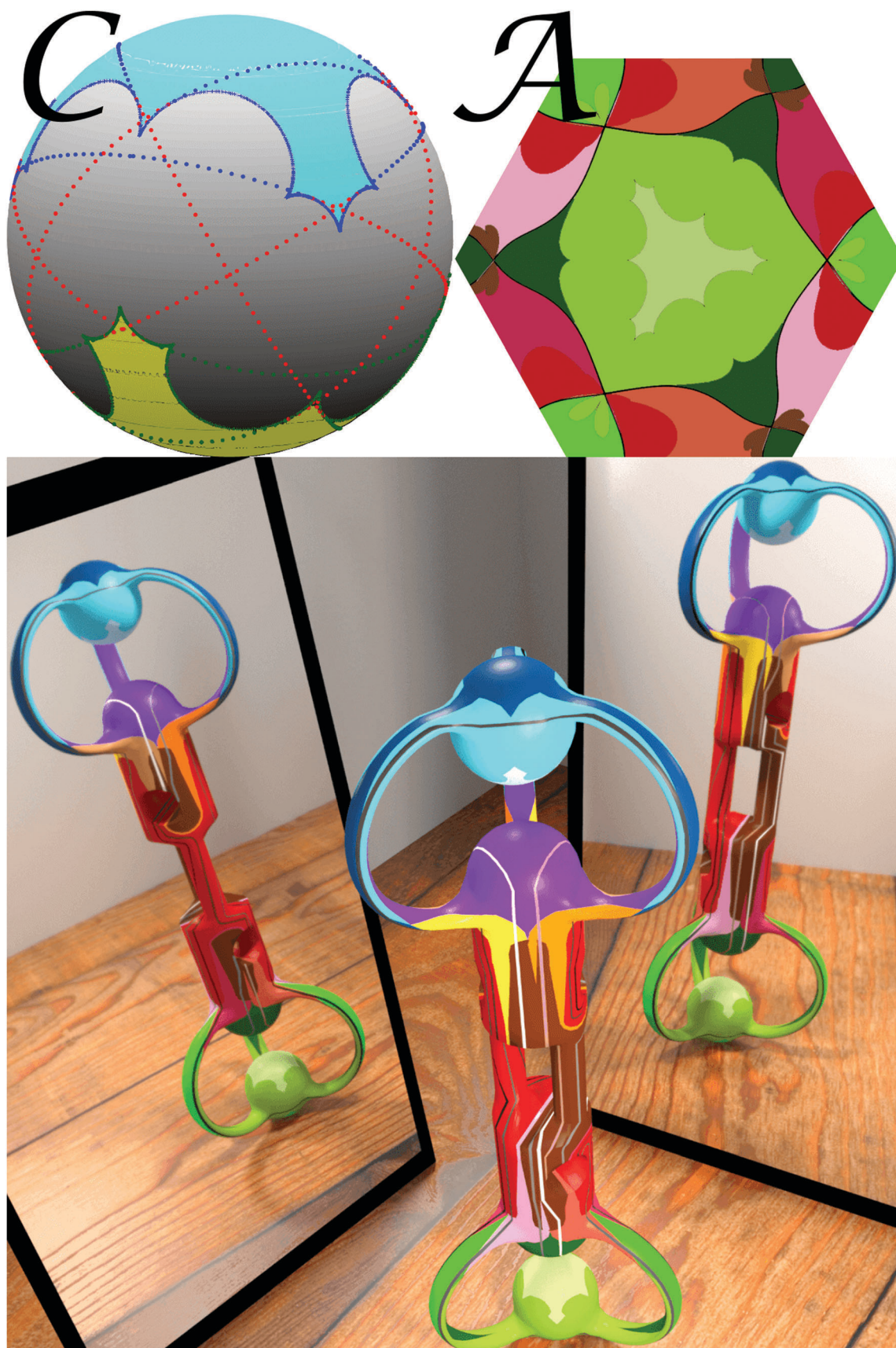


Fig. 30 Universal topology of  $\mathcal{C}$ ,  $\mathcal{A}$  and  $\mathcal{M}$  for a pattern with  $C_6$ -like symmetry ( $\phi = \pi/18$ ).

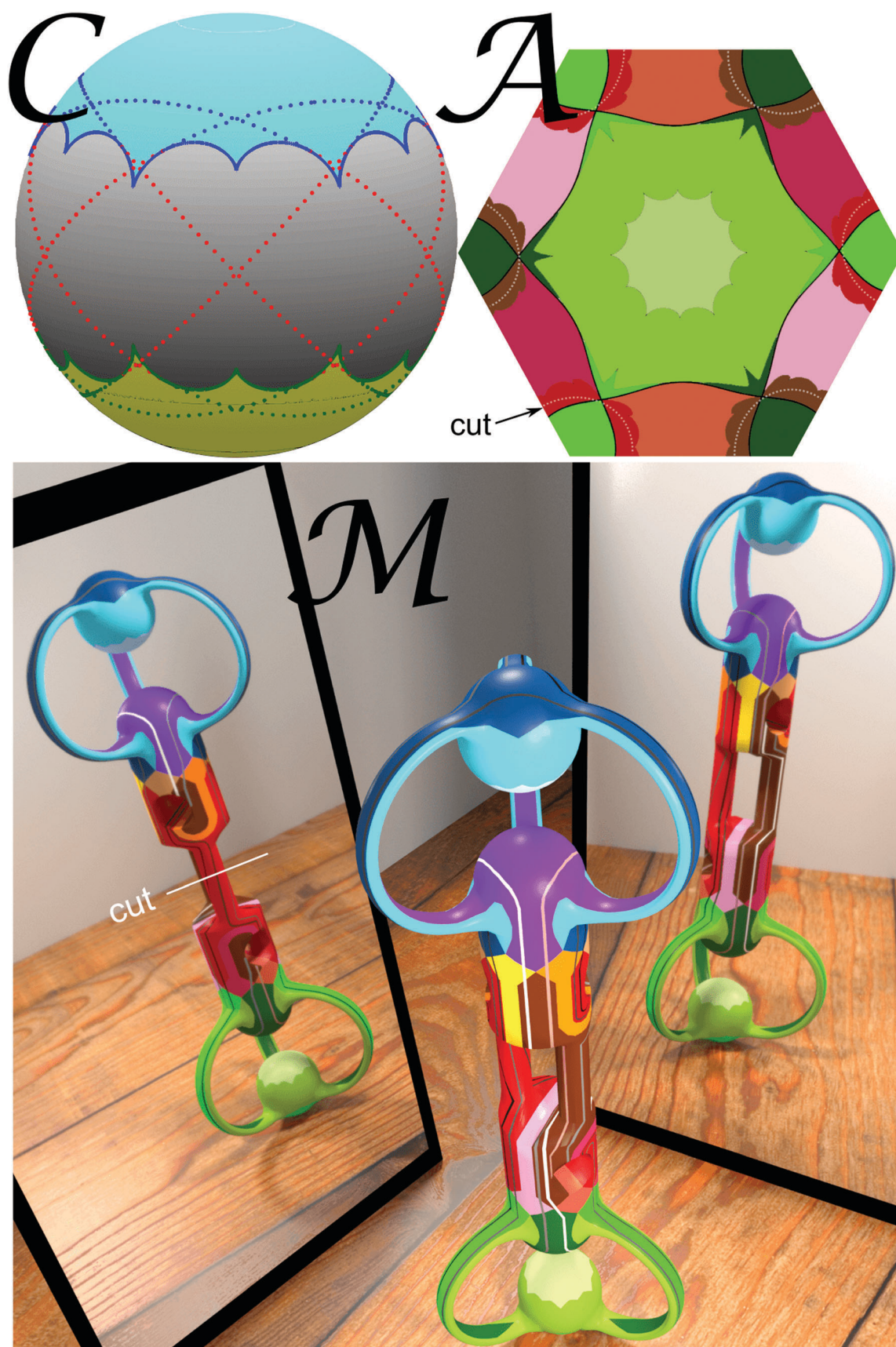


Fig. 31 Universal topology of  $C$ ,  $A$  and  $M$  for a pattern with  $C_6$  symmetry ( $\phi = 0$ ). We have marked the cut in  $A$  that is the projection of the boundary between the projected lower half of  $M$  and the upper half.

orientation of half the areas and switches sign for the others. Each time one passes a pseudo fence that is connected to a bifurcation point one switches the orientation of the projection in  $\mathcal{C}$ . The orientation of the projection from  $\mathcal{M}$  into  $\mathcal{A}$  switches sign when we pass from one side of the gate to the other side. The southern excess region south of the gates  $g_{i-}^j$  ( $g_{i-}$ ) in  $\mathcal{C}$  switches orientation when its preimages in  $\mathcal{M}_-$  are mapped into the bright (dark) green regions around  $\mathbf{x}_{A,3}$  (around  $\mathbf{x}_{A,2}$ ) in  $\mathcal{A}$ .

## A.2 Lithographic magnetic structures

Magnetic patterns with the desired symmetry have been created by 10 keV He-ion bombardment induced magnetic patterning of magnetic multilayer structures with perpendicular magnetic anisotropy<sup>49,54</sup> using a home-built ion source for 5–30 keV He ions.<sup>55</sup> First, the layer system  $\text{Ti}^{4\text{nm}}/\text{Au}^{60\text{nm}}/[\text{Co}^{0.7\text{nm}}/\text{Au}^{1\text{nm}}]_5$  with  $M_s$  of  $1420 \text{ kA m}^{-1}$  was fabricated by DC magnetron sputter deposition on a silicon substrate.<sup>56,57</sup> The sample's magnetic properties were characterized by polar magneto-optical Kerr effect magnetometry, possessing an initial coercive field of  $19.5 \pm 0.5 \text{ kA m}^{-1}$ . The magnetic domain structure was introduced by a local change of the sample's coercive field *via* 10 keV He ion bombardment through a shadow mask with an ion fluency of  $1 \times 10^{15}$  Ions per  $\text{cm}^2$ . Here, the geometry of the mask coincides with the desired four-fold symmetric, three-fold symmetric, or phase gradient pattern with a period length of  $7 \mu\text{m}$  (Fig. 2). The mask locally prevents the He ions to penetrate into the layer system.<sup>54</sup> In the uncovered areas, however, ion bombardment leads to a decrease of the perpendicular magnetic anisotropy and hence, the coercive field, primarily due to defect creation at the interfaces of the [Co/Au] multilayer structure.<sup>48,50</sup> In preliminary experiments, the decrease of the coercive field was characterized *via* polar magneto-optical Kerr effect magnetometry and determined to be  $6.5 \pm 0.5 \text{ kA m}^{-1}$ . The shadow mask was prepared *via* UV lithography on top of the sample. For this purpose, the sample was first spin coated with a photo-resist layer of AZ nLOF 2070 (MicroChemicals, AZ nLOF 2070 diluted with AZ EBR, ratio 4 : 1) with an average layer thickness of  $2 \mu\text{m}$  as determined from atomic force microscopy measurements. The lithographic structure was introduced by UV exposure through a structured chromium hard mask and subsequent development in AZ 826 MIF (MicroChemicals) to remove the unexposed parts of the resist. After ion bombardment without external magnetic fields applied during the process, the sample was first treated with 1-methyl-2-pyrrolidone for 24 h at  $80 \text{ }^\circ\text{C}$ , than ultrasonicated for 1 minute and finally cleaned with acetone and isopropanol. Due to the thickness  $t = 3.5 \text{ nm}$  of the magnetic layer, which is small in comparison to the wavelength of our structures ( $tQ < 1$ ), the pattern magnetic field on top of the lithographic pattern is attenuated to  $H^P = M_s \cdot t \cdot Q$  in comparison to the value  $H^P = M_s$  of a thick ( $tQ > 1$ ) garnet film.

## A.3 Definitions

**Action space:** the plane  $z = \text{const}$ , where the colloidal particles move. Due to the periodicity different unit cells can be identified with each other which folds action space into a torus.

**Adiabatic motion:** a motion enslaved by the external modulation, possible when one preimage in  $\mathcal{M}$  of a modulation loop in  $\mathcal{C}$  lies in  $\mathcal{M}_-$ .

**Allowed regions:** projection of the minimum/maximum sections of  $\mathcal{M}$  into  $\mathcal{A}$ .

**Bifurcation points:** bifurcation points on  $\mathcal{M}$  and on  $\mathcal{A}$  are crossings of fences with pseudo fences. In  $\mathcal{C}$  the bifurcation points are cusps of the fence. Bifurcation points exist for the three- and six-fold pattern not for the two- and four-fold pattern.

**Control space:** the endpoints of the external magnetic field of constant magnitude, a sphere.

**Equator:** the boundary between the two hemispheres in control space excluding fence points. The equators in  $\mathcal{M}$  are the preimages of the equator in  $\mathcal{C}$  of the projection from  $\mathcal{M}$  onto  $\mathcal{C}$ . The equators are relevant for the two-fold pattern, where there are no gates.

**Excess area:** a connected set of points in  $\mathcal{C}$  with higher multiplicity.

**Fence:** the fence in  $\mathcal{M}$  is the boundary between minima (or maxima) and the saddle points on  $\mathcal{M}$ . We use the same names for its projection into control and action space. Fences on  $\mathcal{M}$  and on the torus  $\mathcal{A}$  are closed lines. Fences on  $\mathcal{C}$  are points for the two- and four-fold symmetric pattern and lines for the three- and six-fold symmetric pattern.

**Forbidden regions:** projection of the saddle point regions of  $\mathcal{M}$  into  $\mathcal{A}$ . Allowed and forbidden regions are disjoint areas in  $\mathcal{A}$  for all but the two-fold patterns.

**Gates:** a gate in  $\mathcal{A}$  is a crossing point of two fences in  $\mathcal{A}$ . Gates exist for the three-, four-, and six-fold pattern not for the two-fold pattern. The preimage in  $\mathcal{M}$  of a gate in  $\mathcal{A}$  of the projection from  $\mathcal{C} \otimes \mathcal{A}$  onto  $\mathcal{A}$  is the gate (a closed line) on  $\mathcal{M}$ . The projection of the gate in  $\mathcal{M}$  onto  $\mathcal{C}$  is the gate in  $\mathcal{C}$ . A gate in  $\mathcal{C}$  is a grand circle.

**Irrelevant fence:** a fence that has no  $\mathcal{B}_+$  and no  $\mathcal{B}_-$  bifurcation points.

**Lemniscate:** a preimage in  $\mathcal{M}$  of a modulation loop in  $\mathcal{C}$  that is not a set of loops in  $\mathcal{M}$ .

**Modulation loop:** a loop in  $\mathcal{C}$ .

**Multiplicity:** the multiplicity of a point  $H_{\text{ext}} \in \mathcal{C}$  is the number of preimages  $(H_{\text{ext}}, x_A) \in \mathcal{M} \subset \mathcal{C} \otimes \mathcal{A}$  mapped from  $\mathcal{M}$  onto  $H_{\text{ext}} \in \mathcal{C}$  by the projection onto control space.

**Non-time reversible ratchet:** a ratchet motion that follows an open path when playing a palindrome modulation loop.

**Northern hemisphere:** the northern hemisphere are simply connected regions on  $\mathcal{C}$  and on  $\mathcal{M}$  with  $H_{z,\text{ext}} > 0$ . A similar definition holds for the southern hemisphere.

**Palindrome modulation loop:** a loop in  $\mathcal{C}$  consisting of two loops that are the inverse of each other.

**Path:** a path is a directed segment of a modulation loop.

**Phase space** the (multiply connected) product space of control space and action space and thus the product of a sphere and a torus.

**Pseudo bifurcation points:** pseudo bifurcation points in  $\mathcal{M}$  are preimages of the bifurcation points in  $\mathcal{C}$  that are not bifurcation points. Pseudo bifurcation points exist in three- and six-fold symmetric patterns. Pseudo bifurcation points in  $\mathcal{A}$  are

the projection of the pseudo bifurcation points in  $\mathcal{M}$ . Pseudo bifurcation points in  $\mathcal{M}$  and in  $\mathcal{A}$  are located at cusps of the pseudo fences.

**Pseudo fence:** a line in  $\mathcal{M}$  different from the fence in  $\mathcal{M}$  that is projected onto the fence in  $\mathcal{C}$ . Pseudo fences are closed lines in  $\mathcal{M}$  and  $\mathcal{A}$  that exist for the three- and six-fold symmetric pattern not the universal two- and four-fold symmetric pattern.

**Ratchet motion:** a motion where the adiabatic motion is interrupted by jumps following the intrinsic dynamics.

**Reduced control space:** the cut of control space with the space spanned by the single reciprocal lattice vector  $\mathbf{Q}_1$  of the two-fold pattern and the normal vector  $\mathbf{n}$ .

**Satellites:** excess areas for the  $S_6$ -like pattern that merge with their polar parent excess area upon the topological transition to a  $C_6$ -like pattern.

**Stationary manifold:** a two dimensional manifold in phase space, where the action gradient of the colloidal potential vanishes.

**Time reversible ratchet:** a ratchet motion that follows a closed path when playing a palindrome modulation loop.

**12-Network:** the three-fold symmetric pattern has three different points per unit cell with three-fold rotation symmetry. The straight lines between the first two points define the 12-network. Similar definitions hold for the 23-network and the 31-network.

## Acknowledgements

J. B and A. T. acknowledge support by a Ghana MOE – DAAD joined fellowship and a University of Kassel PhD fellowship respectively.

## References

- M. Z. Hasan and C. L. Kane, Colloquium: topological insulators, *Rev. Mod. Phys.*, 2010, **82**, 3045–3067.
- S.-Q. Shen, *Topological insulators: Dirac equation in condensed matters*, Springer Science, and Business Media (2013).
- C.-K. Chiu, J. C. Y. Teo, A. P. Schnyder and S. Ryu, Classification of topological quantum matter with symmetries, *Rev. Mod. Phys.*, 2016, **88**, 035005.
- L. Fu, Topological crystalline insulators, *Phys. Rev. Lett.*, 2011, **106**, 106802.
- T. H. Hsieh, H. Lin, J. Liu, W. Duan, A. Bansil and L. Fu, Topological crystalline insulators in the SnTe material class, *Nat. Commun.*, 2012, **3**, 982.
- P. Dziawa, B. J. Kowalski, K. Dybko, R. Buczko, A. Szczerbakow, M. Szot, E. Lusakowska, T. Balasubramanian, B. M. Wojek, M. H. Berntsen, O. Tjernberg and T. Story, A topological crystalline insulator states in  $\text{Pb}_{1-x}\text{Sn}_x\text{Se}$ , *Nat. Mater.*, 2012, **11**, 1023–1027.
- R.-J. Slager, A. Mesaros, V. Juricic and J. Zaanen, The space group classification of topological band-insulators, *Nat. Phys.*, 2013, **9**, 98–102.
- X.-J. Liu, J. J. He and K. T. Law, Demonstrating lattice symmetry protection in topological crystalline superconductors, *Phys. Rev. B: Condens. Matter Mater. Phys.*, 2014, **90**, 235141.
- G. van Miert, C. M. Smith and C. Morai, Dirac cones beyond the honeycomb lattice: a symmetry-based approach, *Phys. Rev. B: Condens. Matter Mater. Phys.*, 2016, **93**, 035401.
- T. Kitagawa, E. Berg, M. S. Rudner and E. Demler, Topological characterization of periodically driven quantum systems, *Phys. Rev. B: Condens. Matter Mater. Phys.*, 2010, **82**, 235114.
- M. S. Rudner, N. H. Lindner, E. Berg and M. Levin, Anomalous Edge States and the Bulk-Edge Correspondence for Periodically Driven Two-Dimensional Systems, *Phys. Rev. X*, 2013, **3**, 031005.
- D. Thouless, M. Kohmoto, M. P. Nightingale and M. den Nijs, Quantized Hall Conductance in a Two-Dimensional Periodic Potential, *Phys. Rev. Lett.*, 1982, **49**, 405–408.
- C. L. Kane and T. C. Lubensky, Topological boundary modes in isostatic lattices, *Nat. Phys.*, 2014, **10**, 39–45.
- J. Paulose, B. G. Chen and V. Vitelli, Topological modes bound to dislocations in mechanical metamaterials, *Nat. Phys.*, 2015, **11**, 153–156.
- M. C. Rechtsman, J. M. Zeuner, Y. Plotnik, Y. Lumer, D. Podolsky, F. Dreisow, S. Nolte, M. Segev and A. Szameit, Photonic Floquet topological insulators, *Nature*, 2013, **496**, 196–200.
- L. M. Nash, D. Kleckner, A. Read, V. Vitelli, A. M. Turner and W. T. M. Irvine, Topological mechanics of gyroscopic metamaterials, *Proc. Natl. Acad. Sci. U. S. A.*, 2015, **112**, 14495–14500.
- M. Xiao, G. Ma, Z. Yang, P. Sheng, Z. Q. Zhang and C. T. Chan, Geometric phase and band inversion in periodic acoustic systems, *Nat. Phys.*, 2015, **11**, 240–244.
- S. D. Huber, Topological mechanics, *Nat. Phys.*, 2016, **12**, 621–623.
- A. Murugan and S. Vaikuntanathan, Topologically protected modes in non-equilibrium stochastic systems, *Nat. Commun.*, 2017, **8**, 13881.
- J. Loehr, M. Loenne, A. Ernst, D. de las Heras and Th. M. Fischer, Topological protection of multiparticle dissipative transport, *Nat. Commun.*, 2016, **7**, 11745.
- D. de las Heras, J. Loehr, M. Loenne and Th. M. Fischer, Topologically protected colloidal transport above a square magnetic lattice, *New J. Phys.*, 2016, **18**, 105009.
- C. J. Olson, C. Reichhardt and F. Nori, Nonequilibrium dynamic phase diagram for vortex lattices, *Phys. Rev. Lett.*, 1998, **81**, 3757–3760.
- C. Reichhardt and F. Nori, Phase locking, devil's staircases, Farey trees, and Arnold tongues in driven vortex lattices with periodic pinning, *Phys. Rev. Lett.*, 1999, **82**, 414–417.
- A. B. Kolton, D. Domínguez and N. Grønbech-Jensen, Mode locking in ac-driven vortex lattices with random pinning, *Phys. Rev. Lett.*, 2001, **86**, 4112–4115.
- P. T. Korda, M. B. Taylor and D. G. Grier, Kinetically locked-in colloidal transport in an array of optical tweezers, *Phys. Rev. Lett.*, 2002, **89**, 128301.

- 26 T. Bohlein, J. Mikhael and C. Bechinger, Observation of kinks and antikinks in colloidal monolayers driven across ordered surfaces, *Nat. Mater.*, 2012, **11**, 126–130.
- 27 M. Ghodbane, E. C. Stucky, T. J. Maguire, R. S. Schloss, D. I. Shreiber, J. D. Zahn and M. L. Yarmush, Development and validation of a microfluidic immunoassay capable of multiplexing parallel samples in microliter volumes, *Lab Chip*, 2015, **15**, 3211–3221.
- 28 A. V. Arzola, M. Villasante-Barahona, K. Volke-Sepúlveda, P. Jákl and P. Zemánek, Omnidirectional Transport in Fully Reconfigurable Two Dimensional Optical Ratchets, *Phys. Rev. Lett.*, 2017, **118**, 138002.
- 29 H. Loewen, Particle-resolved instabilities in colloidal dispersions, *Soft Matter*, 2010, **6**, 3133–3142.
- 30 M. Driscoll, B. Delmotte, M. Youssef, S. Sacanna, A. Donev and P. Chaikin, Unstable fronts and motile structures formed by microrollers, *Nat. Phys.*, 2017, **13**, 375–379.
- 31 J. E. Martin and K. J. Solis, Fully alternating, triaxial electric or magnetic fields offer new routes to fluid vorticity, *Soft Matter*, 2015, **11**, 241–254.
- 32 P. Tierno, T. H. Johansen and Th. M. Fischer, Localized and delocalized motion of colloidal particles on a magnetic bubble lattice, *Phys. Rev. Lett.*, 2007, **99**, 038303.
- 33 P. Tierno, S. V. Reddy, M. G. Roper, T. H. Johansen and Th. M. Fischer, Transport and separation of biomolecular cargo on paramagnetic colloidal particles in a magnetic ratchet, *J. Phys. Chem. B*, 2008, **112**, 3833–3837.
- 34 M. P. N. Juniper, A. V. Straube, R. Besseling, D. G. A. Aarts and R. P. A. Dullens, Microscopic dynamics of synchronization in driven colloids, *Nat. Commun.*, 2015, **6**, 7187.
- 35 P. Tierno and A. V. Straube, Transport and selective chaining of bidisperse particles in a travelling wave potential, *Eur. Phys. J. E: Soft Matter Biol. Phys.*, 2016, **39**, 54.
- 36 C. R. Doering, W. Horsthemke and J. Riordan, Nonequilibrium fluctuation-induced transport, *Phys. Rev. Lett.*, 1994, **72**, 2984–2987.
- 37 M. N. Popescu, C. M. Arizmendi, A. L. Salas-Brito and F. Family, Disorder induced diffusive transport in ratchets, *Phys. Rev. Lett.*, 2000, **85**, 3321–3324.
- 38 P. Reimann, Brownian motors: noisy transport far from equilibrium, *Phys. Rep.*, 2002, **361**, 57–265.
- 39 S. Savelév, F. Marchesoni and F. Nori, Stochastic transport of interacting particles in periodically driven ratchets, *Phys. Rev. E: Stat., Nonlinear, Soft Matter Phys.*, 2004, **70**, 061107.
- 40 S. Köhler, J. Lehmann and P. Hänggi, Driven quantum transport on the nanoscale, *Phys. Rep.*, 2005, **406**, 379–443.
- 41 N. A. Sinitsyn, The stochastic pump effect and geometric phases in dissipative and stochastic systems, *J. Phys. A: Math. Theor.*, 2009, **42**, 193001.
- 42 L. Gao, M. A. Tahir, L. N. Virgin and B. B. Yellen, Multiplexing superparamagnetic beads driven by multi-frequency ratchets, *Lab Chip*, 2011, **11**, 4214–4220.
- 43 A. H. Bobeck, P. I. Bonyhard and J. E. Geusic, Magnetic bubbles—an emerging new memory technology, *Proc. IEEE*, 1975, **63**, 1176–1195.
- 44 B. D. Terris and T. Thomson, Nanofabricated and self-assembled magnetic structures as data storage media, *J. Phys. D: Appl. Phys.*, 2005, **38**, R199–R222.
- 45 Videos adfigure4.avi, adfigure10c.avi, adfigure11.avi, adfigure17b.avi, adfigure18b.avi, adfigure19.avi, adfigure20.avi, adfigure21b.avi, adfigure21d.avi, adfigure21e.avi, adfigure23.avi and adfigure24.avi corresponding to Fig. 4, 10c, 11, 17b, 18b, 19, 20, 21b, d, e, 23 and 24 are shown free of charge in the ESI†.
- 46 I. Bauer and F. Catanese, Generic lemniscates of algebraic functions, *Math. Ann.*, 1997, **307**, 417–444.
- 47 A. Jarosz, D. Holzinger, M. Urbaniak, A. Ehresmann and F. Stobiecki, Manipulation of superparamagnetic beads on patterned Au/Co/Au multilayers with perpendicular magnetic anisotropy, *J. Appl. Phys.*, 2016, **120**, 084506.
- 48 C. Chappert, H. Bernas, J. Ferré, V. Kottler, J.-P. Jamet, Y. Chen, E. Cambril, T. De-volder, F. Rousseaux, V. Mathet and H. Launois, Planar patterned magnetic media obtained by ion irradiation, *Science*, 1998, **280**, 1919–1922.
- 49 P. Kuświk, A. Ehresmann, M. Tekielak, B. Szymański, I. Sveklo, P. Mazalski, D. Engel, J. Kisielewski, D. Lengemann, M. Urbaniak, C. Schmidt, A. Maziewski and F. Stobiecki, Colloidal domain lithography for regularly arranged artificial magnetic out-of-plane monodomains in Au/Co/Au layers, *Nanotechnology*, 2011, **22**, 095302.
- 50 M. Urbaniak, P. Kuświk, Z. Kurant, M. Tekielak, D. Engel, D. Lengemann, B. Szymański, M. Schmidt, J. Aleksiejew, A. Maziewski, A. Ehresmann and F. Stobiecki, Domain-Wall Movement Control in Co/Au Multilayers by He<sup>+</sup>-Ion-Bombardment-Induced Lateral Coercivity Gradients, *Phys. Rev. Lett.*, 2010, **105**, 067202.
- 51 Let  $\mathbf{v}_0$  be an eigen vector of the Hesse matrix to the eigen value zero, i.e.  $\nabla_{\mathcal{A}} \nabla_{\mathcal{A}} U^* \cdot \mathbf{v}_0 = 0$ . Then a point on the fence in  $\mathcal{C} \otimes \mathcal{A}$  is a bifurcation point if it fulfills eqn (18) and (19) and the condition  $(\mathbf{v}_0 \cdot \nabla_{\mathcal{A}})^3 U^* = 0$ .
- 52 A. P. Ramirez, Geometrical frustration in magnetism, *Annu. Rev. Mater. Sci.*, 1994, **24**, 453–480.
- 53 N. H. Lindner, G. Refael and V. Galitski, Floquet topological insulator in semiconductor quantum wells, *Nat. Phys.*, 2011, **7**, 490–495.
- 54 A. Ehresmann, I. Koch and D. Holzinger, Manipulation of Superparamagnetic Beads on Patterned Exchange-Bias Layer Systems for Biosensing Applications, *Sensors*, 2015, **15**, 28854.
- 55 D. Lengemann, D. Engel and A. Ehresmann, Plasma ion source for *in situ* ion bombardment in a soft X-ray magnetic scattering diffractometer, *Rev. Sci. Instrum.*, 2012, **83**, 053303.
- 56 M. Tekielak, R. Gieniusz, M. Kisielewski, P. Mazalski, A. Maziewski, V. Zablotkii, F. Stobiecki, B. Szymański and R. Schäfer, The effect of magnetostatic coupling on spin configurations in ultrathin multilayers, *J. Appl. Phys.*, 2011, **110**, 043924.
- 57 J. Quispe-Marcato, B. Pandey, W. Alayo, M. A. de Sousa, F. Pelegrini and E. Baggio Saitovitch, Preferential orientation of magnetization and interfacial disorder in Co/Au multilayers, *J. Magn. Magn. Mater.*, 2013, **344**, 176–181.

## **P4 Macroscopic Floquet topological crystalline steel and superconductor pump**

Anna M. E. Rossi<sup>a</sup>, **Jonas Bugase<sup>a</sup>**, Thomas M. Fischer<sup>\*a</sup>

<sup>a</sup>Experimental Physics, Institute of Physics and Mathematics, Universität Bayreuth,  
95440 Bayreuth, Germany

**EPL,119**, (2017) 40001

**DIO:10.1209/0295-5075/119/40001**

Received 26<sup>th</sup> July, 2017, Accepted 28<sup>th</sup> Sept., 2017

---

### **My Contribution**

I designed, performed and analyzed the experiments for the superconductor pump and contributed to the writing of the manuscript together with Thomas M. Fischer and Anna M. E. Rossi. Anna M. E. Rossi conducted the experiments for the steel pump.





LETTER

# Macroscopic Floquet topological crystalline steel and superconductor pump

To cite this article: Anna M. E. B. Rossi *et al* 2017 *EPL* **119** 40001

View the [article online](#) for updates and enhancements.

## Related content

- [Topologically protected colloidal transport above a square magnetic lattice](#)  
Daniel de las Heras, Johannes Loehr, Michael Loenne et al.
- [Winding numbers of phase transition points for one-dimensional topological systems](#)  
Linhu Li, Chao Yang and Shu Chen
- [Observation of the two-dimensional reciprocal lattice by use of lattice grating sheets and a laser pointer](#)  
Takanori Tsutaoka, Tomohito Tokunaga, Takashi Umeda et al.

# Macroscopic Floquet topological crystalline steel and superconductor pump

ANNA M. E. B. ROSSI, JONAS BUGASE and THOMAS M. FISCHER<sup>(a)</sup>

*Experimental Physics, Institute of Physics and Mathematics, Universität Bayreuth - 95440 Bayreuth, Germany*

received 26 July 2017; accepted in final form 28 September 2017  
published online 30 October 2017

PACS 02.40.Pc – General topology  
PACS 03.65.Vf – Phases: geometric; dynamic or topological  
PACS 05.60.Cd – Classical transport

**Abstract** – The transport of a macroscopic steel sphere and a superconducting sphere on top of two-dimensional periodic magnetic patterns is studied experimentally and compared with the theory and with experiments on topological transport of magnetic colloids. Transport of the steel and superconducting sphere is achieved by moving an external permanent magnet on a closed loop around the two-dimensional crystal. The transport is topological, *i.e.*, the spheres are transported by a primitive unit vector of the lattice when the external magnet loop winds around specific directions. We experimentally determine the set of directions the loops must enclose for nontrivial transport of the spheres into various directions. We show that the loops can be used to sort steel and superconducting spheres. We show that the topological transport is robust with respect to the scale of the system and therefore speculate on its down scalability to the molecular scale.

Copyright © EPLA, 2017

**Introduction.** – Topological nontrivial matter is a class of material, where the response of the material to external perturbations only depends on the global properties not on the local properties of the material. Such properties are called topological invariants and they change in a discrete way, *i.e.*, a continuous change of the perturbation results in a discrete response of the material. Topological properties of matter play a fundamental role in electronic transport behavior of quantum solid state matter [1,2], in mesoscopic systems [3–8] and in macroscopic matter [9–12]. One important class of topological material are Floquet topological systems, where the material is subject to a time-periodic external perturbation that causes the pumping of excitations or quasi particles through the material. The topological pump effect [13] is usually protected by certain symmetries of the problem. Such symmetries include the point group symmetries of the lattice. As a consequence of the topologically nontrivial bulk pump process one obtains a bulk edge correspondence [14,15]. When one augments the voltage applied to a topological insulator, transient topological pumping of bulk electrons from one edge channel to the opposite edge sets in to restore a steady state with asymmetric filling of both edges.

In the current letter we demonstrate such a bulk pumping process with an intriguingly simple setup on a macroscopic scale. We have shown similar pumping with a very different mesoscopic colloidal system, where we also outline the theory of the pumping [8]. The colloidal system requires the use of complex magnetic patterns obtained via lithographic techniques [16]. The macroscopic system presented here in contrast is so simple that it can be easily rebuilt. We believe it to be the technologically simplest macroscopic example of a topological pump. Moreover the full dynamics, *i.e.*, that of the particle and that of the external field are easy to observe. The current work presents three macroscopic examples of topological magnetic crystals, with magnetic point symmetry protected Floquet transport properties of paramagnetic (soft magnetic) and diamagnetic (superconducting) spheres placed above the crystal. We experimentally determine regions of orientation around which we have to wind an external magnetic field to pump the spheres into certain directions. These regions turn out to strongly depend on the symmetry of the lattice.

**Steel pump setup.** – The system consists of a two-dimensional magnetic pattern of up- and down-magnetized domains creating a two-dimensional magnetic potential for the steel sphere above the pattern.

<sup>(a)</sup>E-mail: thomas.fischer@uni-bayreuth.de

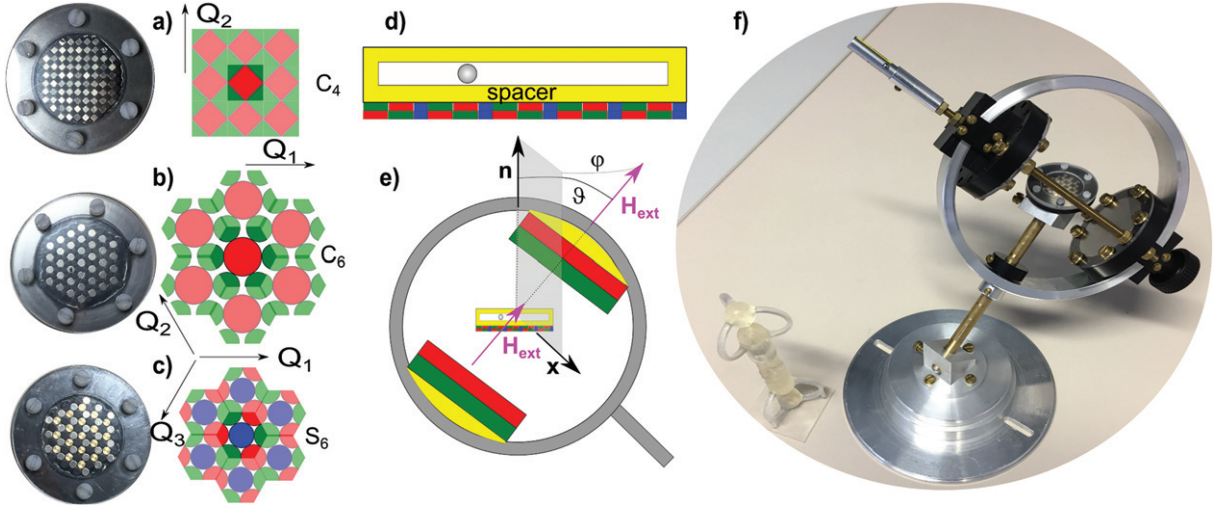


Fig. 1: (Color online) (a) Top view of the magnetic pattern of symmetry  $C_4$ , sample left and scheme right (b) symmetry  $C_6$  and (c) symmetry  $S_6$ . Silver areas in the sample (red areas in the scheme) are magnetized up and black (green) areas are magnetized down, respectively. Blue areas are nonmagnetic brass cylinders inserted for mechanical stability. One unit cell is emphasized in full colors. The vector  $Q_1$  is one of the primitive reciprocal lattice vectors. (d) Sideview of the pattern and the compartment holding the steel sphere. (e) Goniometer and external magnets surrounding the sample. (f) A photo of the setup.

The potential parametrically depends on the direction of a superposed external magnetic field. The steel sphere moves in this potential when we adiabatically modulate the potential by changing the direction of the external field.

Three two-dimensional magnetic patterns are built from an arrangement of NbB-magnets. The first crystal consists of magnetic cubes of side length  $d_1 = 2$  mm and remanence  $\mu_0 M_1 = 1.35$  T arranged in a fourfold symmetric  $C_4$  checkerboard square lattice of alternating up- and down-magnetized cubes (fig. 1(a)). The second, a hexagonal lattice (fig. 1(b)), consists of cylindrical magnets of diameters  $d_2 = 3$  mm and  $d_3 = 2$  mm, height  $h = 2$  mm and remanence  $\mu_0 M_2 = 1.19$  T and  $\mu_0 M_3 = 1.35$  T (respectively). The larger size  $d_2 = 3$  mm magnets are magnetized upwards and they are surrounded by six smaller size  $d_3 = 2$  mm magnets that are magnetized downwards and that touch the larger magnet. The primitive unit cell of the lattice is a sixfold symmetric  $C_6$  hexagon with corners centered within the smaller magnets. Each unit cell thus contains one large magnet and two smaller magnets. The third lattice (fig. 1(c)) is built from a hexagonally closed-packed arrangement of  $d_2 = 3$  mm diameter cylinders. The central cylinder (blue) is nonmagnetic brass, and the surrounding cylinders are NbB magnets of alternating upward and downward magnetization creating an improper sixfold  $S_6$  symmetry. All two-dimensional lattices have two primitive lattice vectors of the same length  $a_1 = a_2 = a = 2.82$  mm (square lattice),  $a = 4.33$  mm ( $C_6$  lattice), and  $a = 5.2$  mm ( $S_6$  lattice) and are metastable (the ground-state configuration of the magnet ensemble is a magnetic rod of magnets aligned along one axis) in zero external magnetic field. We fix the arrangement with an epoxy resin placed in the voids and the lateral

surroundings of the pattern. The pattern then is stable also in the presence of an external field. The crystals are put on a support and covered with a transparent PMMA spacer of thickness  $z = 1$ – $1.5$  mm (fig. 1(d)). The potential energy of the steel sphere can be decomposed into a discrete Fourier series of contributions from reciprocal lattice vectors. The Fourier series of the potential right above the pattern is the square of the Fourier series of the magnetization of the pattern augmented by the external field. As a function of the elevation the higher Fourier coefficients are attenuated more than Fourier coefficients with lower reciprocal vectors. At the experimental elevation only the universal contributions to the potential from the lowest nonzero reciprocal lattice vectors remain relevant. The purpose of the spacer is thus to render the potential universal such that only the symmetry of the pattern, not the details of the pattern are important. We place a steel sphere of diameter  $2r = 1$  mm on top of the spacer and create a closed but transparent compartment around the steel sphere. The topological magnetic crystal with the steel sphere on top is placed in the center of a goniometer set up at an angle of 45 degrees to ensure that relevant motion is not affected by the restrictions of motion of the goniometer (fig. 1(e) and (f)) caused by the support. The goniometer holds two NbB-magnets of diameter  $d_{ext} = 60$  mm, thickness  $t_{ext} = 10$  mm and remanence  $\mu_0 M_{ext} = 1.28$  T aligned parallel to each other at a distance  $2R = 120$  mm and creating an external magnetic field  $\mu_0 H_{ext} = 45$  mT penetrating the two-dimensional crystal and the steel sphere. The magnetic field gradients  $\nabla H_{ext} \approx M_{ext} t_{ext} d_{ext}^2 / R^4$  of the external field at the position of the steel sphere is at least two orders of magnitude smaller than the field gradients of the magnetic field of the crystal  $\nabla H_{int} \approx M/a$ . The two external magnets can be oriented to produce an arbitrary

direction of the external magnetic field with respect to the crystal. A laser pointer pointing along  $\mathbf{H}_{ext}$  is mounted on the goniometer creating a stereographic projection of the instantaneous external magnetic field direction on a recording plane.

**Topologically nontrivial transport loops.** – We reorient the external magnets by moving along a closed reorientation loop that starts and ends at the same initial orientation. The steel sphere responds to the reorientation loop with a motion that starts at one position of the lattice and ends at a final position. A topological trivial motion of the steel sphere is a motion where the steel sphere responds to a closed reorientation loop with a closed loop on the lattice. Not every closed reorientation loop causes a trivial response of the steel sphere. There are topologically nontrivial trajectories, where the steel sphere trajectory ends at a position differing from the initial position by one vector of the lattice.

The theory developed in [8] sorts the modulation loops of the external field on the sphere of external magnetic field orientation into classes that transport into different directions. Additionally the theory distinguishes adiabatic and ratchet modulation loops. For adiabatic loops the speed of the particle is enslaved to the adiabatic speed of modulation during the entire modulation loop. For ratchet modulation loops the particles perform jumps with an intrinsic speed that is uncorrelated with the speed of modulation at particular orientations of the external field. In the adiabatic motion the particle hence moves with the potential minimum at all times, while in a ratchet it jumps to a new minimum if the old minimum disappears at a critical external magnetic field. On the sphere of orientation these different modulation loops can be distinguished by their winding number around specific objects (points, lines or areas). The dimension and position of these objects depends on the symmetry of the lattice.

Experimentally we choose a collection of different non-self-intersecting reorientation loops and measured the corresponding displacement of the steel sphere. Each non-self-intersecting reorientation loop cuts the sphere of orientations that we call the control space into two areas. One of the areas is circulated by the loop in the positive sense the other in the negative sense. We define the intersection of all positive areas of loops causing the same net transport of the steel sphere as the positive common area of this transport direction. Similarly we can define the negative common area of the same transport directions. If we find a loop that cuts through the common area and reproducibly transports into the same direction, we have found a smaller common area. By performing experiments with lots of different loops we eventually approach the smallest common area. In this way we can map the common areas without relying on the theoretical predictions.

*Fourfold symmetric pattern.* In fig. 2(a) we show the common area (yellow) determined in this way for the transport into the  $\mathbf{n} \times \mathbf{Q}_1$ -direction for the fourfold

symmetric pattern. The common area is a rectangle centered around the primitive reciprocal vector  $-\mathbf{Q}_1$  of the lattice. Whenever we wind the modulation loop around the common area in a way that does not touch the area, the result is the same nontrivial transport as shown in fig. 2(b). Two modulation loops with similar winding number around the common area are shown in fig. 2(a). The resulting transport over a period is the same for both loops which shows that the transport is protected against perturbations of the modulation. Entering the common area leads to a statistical trivial or nontrivial response transport direction of the steel sphere (the transport direction is no longer reproducible). The sphere passes from the up-magnetized region toward the down-magnetized regions or vice versa when the loop crosses the gates (dark and bright green circles). In the experiments we observe a hysteresis, *i.e.*, the gate in control space is positioned at the bright green circles of the southern hemisphere when the external field moves from north toward the south and at the dark green circles of the northern hemisphere for the opposite direction. The region of the hysteresis is shown as the green area in control space. Note that similar common areas repeat every  $2\pi/4$  along the equator because of the  $C_4$ -symmetry. In previous work [8] we have computed the theoretical position of the common area as well as the position of the gates. Theoretically the common area is just one point, the  $-\mathbf{Q}_1$ -direction, and the gate is a (green) line on the equator showing no hysteresis. In fig. 2(b) we show the trajectory of the steel sphere on the fourfold lattice subject to the purple loop in fig. 2(a) encircling the reciprocal vector  $-\mathbf{Q}_1$  in the mathematical positive sense. Movies of the motion to both fig. 2 and fig. 3 can be found in the supplementary material (SM) as videos `Fig2b.avi`, `Fig2d.avi` and `Fig2f.avi` corresponding to figs. 2(b), (d) and (f). The first two movies were done by following a predefined path on a screen with the laser pointer of the goniometer. The last movie is done by moving the external magnet by hand showing the robustness of the motion with respect to deviations of the modulation path. Videos `Fig3b.avi`, `Fig3d.avi` and `Fig3f.avi` corresponding to figs. 3(b), (d) and (f) show the different behavior of steel and superconducting spheres when immersed into liquid nitrogen.

*Improper sixfold symmetric pattern.* In fig. 2(c) we show the control space of the  $S_6$ -symmetric pattern. Non-trivial transport into the  $\mathbf{n} \times \mathbf{Q}_1$ -direction occurs if we wind the loop around the yellow common area. We call the borders of the yellow area the fence. A new feature of the  $S_6$ -symmetric pattern is that the transport is still predictable if we enter and exit the yellow area with a loop through fence segments marked in blue and red. A loop exiting the common area in the north (south) has the same result as a common-area-avoiding loop with the same winding number around the cusp point joining the two blue (red) segments of the fence. Although the transport direction of those common-area-passing loops is the same

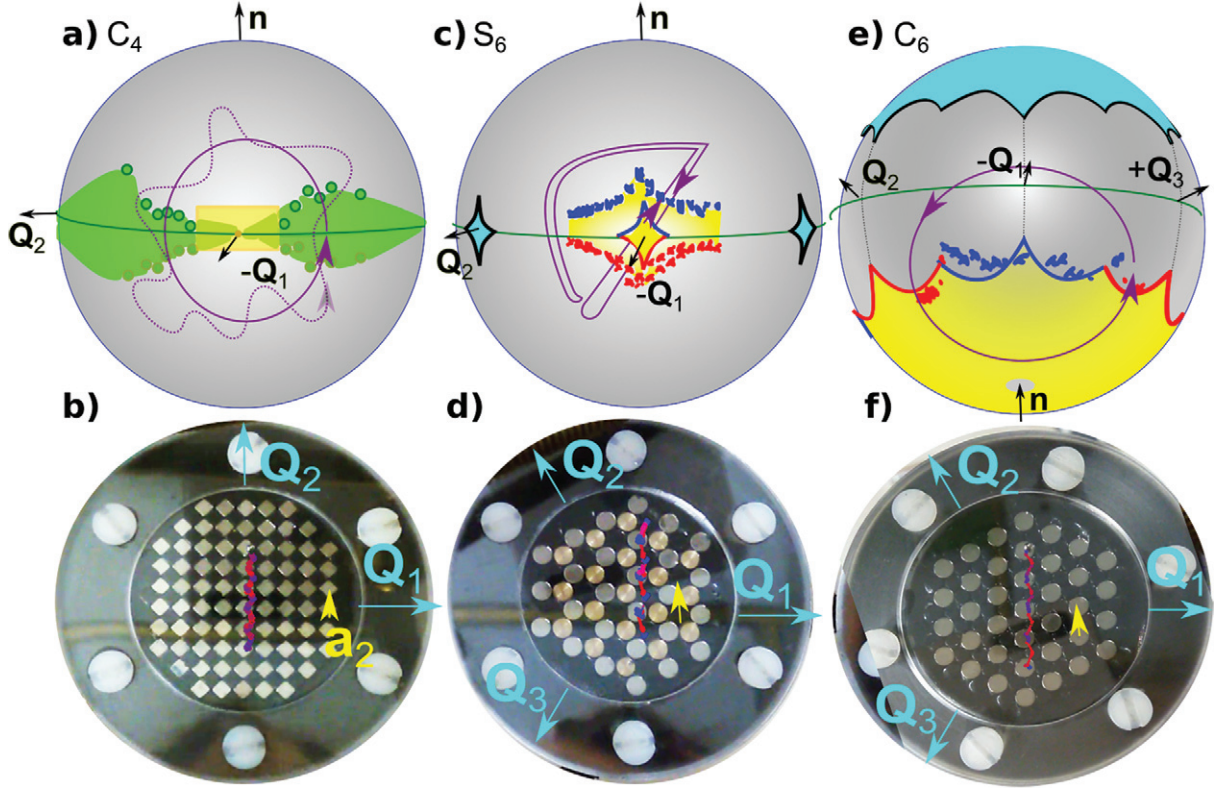


Fig. 2: (Color online) (a) Control space of the  $C_4$ -symmetric lattice. The  $-\mathbf{Q}_1$ -direction of control space is opposite to the reciprocal lattice vector direction  $\mathbf{Q}_1$  in (b). (a) Theoretical fence points are shown in yellow, gates as green lines. The fence points that one must wind around to achieve nontrivial transport enlarges to the fence area (yellow) in the experiment. Gates are shown as dark and light green circles and show a hysteresis (green area) when winding around the fence area in different directions. We depict a purple loop encircling the yellow area as an example loop inducing nontrivial colloidal transport into the  $\mathbf{n} \times \mathbf{Q}_1$ -direction by exactly one lattice vector  $\mathbf{a}_2$ . This transport direction is protected against perturbations of the driving and the dotted purple loop results in exactly the same net transport because it shares the winding number around the yellow common area with the unperturbed solid modulation loop. (b) Trajectory (blue and red) of the steel sphere subject to the solid purple loop shown in (a). Red segments correspond to faster motion than blue segments. The adiabatic motion smoothly changes from fast to slower. The yellow arrow corresponds to the primitive unit vector pointing into the transport direction. (c) Control space of the  $S_6$ -symmetric lattice. Theoretical fences for paramagnets are shown in red and blue and for diamagnets in black. The experimentally determined fence for the steel sphere lies further outside with two separate regions (blue and red) of instability when leaving the yellow area toward the north or south. We depict a palindrome modulation loop in purple that cycles through the common area back and forth in control space but causes an open trajectory (see (d)) with ratchet jumps of the steel sphere above the lattice. For the part of the loop moving in the mathematical positive sense the winding number around the upper cusp joining the two blue segments is nonzero and causes nontrivial transport, while for the same loop traveling in the mathematical negative sense the winding number around the lower cusp joining the red segments is zero and causes trivial motion. (d) Trajectory (blue and red) of the steel sphere subject to the purple loop shown in (c). The ratchet motion discontinuously changes from slow adiabatic to fast ratchet jumps. (e) Control space of the  $C_6$ -symmetric lattice. Theoretical fences as blue and red lines with the experimental fence shown as crosses of the same color. The purple example loop causes adiabatic transport in the  $(\mathbf{Q}_2 - \mathbf{Q}_3)$ -direction. (f) Trajectory (blue and red) of the steel sphere subject to the purple loop (e). Red segments correspond to faster motion than blue segments. The adiabatic motion smoothly changes from fast to slower. Movies of the motion are provided in the SM.

as that of the common-area-avoiding loops, their character is that of a ratchet. A ratchet jump of the steel sphere from one point on the lattice to a different point occurs when we exit the common area. Loops avoiding the common area cause a smooth quasi adiabatic transport of the steel sphere. Entering or exiting the common area in regions where there are no blue or red fence segments yields statistical results for the steel transport direction.

Two further common areas exist at the location turned by  $\pm 2\pi/3$  along the equator. The theoretical prediction is in topological agreement with the experiments, however, the theoretical common area enclosed between the red and blue line fence segments is smaller than the experimentally measured area and the northern and southern fence segments form a closed line around it with no statistical segments of the common area border. The theoretical

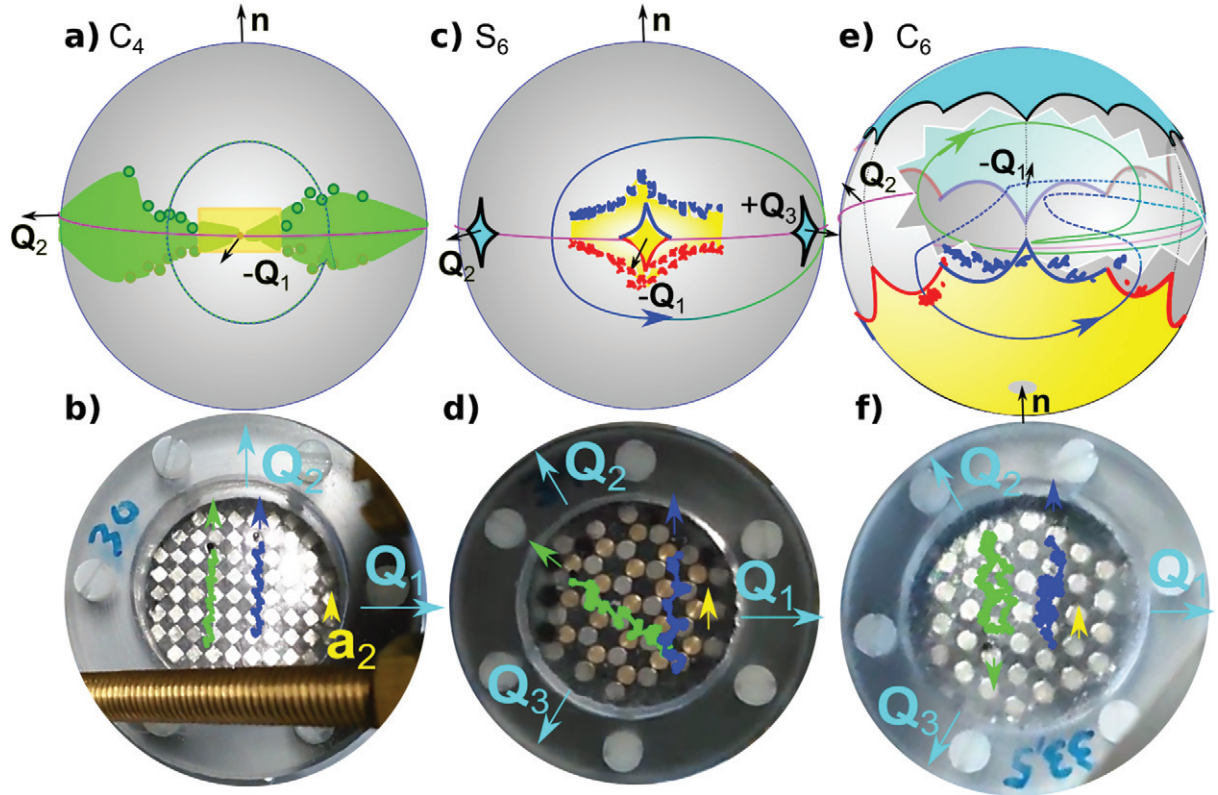


Fig. 3: (Color online) (a) Control space of the  $C_4$ -symmetric lattice. We depict the same loop encircling the yellow area as in fig. 2(a) inducing nontrivial colloidal transport into the  $\mathbf{n} \times \mathbf{Q}_1$ -direction for both paramagnets and superconducting diamagnets. (b) Trajectories (blue) of the steel sphere and (green) of the superconducting sphere subject to the loop shown in (a). Both types of particles are transported in the same direction. Paramagnets and diamagnets reside on oppositely oriented magnets at every instant. (c) Control space of the  $S_6$ -symmetric lattice. We depict a modulation loop (blue-green) that encircles the (yellow) paramagnetic common area around the  $-\mathbf{Q}_1$  direction and the (cyan) diamagnetic common area around the  $\mathbf{Q}_3$  direction. The modulation loop causes an open trajectory (see (d)) with the steel sphere moving in the  $\mathbf{n} \times \mathbf{Q}_1$  direction and the superconducting sphere moving in the  $-\mathbf{n} \times \mathbf{Q}_3$  direction. (e) Control space of the  $C_6$ -symmetric lattice. We have cut a hole into control space (white zig-zag line) to also show the back side of control space. The blue part of our modulation loop on the front of control space causes adiabatic transport of the steel sphere in the  $(\mathbf{Q}_2 - \mathbf{Q}_3)$ -direction (blue trajectory in (f)) and the green part of the modulation loop on the back side of control space causes opposite transport (green trajectory in (f)) of the superconducting sphere. Movies of the motion are provided in the SM.

common areas repeat when we turn the control space by  $2\pi/3$  around the normal vector. The cyan common areas correspond to theoretical areas supposed to cause nontrivial transport of diamagnetic (superconducting) spheres.

In fig. 2(d) we show the trajectory of a palindrome modulation loop for the  $S_6$ -symmetric lattice shown in fig. 2(c). The palindrome loop consists of two sub-loops that are the inverse of each other. The first sub-loop crosses the common area by entering the left southern fence segment (red) and exiting at the northern right segment (blue) and returning to the initial orientation by winding around the cusp joining the two blue fence segments and not winding around the red cusp joining the two red fence segments. Immediately afterwards the second sub-loop retraces the path of the first sub-loop in the opposite direction. The trajectory of the steel sphere is of the ratchet type and does not close because of irreversible

jumps that happen when the modulation loop leaves the common area at different fence segments during the forward and backward period. This nontrivial ratchet motion is in contrast to trivial adiabatic motion where adiabatic palindrome loops always cause the trivial motion back and forth on the same path.

*Proper sixfold symmetric pattern.* In fig. 2(e) we show the control space of the  $C_6$ -symmetric pattern. The transport is adiabatic if a loop enters and exits via segments that have the same blue or red color. If both segment colors differ, the loop causes a ratchet motion. Nontrivial transport into the  $\sigma(\mathbf{Q}_i - \mathbf{Q}_j)$ -direction ( $\sigma = \pm 1$ ,  $i, j = 1, 2, 3$ ) occurs when the modulation loop enters the yellow area via a neighbor segment of the reciprocal unit vector  $\sigma\mathbf{Q}_i$  and exits via a nearest or next nearest neighbor segment of the reciprocal lattice vector  $\sigma\mathbf{Q}_j$ . The sign  $\sigma$  of the nearest or next nearest exit reciprocal vector  $\sigma\mathbf{Q}_j$  must be the same as that of the nearest reciprocal vector

$\sigma\mathbf{Q}_i$  of the entry. The experimental position of the fence (blue and red) has been determined from the irreversible jumps of the steel sphere when the external field exits the yellow area through a segment of opposite color than that of the entry. The match between experiment and theory here is almost perfect. In fig. 2(f) we depict the adiabatic trajectory of the steel sphere above a  $C_6$ -symmetric lattice for a loop passing through the yellow area via the red fence segments in fig. 2(e).

*Transport of paramagnets and diamagnets.* If we open the compartment, fill it with liquid nitrogen and place a steel sphere and a high-temperature superconducting sphere (YBCO) we may study the transport of both paramagnetic and diamagnetic spheres. For the fourfold pattern we observe parallel transport of the steel and superconductor spheres with spheres of different character separated by an odd multiple of  $(\mathbf{a}_1 + \mathbf{a}_2)/2$ . On the  $C_6$  and  $S_6$  patterns the steel and superconductor sphere can be transported independently, because the yellow and cyan common areas are lying in different opposing locations of the control space. In fig. 3(b), (d), (f) we show the simultaneous transport of a steel and a superconductor sphere subject to example loops depicted in fig. 3(a), (c), (e).

**Discussion and conclusion.** – From the measurements we see that the experiments are in topological agreement with the theory [6–8]. The most striking difference between experiment and theory is the existence of a hysteresis visible in the  $C_4$ - and  $S_6$ -symmetric patterns. We explain the shift of the experimental fence with respect to the theoretical predictions as well as the hysteresis by solid friction that lets the steel particle move only when the magnetic potential exceeds a certain slope. Slopes for a forward and backward jump will have opposite sign explaining the splitting of the closed theoretical fence in the  $S_6$ -pattern into two separate blue and red fences. The asymmetry of the hysteresis in fig. 2(a) is an indicator for the influence of noise in the magnetization of the pattern and the noise of the solid friction. Note that without solid friction there should not be any hysteresis. Hydrodynamic friction vanishes in the adiabatic limit and can, without solid friction, be made arbitrary small by reducing the speed of modulation.

Let us note that the topological protected transport theory has been developed for colloidal particles not for steel spheres. The scale invariance of the theory (the scales differ by a factor  $10^3$ ) demonstrates the robustness of the topological concept. Presumably it is also possible to down scale the experiment from the colloidal toward molecular scales, which would provide a transport mechanism for molecular magnets above magnetic nano

structures that could be sorted according to their magnetic properties. There instead of solid friction thresholds with hysteresis thermal fluctuations (the influence of which was studied in detail in ref. [7]) will be relevant, the topological properties will however probably remain robust enough to dominate the dynamics.

\* \* \*

JB acknowledges financial support by a Ghana MOE - DAAD joined fellowship. We appreciate scientific support by JOHANNES LOEHR and by DANIEL DE LAS HERAS.

## REFERENCES

- [1] HASAN M. Z. and KANE C. L., *Rev. Mod. Phys.*, **82** (2010) 3045.
- [2] SHEN S.-Q., *Topological Insulators: Dirac Equation in Condensed Matters* (Springer Science and Business Media) 2013.
- [3] RECHTSMAN M. C., ZEUNER J. M., PLOTNIK Y., LUMER Y., PODOLSKY D., DREISOW F., NOLTE S., SEGEV M. and SZAMEIT A., *Nature*, **496** (2013) 196.
- [4] XIAO M., MA G., YANG Z., SHENG P., ZHANG Z. Q. and CHAN C. T., *Nat. Phys.*, **11** (2015) 240.
- [5] MURUGAN A. and VAIKUNTANATHAN S., *Nat. Commun.*, **8** (2017) 13881.
- [6] LOEHR J., LOENNE M., ERNST A., DE LAS HERAS D. and FISCHER TH. M., *Nat. Commun.*, **7** (2016) 11745.
- [7] DE LAS HERAS D., LOEHR J., LOENNE M. and FISCHER TH. M., *New J. Phys.*, **18** (2016) 105009.
- [8] LOEHR J., DE LAS HERAS D., LOENNE M., BUGASE J., JAROSZ A., URBANIAK M., STOBIECKI F., TOMITA A., HUHNSTOCK R., KOCH I., EHRESMANN A., HOLZINGER D. and FISCHER TH. M., *Soft Matter*, **13** (2017) 5044.
- [9] KANE C. L. and LUBENSKY T. C., *Nat. Phys.*, **10** (2014) 39.
- [10] PAULOSE J., CHEN B. G. and VITELLI V., *Nat. Phys.*, **11** (2015) 153.
- [11] NASH L. M., KLECKNER D., READ A., VITELLI V., ARI M. TURNER and IRVINE W. T. M., *Proc. Natl. Acad. Sci. U.S.A.*, **112** (2015) 14495.
- [12] HUBER S. D., *Nat. Phys.*, **12** (2016) 621.
- [13] RICE M. J. and MELE E. J., *Phys. Rev. Lett.*, **49** (1982) 1455.
- [14] HALPERIN B. I., *Phys. Rev. B*, **25** (1982) 2185.
- [15] RUDNER M. S., LINDNER N. H., BERG E. and LEVIN M., *Phys. Rev. X*, **3** (2013) 031005.
- [16] KUŚWIK P., EHRESMANN A., TEKIELAK M., SZYMAŃSKI B., SVEKLO I., MAZALSKI P., ENGEL D., KISIELEWSKI J., LENGEMANN D., URBANIAK M., SCHMIDT C., MAZIEWSKI A. and STOBIECKI F., *Nanotechnology*, **22** (2011) 095302.



# Eidesstattliche Versicherung

Hiermit versichere ich an Eides statt, dass ich die vorliegende Arbeit selbstständig verfasst und keine anderen als die von mir angegebenen Quellen und Hilfsmittel verwendet habe.

Zusätzlich erkläre ich hiermit, dass ich keinerlei frühere Promotionsversuche unternommen habe.

Weiterhin erkläre ich, dass ich die Hilfe von gewerblichen Promotionsberatern bzw. -vermittlern oder ähnlichen Dienstleistern weder bisher in Anspruch genommen habe, noch künftig in Anspruch nehmen werde.

Jonas Bugase  
Bayreuth, June 12, 2018